METAMATERIAL-INSPIRED ELECTROELASTOACOUSTIC ENERGY HARVESTING

A Dissertation
Presented to
The Academic Faculty

By

Amirebrahim Darabi

In Partial Fulfillment of the Requirements for the Degree
Doctor of Philosophy in the
George W. Woodruff School of Mechanical Engineering

Georgia Institute of Technology
December 2017

METAMATERIAL-INSPIRED ELECTROELASTOACOUSTIC ENERGY HARVESTING

Approved by:

Dr. Michael J. Leamy, Advisor
School of Mechanical Engineering
Georgia Institute of Technology

Dr. Massimo Ruzzene
School of Aerospace Engineering
Georgia Institute of Technology

Dr. Karim Sabra
School of Mechanical Engineering
Georgia Institute of Technology

Dr. Julian Rimoli
School of Aerospace Engineering
Georgia Institute of Technology

Dr. Aldo Ferri
School of Mechanical Engineering
Georgia Institute of Technology

Dr. Laurence Jacobs
School of Civil Engineering
Georgia Institute of Technology

Date Approved: October 31, 2017

To my parents

Mohammadreza Darabi and Shahin Arabi

ACKNOWLEDGEMENTS

First, I want to thank God for never leaving me alone in my hard moments, helping me in my time of need, and guiding me to take the best decisions. I am deeply indebted to my adviser, Dr. Michael Leamy, for guiding me through four years of my PhD. He was always understanding and supportive through ups and downs of research. His passion toward science and research encouraged me to work harder and be eager to learn more and more every day.

My special gratitude goes to my thesis committee members, Dr. Massimo Ruzzene, Dr. Aldo Ferri, Dr. Laurence Jacobs, Dr. Karim Sabra, and Dr. Julian Rimoli for their invaluable assistance and guidance. Their patronage helped me with my research through my PhD journey, and their commitment assisted me with accomplishing my PhD studies.

I would like to express my deep indebtedness to my parents Mohammadreza Darabi and Shahin Arabi. I can never express in words how thankful I am to have them, but I will try my best to always make them proud of me. They always have been very understanding, helpful and supportive of my decisions. I would like to extend my gratitude to my amazing brother, Amirhossein Darabi.

I would like to thank my labmates for their training and support and all the good time I had with them in the past four years. I would like to extend my appreciation to Justin Willbanks, Matthew Fronk, and Saeid Loghavi.

I also would like to thank my friends in the Georgia Tech soccer club, specially Sommy Khalaj for all the great memories they made for me during the time I played

for the team.

I am greatly indebted to my friend, Dr. Shaghayegh Fathi, for her support over the past three years.

My special thank to Hossein and Mohammad Taghinejad for all of their helps and supports in the past few months for my faculty position applications.

I would also like to send my gratitude to ones who always believed in me and never lost faith in me. All friends and family who were there for me when I was feeling down. They helped and encouraged me to stand tall and motivated to defeat all the challenges and problems in the world.

TABLE OF CONTENTS

List of Tables

List of Figures

SUMMARY

Following an introduction to the research and literature review in the first chapter, the second chapter concerns a clearance-type nonlinear energy sink to harvest electrical power from non-stationary mechanical waves. Closed-form solutions are found which quantify the relationship between the impact amplitude and the energy produced. Analytical, computational, and experimental methods are employed to explore and verify the sink performance.

An analytical framework for predicting the wave energy harvested by a circular piezoelectric disk attached to a thin plate is presented next in the third chapter. A harmonic point source excitation generates waves incident on a piezoelectric disk. In addition, the voltage generated by the harvester is calculated using coupled electromechanical equations. The system is studied in the frequency domain and the optimum harvester resistance is found for generating the most electrical energy. The analysis is validated by comparing predicted response quantities to those computed using numerical simulations and measured through an experimental setup.

The fourth chapter develops and experimentally validates a multiple scattering approach for computing the wave response of plate-harvester systems incorporating multiple scatterers. The overall goal is to enhance the wave power generated by a circular piezoelectric disk via the addition of targeted cylindrical inclusions. Specifically, the multiple scattering formulation is applied to the determination of optimal arrangements of scatterers in a semi-elliptical path which maximizes focused wave energy and electrical power. Representative experiments are carried out to demonstrate

the validity of the analytical approach.

The fifth and final technical chapter develops a fully-coupled T-matrix formulation for analyzing scattering of incident wave energy from a piezoelectric patch attached to a thin plate. More generally, the T-matrix represents an input-output relationship between incident and reflected waves from inclusions in a host layer, and is introduced herein for a piezoelectric patch connected to an external circuit. This generalizes the system from Chapter 4 such that multiple piezoelectric harvesters can appear together in the formulation, and has broader implications for wave-based electromechanical systems used to generate and sense waves (e.g., as used in structural health monitoring techniques). The chapter closes with analytical and experimental studies of a funnel-shaped waveguide formed by placing rigid aluminum inclusions in, and multiple piezoelectric harvesters on, a Lexan plate.

Chapter 1

Introduction

1.1 Overview

Energy harvesting has emerged as a viable means for powering low-power electronic devices. It enables energy collection directly from the environment to power electronics, or to recharge a secondary battery. Environmental energy harvested may include kinetic energy in the form of vibration and noise, electromagnetic radiation, thermal energy, and others [1, 2]. Harvesting of *vibrational* energy for low-power electronic components, such as wireless sensor networks, has been studied extensively over the past few years. A variety of transduction methods have been considered, to include piezoelectric [3], electrostatic [4], electromagnetic [5] and magnetostrictive [6] transduction. Harvesting of *wave* energy has received little attention and is the subject of this thesis.

An effective approach for wave energy harvesting may entail *trapping* a portion of incident energy in a subdomain, and then harvesting the subdomain's energy over a finite period of time. Trapping of wave energy is particularly useful in situations where the energy source is present during short intervals of time, such as non-stationary excitation, impact events, wind gusts, etc. Nonlinear energy sinks (NES's) offer one approach for trapping energy in a subdomain. NES's employ a highly nonlinear element such that when they are attached to a linear subdomain, energy is trapped

in the nonlinear element for extended periods of time [7].

A second effective approach for harvesting waves may entail first *focusing* using arrangements inspired by metamaterials – so-called metamaterial-inspired energy harvesting (MEH). To focus the energy of the propagating wave, the MEH's use periodic arrays of scatterers and the Bragg scattering effect [8] to form phononic crystals exhibiting frequency bandgaps. Bragg scattering bandgaps occur at wavelengths on the order of the unit cell size and can be employed in phononic crystals to filter, localize, and guide acoustic waves [9, 10].

1.2 Energy Trapping

1.2.1 Nonlinear energy sinks

Reciprocity-breaking materials offer one means for trapping energy in a subdomain. Such materials are enablers for acoustic diodes, one-way mirrors, and rectifiers. Sun, Zhang and Shui [11] used a simple linear acoustic system to design an acoustic diode composed of a thin brass plate with single-sided, periodic gratings immersed in water. Maznev *et al.* [12] reviewed examples of nonlinear designs which break reciprocity while discussing precise criteria for deeming a system reciprocity breaking. They also showed a thermal (e.g., energy due to lattice vibrations) diode is not possible for ballistic phonon transport in a linear system. A new technique of phonon-based thermal rectification on a thin Si membrane has been presented by Schmotz *et al.* [13]. The symmetry of the heat flow was broken and phonon motion was limited to one direction, thus yielding a diode. One of the earliest works to explore experimentally

the significant rectifying phenomenon in acoustic waves is the study by Liang *et al.* [14]. The acoustic diode which they fabricated allows part of the acoustic energy flux incident from one particular side to pass, but acts as an insulator when the wave propagates in the opposite direction. Liang *et al.* [15] also studied longitudinal waves in a nonlinear system and suggested acoustic diode mechanisms. Sonic crystals (or phononic crystals), in analogy with photonic crystals, have also impacted acoustic reciprocity. Feng *et al.* [16] showed experimentally unidirectional transmission in a device incorporating a linear sonic crystal. Their diode uses an asymmetrical, periodically corrugated crystal consisting of a diffraction structure and a regular sonic crystal. Still others have shown that, by utilizing mode conversion and selection, one-way behavior can be achieved in a generic manner in one-dimensional phononic crystal plates with both symmetric and antisymmetric structures [17, 18].

Nonlinear energy sinks offer an approach for trapping energy in a subdomain. NES's employ a highly nonlinear element such that when they are attached to a linear subdomain, energy is trapped in the nonlinear element for extended periods of time. Vakakis and co-authors [19, 20, 21, 22] have carried-out numerous studies on NES's in which an essentially nonlinear attachment to a linear structure has been used to absorb significant energy from the linear part. Their work develops the theoretical underpinnings and experimental realization of passive NES's for mitigating vibration due to impulsive excitation. Nonlinear modal interactions between aeroelastic and NES modes in a single degree of freedom nonlinear energy sink has been investigated carefully by Lee [23] *et al.* using both analytical and experimental methods. They worked on enhancing the robustness of instability suppression for the SDOF NES.

Gendelman *et al.* [24, 25] studied a small NES subjected to external harmonic force with a large mass close to the resonance frequency. They focused on quasiperiodic behavior in a vibration-absorbing NES, and performed experimental validation using a nonlinear electric circuit. They also considered nonlinear damping with piecewise-quadratic characteristics as a new NES enabler. This strategy helps to eliminate an undesirable periodic regime present when an NES is coupled with a linear oscillator under harmonic force excitation. A general, nonlinear, aeroelastic system exhibiting flutter oscillations was considered by Loungo *et al.* [26]. An attached NES was shown to limit vibration amplitudes experienced by the system. Zulli and co-authors studied a primary structure consisting of a Duffing-type nonlinear oscillator attached to a single-degree of freedom NES [27]. This design helps to suppress vibration induced by a bi-frequency harmonic excitation.

1.2.2 Hybrid dynamical systems

The clearance-type nonlinear energy sink concept explored in Chapter 2 can be classified broadly as a hybrid dynamical system due to its exploitation of discontinuous dynamics. A hybrid dynamical system is any dynamical system containing both continuous and discrete dynamic behavior. Typically, such a system can both flow (described by differential equations) and jump (described by difference equations). These two kinds of dynamics interact and generate complex dynamical behavior, such as switching, state jumping, and bifurcations [28]. Impact oscillators are one prototypical hybrid system found commonly and at many length scales; e.g., in heavy machinery and in small-scale devices. Bifurcation behavior in hybrid dynamical sys-

tems has been studied carefully in Kowalczyk and Bernardo [29] and Luo [30]. Decarlo *et al.* focused on the stability of hybrid systems within the narrow confines of switching among a finite set of possible motions [31]. An overview of bifurcation phenomena for non-smooth dynamical systems was presented by Leine *et al.* [32]. They studied example systems which demonstrate that bifurcations in non-smooth systems are sometimes similar to known bifurcations from classical bifurcation theory in smooth vector fields. The dynamics of repeated impacts with a sinusoidal vibrating table, with dissipation, has been presented as an important hybrid system [33]. In addition to these studies, Luo *et al.* [34] considered multi-performance and multi-parameter simulation analysis for dynamics of periodically forced impact system with a clearance represented by two symmetric rigid stops. The excitation frequency and clearance distance were used as bifurcation parameters to analyze the performance of the system and their influence on impact velocities and existence regions.

1.3 Energy Focusing

1.3.1 Vibrational energy harvesting

During the past few decades, significant research has been carried-out on the harvesting of vibrational energy in order to power small electronic components, such as wireless sensor networks and resonators. Previous studies have used piezoelectric [35], electrostatic [4], electromagnetic [5] and magnetostrictive [6] transduction to harvest direct vibrational energy. In contrast, there are relatively few studies on harvesting propagating waves in structures. Those present have considered Helmholtz

resonators [36], sonic crystals [37] and polarization-patterned piezoelectric solids [38] for structure-borne or air-borne wave energy harvesting. Carrara *et al.* introduced multiple metamaterial energy harvester approaches for enhancing wave energy harvesting of structure-borne waves using arrays of acoustic scatterers attached to a thin plate [39, 40] (Figure. 1). MEH concepts studied include arrays which focus energy using an elliptical or parabolic shape (i.e., an acoustic mirror), localize waves using 2D lattice structure with an imperfection, or amplify waves via acoustic funneling [40]. Finally, they proposed a Fourier transform-based harvester design to further enhance the energy extraction from incident waves [41]. Among the MEH concepts introduced to date, the elliptical MEH mirror appears to hold the most promise as a source at one focal point of an ellipse can be perfectly focused at the other focal point. However, in practice, only a small portion of the ellipse is used, which while focusing much of the incident energy, results in spurious effects such as side lobes and other unfocused artifacts. In developing their MEH concepts, Carrara *et al.* used simple, but effective, scattering models to predict energy focusing useful for informing preliminary designs. For example, the scatterers were assumed to act as point sources which scatter incident waves with 100% efficiency. Furthermore, the harvesting element (e.g., piezoelectric disk) was not part of the model, and so detailed predictions of harvesting performance were not made. Shuibao Qi *et al.* proposed AEH (acoustic energy harvester) system consists of acoustic energy confinement part (acoustic model) and strain energy conversion part (electrical model). They used an array of silicone rubber stubs on a thin plate. This innovative concept scavenges the airborne acoustic wave energy by using a planar AMM (acoustic metamaterials) with

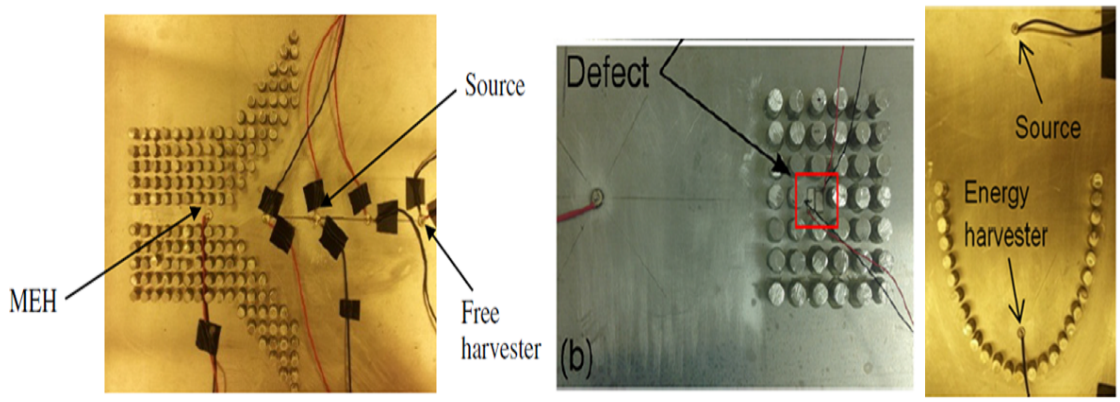

Figure 1.1: ***Schematic of multiple-scattering problem***

piezoelectric material [42].

1.3.2 Multiple scattering method

Numerous studies have been carried out on the subject of wave scattering from the perspective of energy flux conservation via a transfer matrix (i.e., T-matrix) [43, 44]. For a single scattering problem, the T-matrix relates the scattered and incident waves' characteristic coefficients in linear transformation form. Once the T-matrix is formulated, several instances of it can then be used in a multiple-scattering context to compute a problem's total wavefield. The T-matrix paradigm was introduced by Waterman for analyzing scattering of electromagnetic waves by objects of general shapes [45]. Later, Waterman employed the concept to study scattering of acoustic waves [46]. The null-field method introduced in Waterman's papers typically requires numerical evaluation of an integral equation to obtain the T-matrix elements. On the other hand, for problems with simple geometries, such as cylindrical or spherical shapes, the T-matrix can be obtained in closed-form using a separation of variables approach and matching of scatterer boundary conditions [47, 48, 49]. In this vein,

Cai and Hambric recently presented such analytical expressions for thin plates using Kirchhoff theory to detail T-matrices for a variety of inclusion-type scatterers (rigid, elastic, and void) [50]. Cai subsequently studied several multiple-scattering problems, to include wave propagation through a phononic crystal.

Chapter 2

Electroacoustic Clearance-Type Nonlinear Energy Sink

2.1 Overview

This chapter explores a clearance-type nonlinear energy sink for increasing electrical energy harvested from non-stationary mechanical waves, such as those encountered during impact and intermittent events. The key idea is to trap energy in the NES such that it can be harvested over a time period longer than that afforded by the passing disturbance itself. Analytical, computational, and experimental techniques are employed to optimize the energy sink, explore qualitative behavior (to include bifurcations), and verify enhanced performance. Unlike traditionally-studied single-DOF NESs, both subdomains of the NES (i.e., on either side of the clearance) contain displaceable degrees of freedom, increasing the complexity of the analytical solution approach. However, closed-form solutions are found which quantify the relationship between the impact amplitude and the energy produced, parameterized by system properties such as the harvester effective resistance, the clearance gap, and the domain mass and stiffness. Bifurcation diagrams and trends therein provide insight into the number and state of impact events at the NES as excitation amplitude increases. Moreover, a closed-form Poincaré map is derived which maps one NES impact location to the next, greatly simplifying the analysis while providing an important tool

for follow-on bifurcation studies. Finally, a series of representative experiments are carried-out to realize the benefits of using clearance-type nonlinearities to trap wave energy and increase the net harvested energy.

The chapter is organized as follows: first a discrete model is proposed which captures the essential, hybrid dynamics of the clearance-type nonlinear wave energy harvester. Analytical and numerical solutions are then pursued to solve the equations of motion, optimize system parameters, and highlight important phenomena. The analysis includes insight from Poincaré sections, bifurcation diagrams, and example state trajectories, with and without harvesters. Guided by these studies, a series of experiments are presented which show the potential benefits of using clearance-type nonlinearities in harvesting energy from non-stationary loads.

2.2 System Model

A simplified model of a clearance-type nonlinear energy sink is developed and analyzed in this section. This model captures the essential aspects of the idea and enables straight-forward analytical, numerical, and experimental assessment of its ability to enhance energy harvesting. Motivation for this system comes primarily from previous work in which metamaterial-inspired funnels and mirrors have been used to direct and concentrate broadband elastic wave energy onto piezoelectric harvesters. While this idea has been shown to greatly enhance energy harvesting in steady-state conditions, it proves to be less effective in non-stationary situations where the incident wave energy is present for short durations of time, such as in impact systems, random

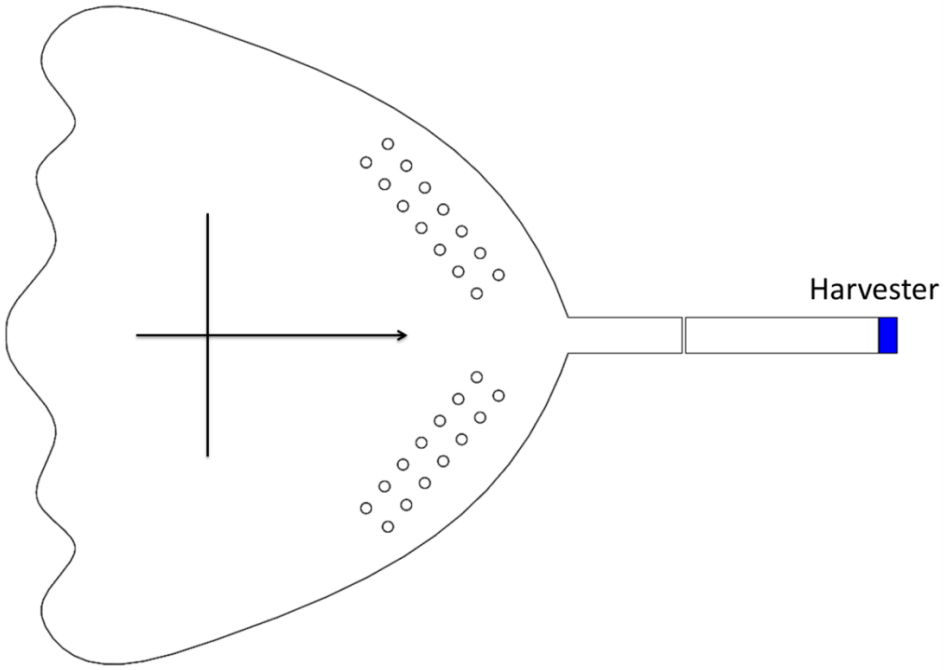

Figure 2.1: ***Schematic representation of an energy harvesting configuration showing a metamaterial-inspired funnel and a clearance-type nonlinear energy sink.***

vibrations, wind gusts, etc. In these situations, it may be beneficial to extend the developed concept to include a nonlinear energy sink, as shown in Figure. 2.1. There, a funnel-shaped periodic arrangement of stubs on a plate, for example, directs and concentrates wave energy to a clearance-type nonlinear sink. The energy sink traps a portion of the energy in an additional subdomain, where it is then harvested over a period of time much greater than the non-stationary event that produced the incident energy. By proper design, and due to the fact that traditional energy harvesting techniques capture only a small percent of the incident power, it can be expected that the trapped energy is a significantly higher percentage of energy than that which can be harvested without the energy sink.

A model capturing the essential ideas from above is shown in Figure. 2.2. It

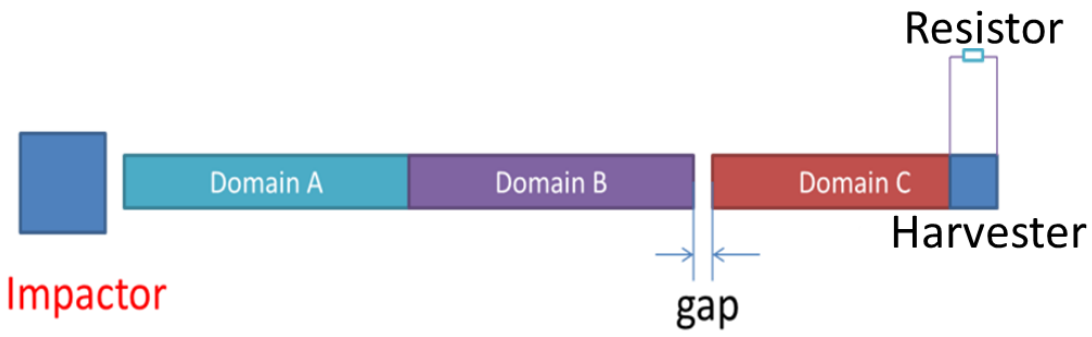

Figure 2.2: ***Schematic of the NES with an attached harvester and electrical circuit.***

consists of three one-dimensional subdomains, a clearance between the second and third subdomains, an impactor providing excitation, and a harvester that converts mechanical to electrical energy. An elastic wave excited by the impactor propagates from the first subdomain (A) and passes through the second subdomain (B). Subdomain B is chosen to have smaller impedance (e.g., stiffness) than the C subdomain, and thus bridges the gap at lower amplitudes than a wave-approaching subdomain B from subdomain C. The differing subdomains (B and C) separated by a clearance yields asymmetry and nonlinearity, which are hallmarks of non-reciprocity. Contact between the B and C subdomains transfers a portion of the wave energy to subdomain C, where it is then trapped due to the larger impedance of subdomain C.

As a first step in analyzing the system, a lumped parameter model composed of masses, springs, and a harvester element is proposed as shown in Figure. 2.3. The harvesting frequency range of interest determines the length scale assumed for each lumped element. Without loss of generality, each subdomain is assumed to have the same mass $m_A = m_B = m_C = m$, but differing stiffnesses k_A, k_B, k_C. The gap is

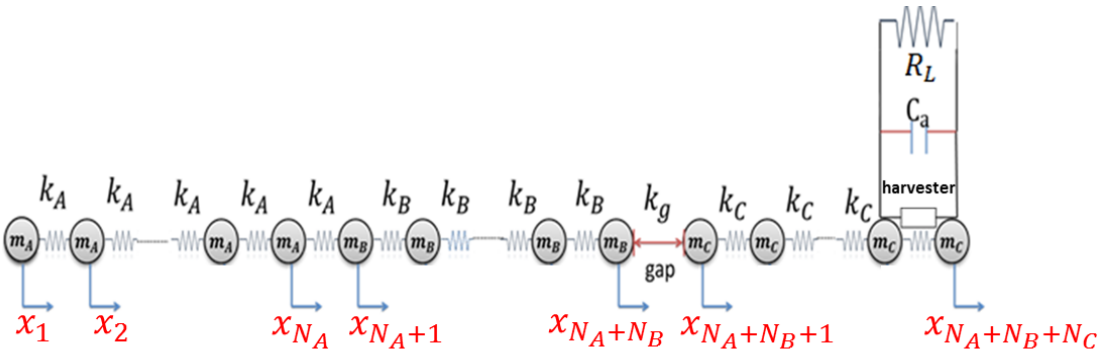

Figure 2.3: ***Schematic of the NES with harvester and electrical circuit (discrete model).***

modeled with either a stiffness, k_g, or a coefficient of restitution, e, as discussed in more detail later. The capacitance of the harvester is denoted by C_a and the resistance of the piezoelectric is denoted by R_l.

It is assumed an impact, or other non-stationary event, causes a wave to start propagating from the first mass and to pass through to the B subdomain. Further propagation and subsequent impact past the clearance gap transfers energy from the B subdomain to the C subdomain. If one considers subdomains B and C to be a device designed to harvest energy from subdomain A, one needs to optimize the stiffness and masses of these subdomains, along with the stiffness of the clearance gap and its initial separation, to trap the most energy in the third subdomain. In addition to these parameters, for electrical optimization, one needs to consider the resistance of the electrical circuit and the coupling term of the harvester.

2.2.1 Governing equations of mechanical motion

Motion of a single mass

The motion of each mass shown in Figure 3 is governed by

$$m\ddot{x}_i + k_j(x_i - x_{i-1}) + k_{j'}(x_i - x_{i+1}) = 0 \tag{2.1}$$

where $j, j' = A, B, C$ distinguish left and right springs, respectively, in subdomains A, B, and C. Note that Eq. (2.1) holds for all masses apart from the two involved in contact across the clearance gap. Two different approaches are considered for gap modeling, each invoking an idealization not satisfied exactly in practice. In the first, a stiff gap spring (GS) models the interaction of the two subdomains as they initiate contact, while in the second approach, a coefficient of restitution (CoR) is introduced. In the former, contact and loss of contact occurs over a finite time, while in the latter these events occur in zero time. Thus, the dynamics (and optimized parameters) can differ depending on the use of each. A further, equally important, distinction concerns the analysis approaches afforded by each: the CoR approach allows one to use return maps and new techniques from the study of hybrid dynamical systems, while the GS approach requires ones to resort to numerical solution methods.

Gap modeling

For GS modeling, the following equations govern contacting masses:

$$\text{if} : g = g_0 + x_{N_B+N_{A+1}} - x_{N_B+N_A} < 0 \tag{2.2a}$$

$$m_B\ddot{x}_{N_B+N_A} = m_B\ddot{x}_{N_B+N_A} + k_g * g \tag{2.2b}$$

$$m_C\ddot{x}_{N_B+N_A+1} = m_C\ddot{x}_{N_B+N_A+1} - k_g * g \tag{2.2c}$$

where g and g_0 are the gap and initial gap distances, respectively, and k_g denotes the stiffness of the gap spring. When condition Eq. (2.2a) is satisfied, the gap spring is compressed and energy transfers from the the last mass of second subdomain ($x_{N_B+N_A}$) to the first mass of third subdomain ($x_{N_B+N_A+1}$), based on Eqs. (2.2b-2.2c)

For CoR modeling, the contacting masses are governed by

$$\text{if} : g = g_0 + x_{N_B+N_A+1} - x_{N_B+N_A} < 0 \tag{2.3a}$$

$$v + w = v' + w' \tag{2.3b}$$

$$e = \frac{v' - w'}{w - v} \tag{2.3c}$$

where v is the pre-impact velocity of the end mass from subdomain B and w is the pre-impact velocity of the front mass in subdomain C. Similarly, post-impact velocities are denoted by (’). The two impacting masses will be denoted by index $M = N_A + N_B$ and $M + 1$. Similar to the GS model, when Eq. (2.3a) is satisfied, the energy of the wave is transferred to the third domain using the conservation of momentum (Eq. (2.3b)) and energy (Eq. (2.3c)) relationships.

Energy propagation

Similar to contact, two different means for exciting waves are considered for completeness. For each, the last mass in subdomain C is treated as either free or fixed. Waves are excited by choice of an initial condition for the first mass of subdomain A, simulating an impact event. In the first excitation case, the first mass has a nonzero displacement (ID) and zero velocity. In the second case, the first mass has a zero displacement and nonzero velocity (IV). For ID, an initial force F_0 displaces the first mass while the second mass is held in place, yielding an initial displacement,

$$\delta = x_0 = F_0/k_A \tag{2.4}$$

For IV, the first mass receives initial momentum M_0, resulting in initial velocity,

$$\nu = v_0 = M_0/m_A \tag{2.5}$$

Each subdomains mechanical energy is given by the usual expressions for kinetic and potential energy. The total mechanical energy, E_{total}, is then the sum of all energies in the system, including that stored by the gap spring. E_{total} is constant before placing a harvester in the C subdomain and is equal to the energy imparted by the input excitation to the first mass. This energy is equal to the stored potential energy of the first spring for the ID case, and the imparted kinetic energy of the first mass for the IV case. Thus,

$$E_{total} = \frac{1}{2} k_A \delta^2 \tag{2.6}$$

$$E_{total} = \frac{1}{2} m_A \nu^2 \tag{2.7}$$

for ID or IV, respectively. To measure the trapped mechanical energy in subdomain C, the non-dimensional parameter ε is defined as

$$\varepsilon = E_3 / E_{total} \tag{2.8}$$

where E_3 is the total energy present in the third subdomain (i.e., the trapping subdomain).

2.2.2 Harvester governing equations

To generate electrical power, subdomain C must include an electrical harvester. This work considers an idealized harvester between the N_{th} and $(N-1)_{th}$ masses in sub-

domain C, which can employ piezoelectric, electromagnetic, or any other means of electromechanical transduction. Note that $N = N_A + N_B + N_C$. The coupled equations governing such a harvester are given by

$$C_p\dot{v} + \frac{v}{R_l} + \theta(\dot{x}_{N-1} - \dot{x}_N) = 0 \tag{2.9}$$

$$m\ddot{x}_{N-1} + k_C(x_{N-1} - x_{N-2}) + k_C(x_{N-1} - x_N) - \theta v = 0 \tag{2.10}$$

where v denotes the voltage, R_l the electrical resistance, C_p the capacitance, and θ is the electromechanical coupling coefficient relating the output voltage to the harvester displacements. Note that when the last mast of the system is free,

$$m_C\ddot{x}_N + K_C(x_N - x_{N-1}) - \theta v = 0 \tag{2.11}$$

In order to assess the efficiency of electrical power generation, a non-dimensional harvested energy μ is defined as

$$\mu = \frac{E_R}{E_{total}} \tag{2.12}$$

where E_R is the energy harvested by the resistance element in the electrical circuit.

For later reporting purposes, the following nondimensional parameters are intro-

duced,

$$k_A/m = \omega_1, \;\; \tau = \omega_1 t, \;\; \frac{d^2}{dt^2} = \omega_1^2 \frac{d^2}{d\tau^2}, \;\; k_B/k_A = \kappa_B, \;\; k_C/k_A = \kappa_C, \;\; k_g/k_A = \kappa \quad (2.13)$$

$$\overrightarrow{\boldsymbol{x}} = (x_1, x_2, , x_{N_A+N_B+N_C})$$

Further, for the ID case dimensionless distances can be defined as

$$\chi_i = x_i/\delta, \;\; \eta = g/\delta \quad (2.14)$$

and for the IV case

$$\chi_i = \frac{x_i}{\nu\omega_1}, \;\; \eta = \frac{g}{\nu/\omega_1} \quad (2.15)$$

2.3 Analytical Solution Approach

For the CoR treatment of the clearance gap, tools from hybrid dynamical systems are employed to find analytical solutions to the system equations. Presently, such an approach cannot be applied to the system of equations modeled with a gap spring due to the finite time associated with the impact event.

The hybrid dynamical system approach requires the equations of motion to be

assembled in canonical form as follows:

$$\dot{\overrightarrow{\mathbf{p}}} = \mathbf{F}(\overrightarrow{\mathbf{p}}) \qquad \text{if} : H(\overrightarrow{\mathbf{p}}) > 0 \tag{2.16}$$

$$\dot{\overrightarrow{\mathbf{p}}} \rightarrow \mathbf{R}(\overrightarrow{\mathbf{p}}) \qquad \text{if} : H(\overrightarrow{\mathbf{p}}) = 0 \tag{2.17}$$

where $\overrightarrow{\mathbf{p}}$ denotes the system states (i.e., displacements and velocities), Σ is the impact surface given by the zero set of the smooth function $H(\overrightarrow{\mathbf{p}}) = 0$ (i.e., where impact occurs), $\mathbf{F}(\overrightarrow{\mathbf{p}})$ is a smooth vector field defined in a neighborhood of Σ, and $\mathbf{R}(\overrightarrow{\mathbf{p}})$ is the reset map defined by the impact rule. The system state is defined as

$$\overrightarrow{\mathbf{p}} = \left(x_1, \dot{x}_1, x_2, \dot{x}_2, ...x_{(N_A+N_B)}, \dot{x}_{(N_A+N_B)}, ...x_{(N_A+N_B+N_C)}, \dot{x}_{(N_A+N_B+N_C)}, v, \dot{v}\right) \tag{2.18}$$

A first order system is defined by introducing derivatives of the displacements and the harvester voltage as follows

$$\dot{x}_j = y_j, \dot{v} = q \tag{2.19}$$

The definition for $\overrightarrow{\mathbf{p}}$ is valid for both systems with initial displacement or velocity (with or without harvester); however, $\mathbf{F}(\overrightarrow{\mathbf{p}})$ requires different forms for each case. $\mathbf{F}(\overrightarrow{\mathbf{p}})$ is written as

$$\mathbf{F}(\overrightarrow{\mathbf{p}}) = (f_{1,j}, f_{2,j}, ..., ...f_{2N,j}, f_{2N+1,j}, f_{2N+2,j}, f_{2N+3,j}) \tag{2.20}$$

where $j = 1$ denotes the ID case and $j = 2$ denotes the IV case. Subsequently, the vector field for the two cases is given by

$$f_{i,1}(p) = \begin{cases} y_i & i = 2k-1 \\ k_C(x_{N-2} + x_N - 2x_{N-1}) + \theta V & i = 2N-2 \\ 0 & i = 2N-1 \\ 0 & i = 2N \\ q & i = 2N+1 \\ -V/R_l C_p - \theta(\dot{x}_{N-1} - \dot{x}_N)/R_l & i = 2N+2 \\ 1 & i = 2N+3 \\ k_j(x_{i-1} - x_i) + k_{j'}(x_{i+1} - x_i) & \text{else} \end{cases}. \tag{2.21}$$

$$f_{i,2}(p) = \begin{cases} y_i & i = 2k-1 \\ k_C(x_{N-2} + x_N - 2x_{N-1}) + \theta V & i = 2N-2 \\ y_N & i = 2N-1 \\ k_C(x_{N-1} - x_N) + \theta V & i = 2N \\ q & i = 2N+1 \\ -V/C_p - \theta(\dot{x}_{N-1} - \dot{x}_N) & i = 2N+2 \\ 1 & i = 2N+3 \\ k_j(x_{i-1} - x_i) + k_{j'}(x_{i+1} - x_i) & \text{else} \end{cases}. \tag{2.22}$$

Note that when the harvester is not present in the system, $V = \theta = q = 0$ in Eqs. (2.212.22).

The impact surface and reset map still require functional forms. The impact surface derives from closing of the clearance gap,

$$\Sigma = \left\{ \overrightarrow{\mathbf{p}} : x_{M+1} + g_0 - x_M = 0 \right\} \tag{2.23}$$

which determines $H(\overrightarrow{\mathbf{p}})$ as

$$H(\overrightarrow{\mathbf{p}}) = x_{M+1} + g_0 - x_M \tag{2.24}$$

The reset map $\mathbf{R}(\overrightarrow{\mathbf{p}})$ (or impact function) links the state of the system before the j_{th} impact, $\overrightarrow{\mathbf{p}}(t_j^-)$, to the state after impact, $\overrightarrow{\mathbf{p}}(t_j^+)$. Recalling that $M = N_A + N_B$ and that impact only changes the velocity of the impact masses,

$$[\mathbf{R}(\overrightarrow{\mathbf{p}})]_{2N+2\times 2N+2} \rightarrow R_{ij} = \begin{cases} \frac{1+e}{2} & (i,j) = (2M, 2M), (2(M+1), 2(M+1)), \\ \frac{1-e}{2} & (i,j) = (2M, 2(M+1)), (2(M+1), 2M), \\ 1 & i = j \\ 0 & \text{otherwise} \end{cases} \tag{2.25}$$

then

$$\left(\overrightarrow{\mathbf{p}}(t_j^+) \right) = [\mathbf{R}] \left(\overrightarrow{\mathbf{p}}(t_j^-) \right) \tag{2.26}$$

The solution of Eq. (2.1) for the described system can be written as a modal

expansion,

$$\overrightarrow{\boldsymbol{\chi}}(t) = (C_1 + D_1 t)\overrightarrow{\boldsymbol{\zeta_1}} + \sum_{i=2}^{N} \overrightarrow{\boldsymbol{\zeta_i}} \left\{ C_i \cos(\omega_i t) + D_i \sin(\omega_i t) \right\} \tag{2.27}$$

where ω_i and $\{\overrightarrow{\boldsymbol{\zeta_i}}\}$ are easily determined solutions of the free response problem

$$\left[[K] - [M]\omega_i^2 \right] \{\overrightarrow{\boldsymbol{\zeta_i}}\} = \{\overrightarrow{0}\} \tag{2.28}$$

and the matrices $[K]$ and $[M]$ store the usual stiffness and mass.

Algorithm 1 provides the solution flow for generating analytical solutions. For both ID and IV cases, the system starts at with zero initial conditions for all masses except the first mass. With these initial conditions, Eqs. (2.27) are evaluated up until a time at which impact occurs (the clearance gap closes at time t_1 when $x_m(t_1) - x_{M+1}(t_1) = g_0$). The reset map is then used to reinitialize system starting conditions, followed again by evaluation of Eqs. (2.27)-(2.28). This process repeats until the final impact in the system occurs. After this impact, the solution flow is determined via Eq. (2.27), at which point system oscillations are sustained *ad infinitum*. Typically, only the impact times t_j and the states of the impacting masses are saved for later presentation.

This section generates analytically-predicted steady-state results for the system's response quantities (displacements and voltages), and compares these quantities to those obtained using both numerical and experimental means. The frequency response of the combined harvester/plate system is also studied, and an analysis of the

$t_j^+ = 0$

solve $\begin{cases} \dot{\vec{p}} = \boldsymbol{F}(\vec{p}) \\ \vec{p}(t=0) = \vec{p}(t_j^+) \end{cases}$

if $x_M - x_{M+1} = g_0$

$- \left(\vec{p}(t_j^+)\right) = [\boldsymbol{R}]\left(\vec{p}(t_j)\right)$

$-$ Find t_j

$-X_j = x_M(t_j^+)$

Else

$-$ *Return* X_j, t_j

$-$ *Break*

End

Algorithm 1. Step by step procedure for solving the equations of NES

electrical resistance needed to optimize harvested power is presented.

2.4 Results

This section first presents a verification of the analytical and numerical solutions of the governing equations. Following the verification, optimization studies are detailed which find system parameters leading to large trapped energy in the third subdomain (termed mechanical optimization) and large harvested energy (termed electrical optimization). Qualitative behavior of the system is also explored using Poincaré sections, bifurcation diagrams, and a closed-form, approximate Poincaré map.

2.4.1 Comparison of analytical and numerical simulations

The first results presented compare analytical predictions to those from direct numerical simulation of the governing equations. The parameter set employed for the comparisons is given in Table 2.1, where it is noted that a harvester is not present.

Table 2.1: ***Input parameters used to compare the analytical and numerical solution methods.***

Parameters	k_A	k_B	k_C	e	gap	R_l	θ
Values	10	10	20	1	0.5	0	0

Figure 2.4 illustrates the trapped energy as a function of time for both approaches. For the chosen parameter set, the figure clearly illustrates energy gained during two impacts. The figure also documents good agreement between the analytical and numerical predictions. Figure 2.5 compares responses predicted for the second subdomains contacting mass, which is a critical mass in the system as it drives much of the complex system behavior. Very good agreement is again noted.

2.4.2 Mechanical optimization

This section explores mechanical optimization of the considered system for which a maximum amount of energy can be trapped in the third subdomain, regardless of the harvester parameters. Following mechanical optimization, additional considerations are presented to optimize the electrical harvester. Mechanical optimization is accomplished through numerical solution of Eqs. (2.1)-(2.10) for multiple contact, excitation, and final-mass end conditions listed in Table 2.2. It should be noted that

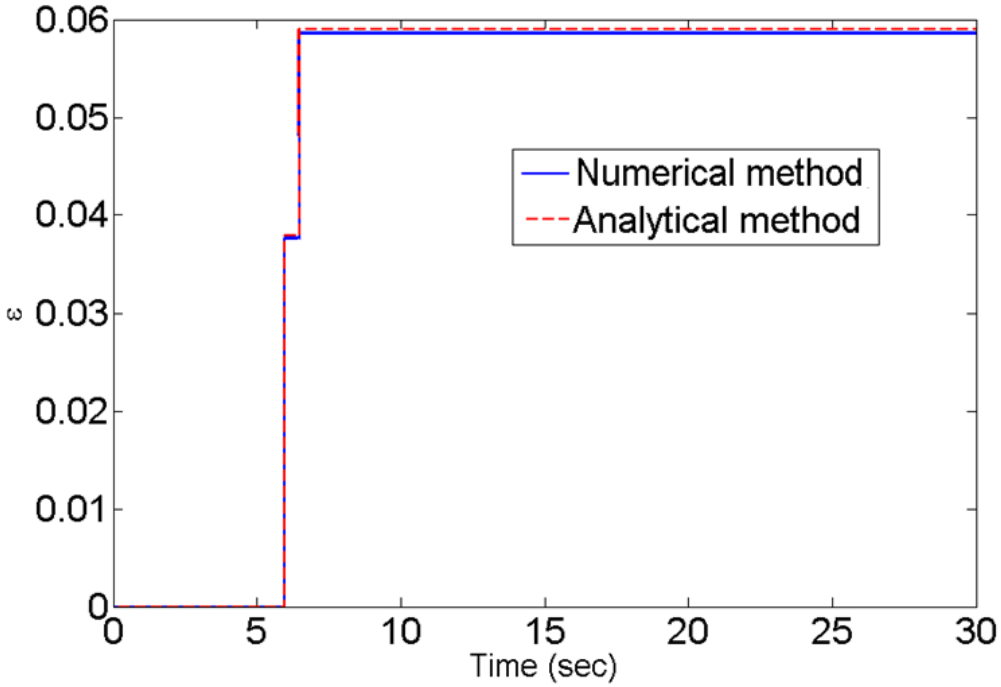

Figure 2.4: ***Trapped energy as a function of time for the analytical and numerical methods.***

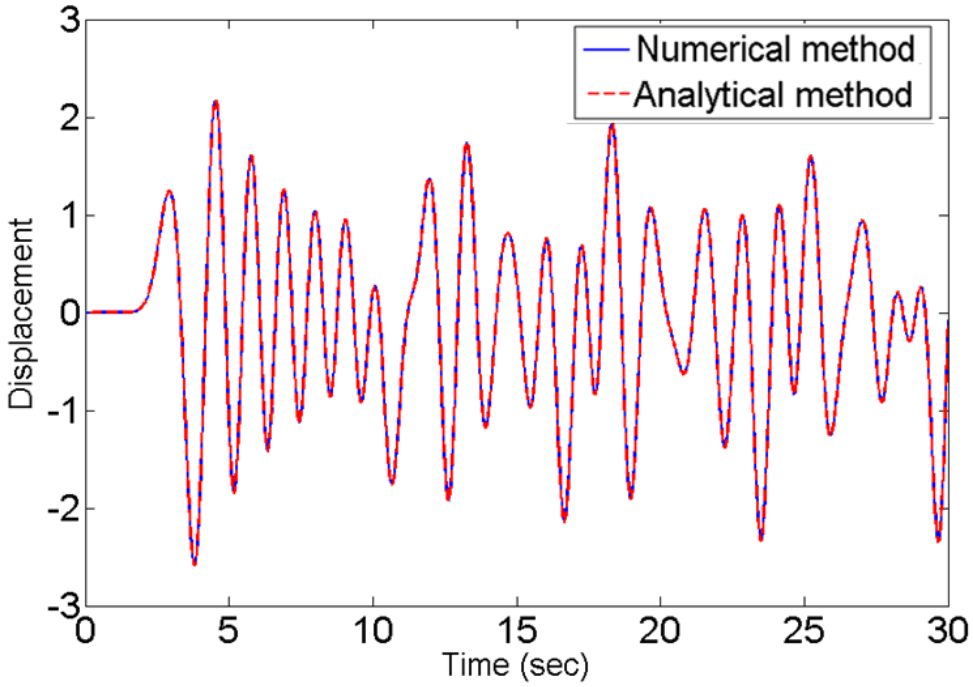

Figure 2.5: ***Contacting mass displacement as a function of time.***

when the final mass is fixed, an initial velocity excitation is not considered. This form of excitation imparts to the system an initial momentum, which in the absence of external forces, monotonically shifts the center of mass of first two subdomains as time progresses. Consequently, it closes the gap distance between the second and third subdomain such that trapping energy in the third subdomain becomes nearly impossible. Numerical solutions, together with MATLABs optimization toolbox, are used for the optimization since an analytical solution to a system with a contact spring is not readily available. The mass and stiffness of the first subdomain is considered to be fixed, while the second subdomain is considered to be of fixed mass and variable stiffness. Its purpose is to provide an impedance transition before the disturbance propagates across the clearance. The third subdomain, and the contact spring (when present), also have a variable stiffness. Finally, the optimization considers the gap distance and the input energy (as quantified by χ or ζ) to be variable and subject to optimization. Note that by optimizing input energy, the full potential of the system with a clearance-type energy sink is assessed rather than its potential for a single, arbitrarily-chosen input energy.

Table 2.2: ***Simulation cases considered (with and without gap).***

Case	Initial Condition	Last mass	Gap	$N_A = N_B = N_C$	Approach
1	Displacement	Fixed	Yes	10	GS
2	Velocity	Free	Yes	10	GS
3	Displacement	Fixed	Yes	10	CoR
4	Velocity	Free	Yes	10	CoR
5	Displacement	Fixed	No	10	No Gap
6	Velocity	Fixed	No	10	No Gap

Figure 2.6 exhibits the optimal trapped energy as a function of stiffness ratios $\kappa_B =$

k_B/k_A , $\kappa_C = k_C/k_A$ for an initial displacement excitation using a gap spring to model the clearance joint. Similar trends are seen in initial velocity excitation. Two general classes of optimization techniques (gradient and non-gradient) are used to ensure the results are independent of the optimization technique chosen. Although there is strictly one optimized value for both ratios which yields the most trapped energy, fixing one ratio and optimizing on all others reveals impact trends important for interpreting system behavior. For example, the figure reveals a non-smooth behavior (jumps leading to peaks) in the optimized trapped energy versus stiffness ratios. Rational for this behavior is provided in Figure 2.7 where the trapped energy is plotted as a function of time for several values of κ_B. Note that energy is only transferred during short intervals of time corresponding to impact, and thus the trapped energy appears as straight lines interrupted by jumps. The first vertical jump is the same for all of cases (i.e., the first impact occurs at the same time for all κ_B). For $\kappa_B = 2$, there is only the initial impact; for other values, multiple impacts occur. At the global optimal value ($\kappa_B = 1.7$, see Figure 2.7) the most trapped energy and the highest number of impacts occur. For stiffness ratios above this value, displacements of the contacting mass in subdomain 2 do not have sufficient amplitude to bridge the clearance gap, and performance of the device degrades.

Table 2.3 summarizes the global optimized parameters from the four cases in Table 2.2 containing clearance gaps, while Figure. 2.8 compares the trapped energy over time for each optimized case. This plot demonstrates that, in all four cases, the optimal configurations trap energy using a single impact.

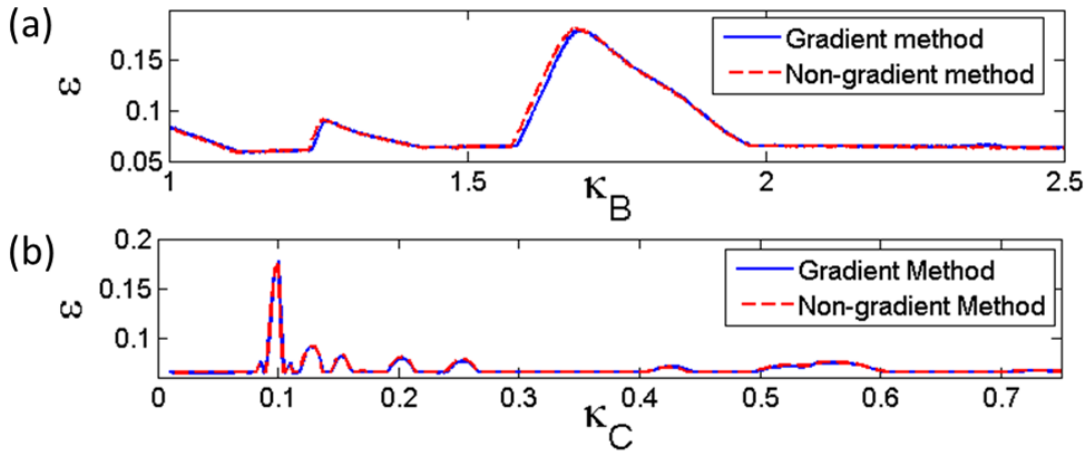

Figure 2.6: ***Comparison of the optimal values of (a)*** κ_B ***and (b)*** κ_C ***for gradient and non-gradient optimization methods.***

Table 2.3: ***Optimal values of parameters in the system.***

Case	ω_1^2	κ_B	κ_C	κ_g	η	ε
1	10	1.7	0.1	3	0.25	0.18
2	10	1.0	1.0	1	0.006	0.62
3	2.8	3.0	1.6	-	0.25	0.15
4	3	2.3	2	-	0.003	0.65

2.4.3 Electrical optimization

Next, the electrical parameters are included in the optimization with the goal of harvesting the largest non-dimensional harvested energy μ. Note that all six cases from Table 2.2 are included. The results from all cases are displayed in Table 2.3, which reports the optimal values of resistance and θ (coupling coefficient) for each case. From Table 2.4, it is clear that the value of resistance, for the set of chosen parameters,

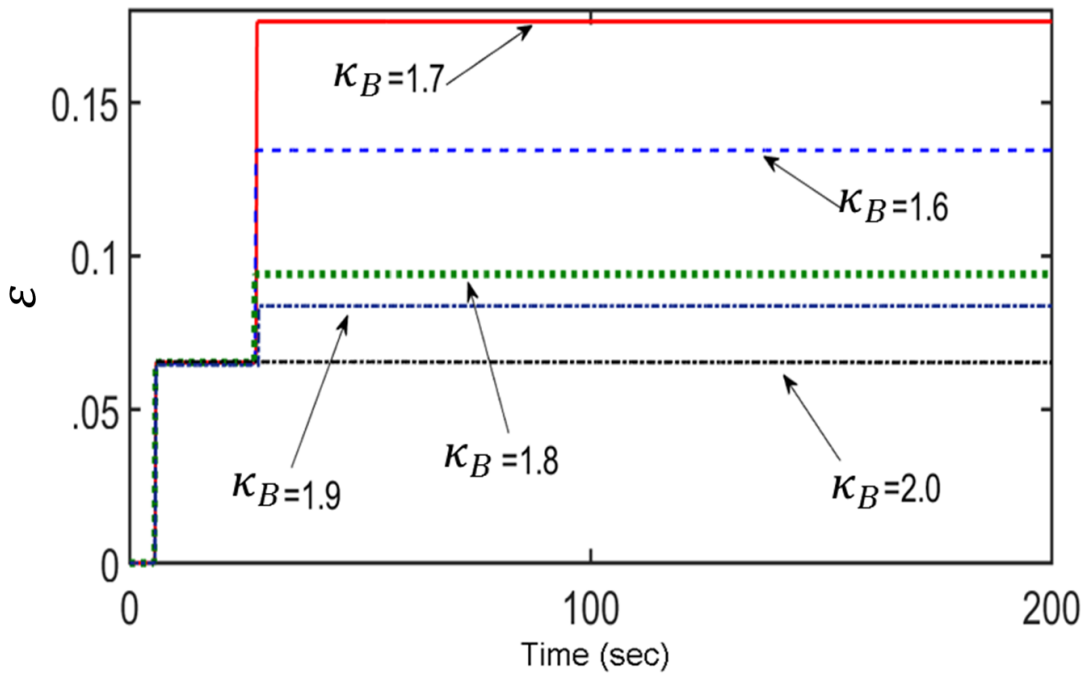

Figure 2.7: ***Comparison of different values of*** κ_B ***for optimal parameters and different numbers of impact.***

should be approximately 0.01 Ohms for GS and approximately 0.5 Ohms for the CoR gap model. The optimal values of θ for systems with a gap are nearly the same for all the cases except the first case. The harvested energy in the 2nd case is the greatest, while in the 5th case it is the lowest. Inspection of the electrical optimization results in Table 2.4 reveals that the optimal values for produced electrical energy for different gap models (CoR or GS) are close to the results from the mechanical optimization. This is due to the fact that the addition of the harvester does not appreciably change the subdomains impedance. Thus the electrical components do not appreciably affect the mechanical parameters and can be independently assigned. For the system without gap, a non-reflecting boundary condition is used for the first mass to avoid having the wave return to the system after one cycle of propagation. This choice is

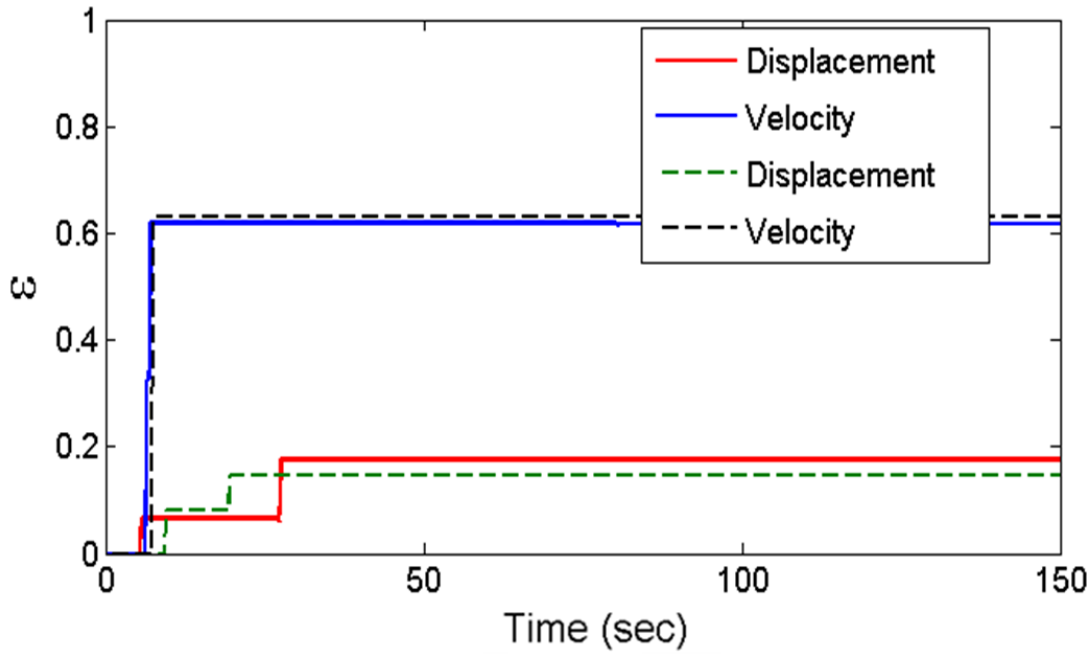

Figure 2.8: ***Comparison of percent of trapped energy over time for ID and IV conditions (solid lines show the system with GS and dashed lines show the system with CoR of modeling gap).***

motivated by applications, such as depicted in Figure. 2.1, where it is expected that reflected energy returns to a large reservoir-like domain, where diffusion, boundary interactions, and loss mechanisms are responsible for preventing an appreciable return of coherent energy.

Table 2.4: ***Optimal values of parameters in the system.***

Case	κ_B	$R_l(Ohms)$	θ	δ, ν	κ_C	μ
1	1.7	0.05	1.5	1	0.1	0.16
2	1	0.015	25	1	1.2	0.47
3	3	0.5	2	1	1.6	0.14
4	2.3	0.4	3.5	1	2	0.44
5	1	0.05	28	1	1	0.11
6	1.1	0.1	28	1	1	0.13

Note from Table 2.4 that in all cases, the presence of the clearance-type nonlinearity increases (by as much as 300 %) the amount of non-dimensional harvested energy as compared to cases where the nonlinearity is not present. Further, it is found that models approximating impact as departing initial velocity (as is standard in most treatments) result in larger harvested energy than cases treating impact with an initial displacement. This trend is also verified in Figure. 2.9, which plots the time-history of the last mass, which carries the harvester, and the voltage of the harvester patch. The voltage of the harvester begins to trap the energy of subdomain C as soon as wave front reaches the mass, which for all cases is roughly 10 seconds after inputting energy to the system. Figure 2.9 indicates that the peak of voltage with ID and gap is higher than other cases since more energy is transferred to subdomain C. For the case with initial displacement and no clearance gap, the lowest amount of power is realized (see Table 2.4). As can be expected, this case requires the largest optimal resistance due to the short duration of time over which the harvester can generate power.

2.4.4 Qualitative behavior of the system

This section explores qualitative behavior of the electromechanical system incorporating the nonlinear energy sink using the analytical approach and optimized parameters. Note that analytical solutions can only be formulated when modeling the gap using a coefficient of restitution. Starting with the case of initial displacement energy input, flow trajectories are presented in Figure. 2.10, with and without the harvester. The vertical axis is the voltage of the harvester while the other axes are the displacement

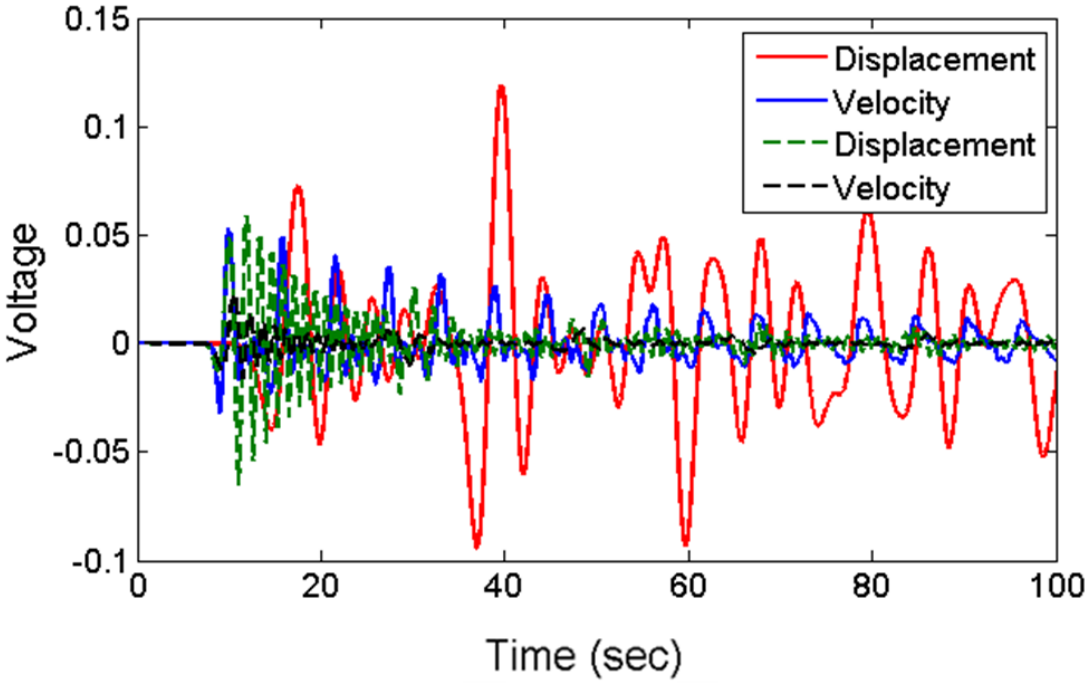

Figure 2.9: ***Change of output voltage for ID and IV conditions with GS modeling of gap (solid lines show the system with gap while dashed lines show the system without gap).***

and velocity of mass (N-1) attached to the harvester, respectively. Studying the sub-figure (Figure 2.10b), which projects the trajectories onto the voltage-velocity plane, reveals that the relationship between the voltage of the harvester and the velocity of the $(N-1)_{th}$ mass is linear as expected (recall that in the ID cases, the last mass is fixed).

Figure 2.11 illustrates the 3-D trajectory for the flow when the excitation is an initial velocity. As evident in the 2-D plot for the flow, contrary to the previous case, the relationship between the voltage of the harvester and the velocity of the $(N-1)_{th}$ mass is not linear. Instead, the N_{th} mass is not fixed, and the voltage of the harvester depends on the relative velocities of the $(N-1)_{th}$ and N_{th} masses. Trajectories in the three-dimensional state space resemble closed curves with smaller

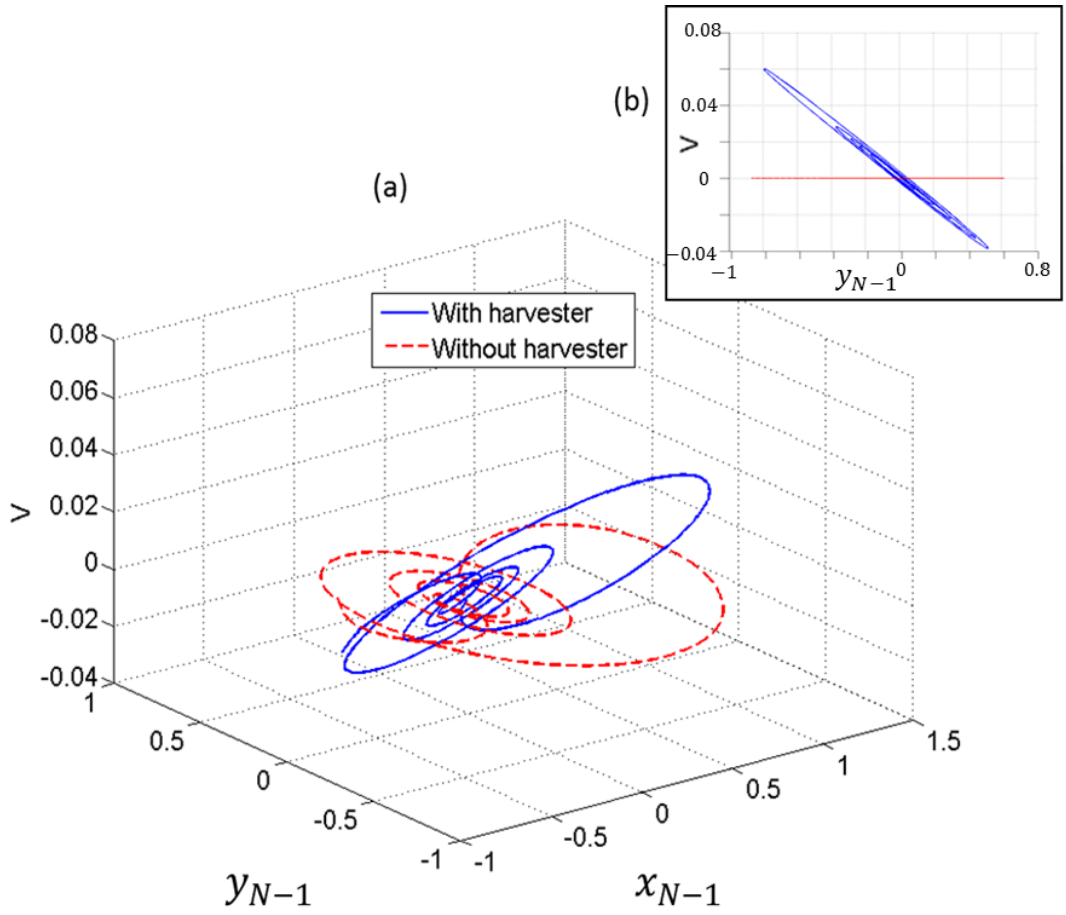

Figure 2.10: ***(a) 3-D Trajectory of the flow for the case ID (b) the 2-D view of the flow (x-axis is the velocity of the*** $(N-1)_{th}$ ***mass and y-axis is the voltage of the harvester).***

height as time progresses, and as a result, the radius of the curves decrease with time as energy is harvested. This figure clearly shows that the optimized electrical resistance is small such that the nearly-closed curves return to the trajectories of the case without harvester, at zero voltage.

Studying the impact masses also reveals important qualitative information about the system behavior. Figure 2.11 exhibits the M_{th} masss trajectories through state space. Note that this is the contacting mass from the second subdomain. Figure 2.12a shows the trajectories for ID, while 2.12b shows the trajectories for IV. As observed in

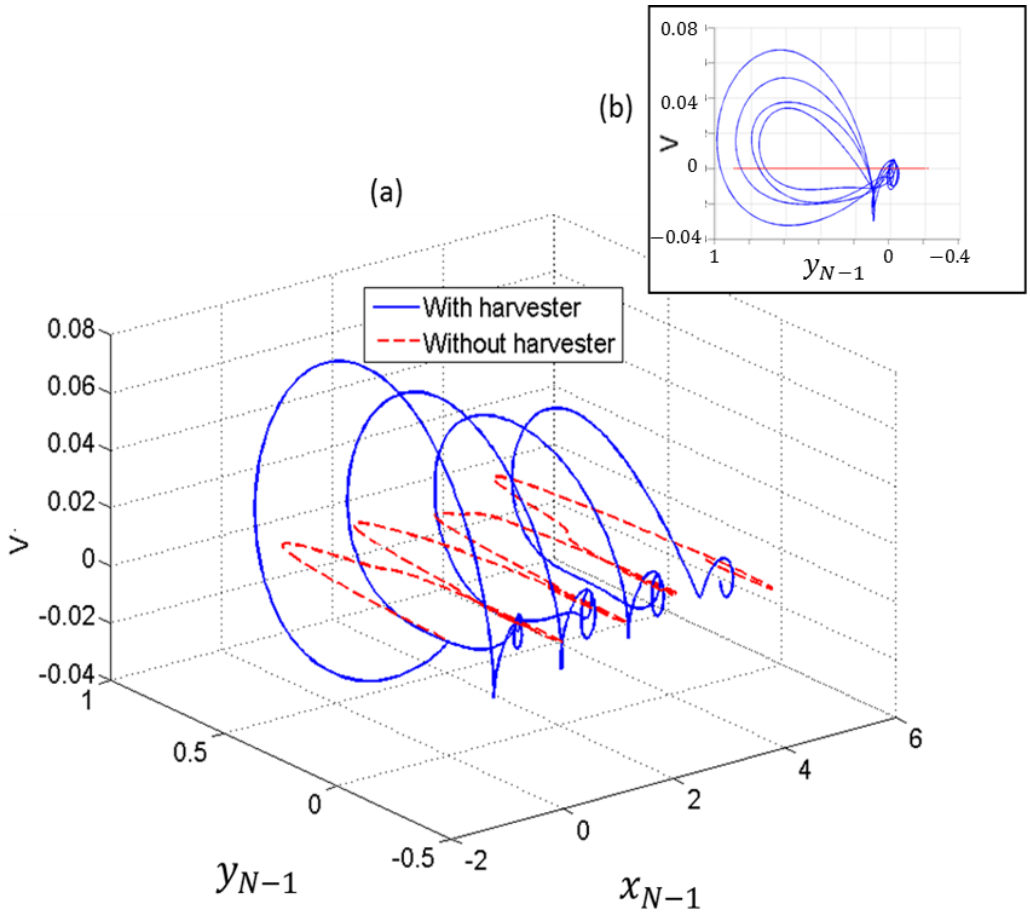

Figure 2.11: ***(a) 3-D Trajectory of the flow for the case IV (b) the 2-D view of the flow (x-axis is the velocity of the (N-1)th mass and y-axis is the voltage of the harvester***

the ID case, two velocity jumps occur for the case with a harvester, while three occur without a harvester. For both cases, the first two impacts occur before a wave can reach the harvester and reflect back to the clearance. Therefore the flow up to, and just beyond, the second impact is identical. The case without a harvester has a third impact due to the larger system energy, and afterwards, the trajectories of the M_{th} mass begin to differ (slightly) from the case with an absent harvester. In this case, the third impact is nearly grazing. Figure 2.12b illustrates the 2-D trajectory of the flow for the velocity of the M_{th} mass versus the displacement for initial velocity excitation.

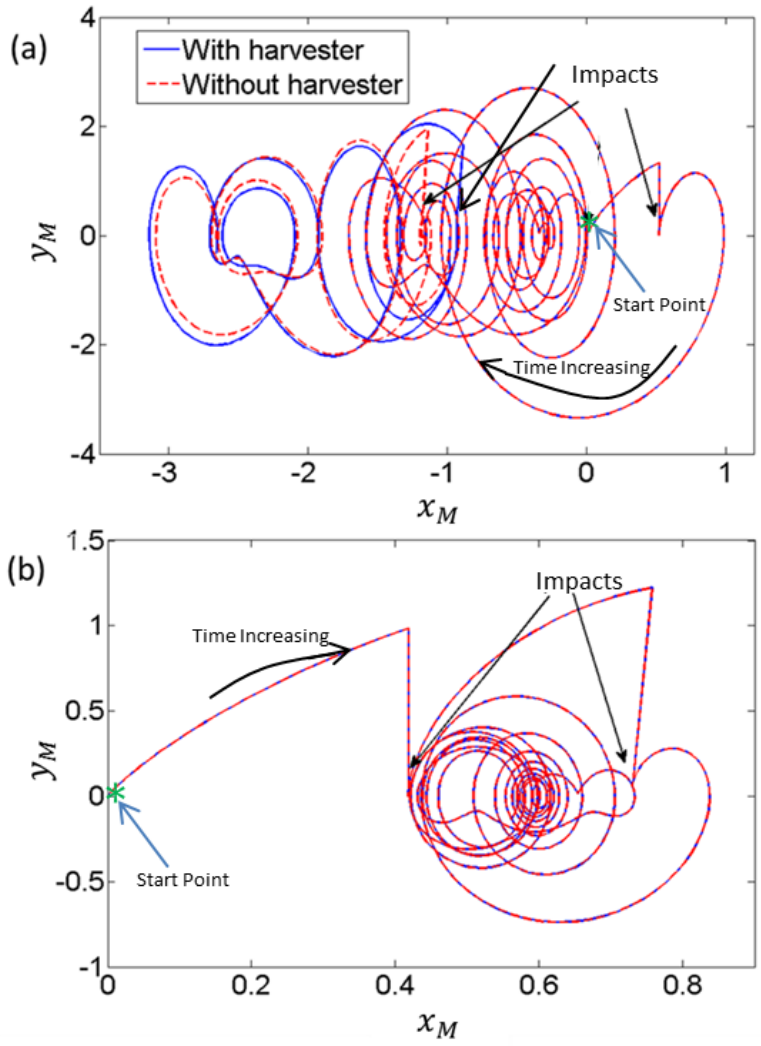

Figure 2.12: ***2-D Trajectory of the flow for a) ID excitation b) IV excitation (jumps in the plot show the time when impacts occur).***

In this case, only two impacts occur and the trajectories of the M_{th} mass are identical, with and without harvester. Note that the first mass of the third subdomain does not have identical behavior due to the presence or absence of the harvester.

Bifurcation diagrams, generated using the analytical solution for both initial displacement and initial velocity energy input, reveal additional qualitative behavior of the system with a clearance gap. Figure 2.13 displays these bifurcation diagrams in which the initial displacement/velocity δ/ν appear on the horizontal axis, and the

displacement of the M_{th} mass appears on the vertical axis. The number of total impacts is conveyed by the number of displacements x_M recorded for each point on the horizontal axis; each color represents a unique impact such that the first impact is denoted by a blue point, the second by green, the third by red, and so forth. Inspecting both Figures. 2.13a and 2.13b, over a large range of initial displacement/velocity, it can be seen that the number of impacts, on average, grows linearly with displacement/velocity. However, close inspection (see inset figure) reveals that the number of impacts is constant over small ranges of initial displacement/velocity, and then experiences jumps. Further, it must be that the first impact always occurs at the same value of x_M, equaling g_0. Note also that for ID, for energy input where at least four impacts occur, the last impact value of x_M always occurs at a negative displacement, with this value becoming more negative with increasing δ. For IV, all impacts occur at positive x_M displacements. Finally, the last and the second-to-last impact displacements of the M_{th} mass (for ID), and the final impact displacement (for IV), also grow linearly with displacement/velocity. It can be noted that, for ID, the negative (last) and positive boundary slopes (second-to-last) of the populated impacts seen Figure 13a are equal in magnitude.

As shown in Figure. 2.14, systems with a harvester exhibit similar bifurcation behavior. The major difference between the cases with and without harvester is the density of the impact locations and the slope of the bifurcation diagram. With a harvester, less energy in the system survives after each impact and thus the displacement of the mass at subsequent impacts is less than the cases without a harvester. As a result, the bifurcation diagrams increase in density (number of impacts for a given

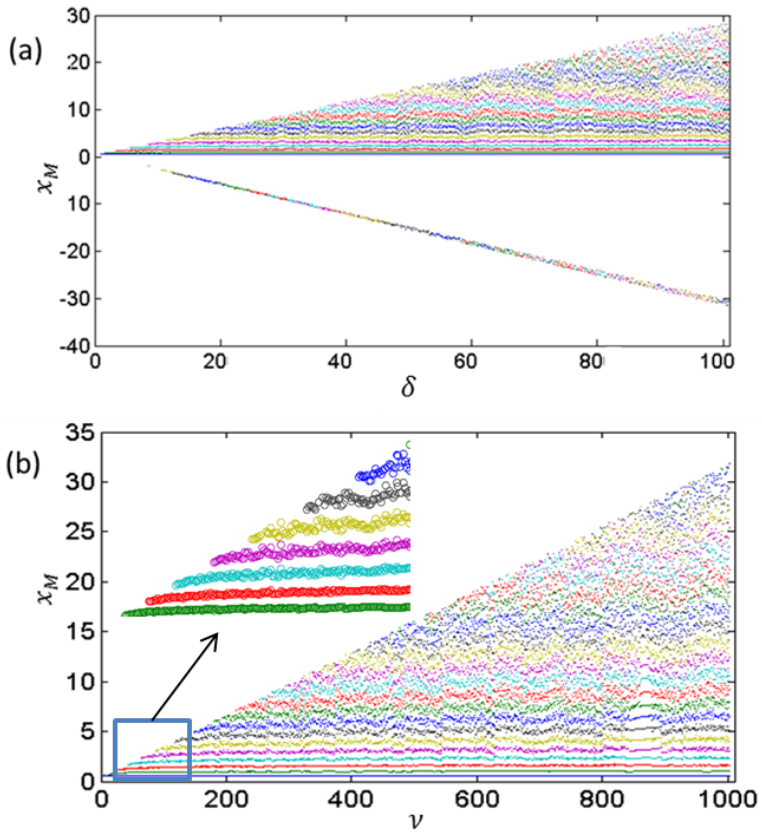

Figure 2.13: ***Bifurcation diagram without harvester for a) ID excitation (only one impact at negative position) and b) IV excitation (all impacts at positive positions).***

x_M range) and the boundary slope of populated impacts decreases.

The linear growth trends for impact number and impact x_M discussed above can be predicted through further analysis, as shown next for the case of ID. A similar analysis holds for IV, but is not provided. First, Eqs. (2.28-2.29) are rewritten distinguishing the first two subdomains from the third,

$$\overrightarrow{\boldsymbol{x}}_{A,B}(t) = (C_1 + D_1 t)\overrightarrow{\boldsymbol{\zeta_1}} + \sum_{i=2}^{M} \overrightarrow{\boldsymbol{\zeta_i}} \{C_i \cos(\omega_i t) + D_i \sin(\omega_i t)\} \tag{2.29}$$

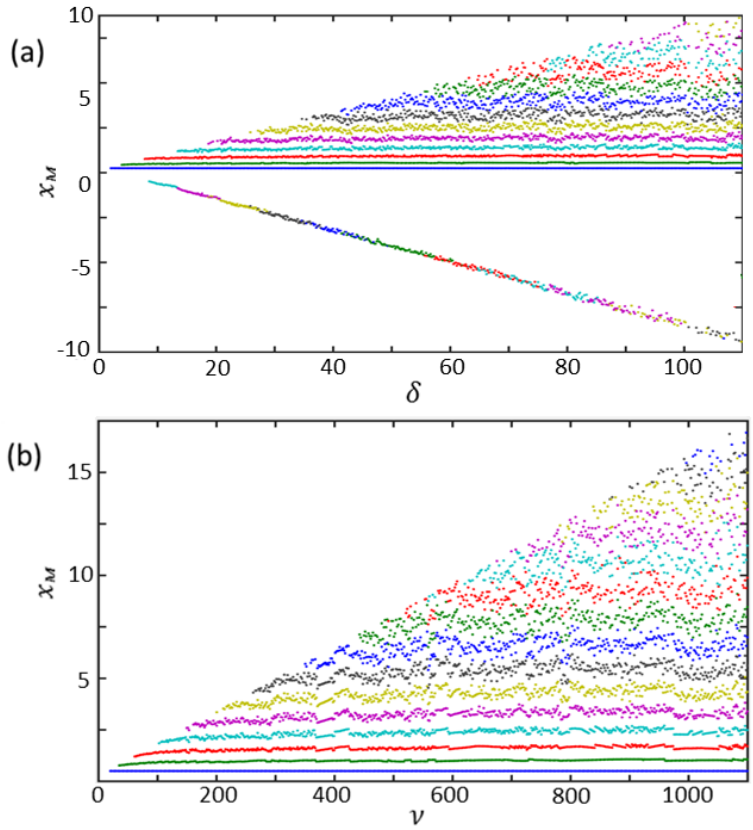

Figure 2.14: ***Bifurcation diagram with harvester for a) ID excitation (only one impact at negative position) and b) IV excitation (all impacts at positive position).***

and

$$\overrightarrow{\boldsymbol{x}}_C(t) = \sum_{i=M+1}^{N} \overrightarrow{\boldsymbol{\zeta_i}} \{C_i \cos(\omega_i t) + D_i \sin(\omega_i t)\} \tag{2.30}$$

where $\overrightarrow{\boldsymbol{x}}_A$, $\overrightarrow{\boldsymbol{x}}_B$, and $\overrightarrow{\boldsymbol{x}}_C$ hold the displacements in subdomains A, B, and C, respectively, and C_i and D_i denote Fourier coefficients. It is noted that the third subdomain does not have a rigid body mode due to fixing of the last mass. The first impact occurs when the last element of $\overrightarrow{\boldsymbol{x}}_{A,B}$ is equal to the gap distance g_0. Initial conditions for each mass in the first two subdomains provide the other conditions to

complete specification of all Fourier coefficients C_i and D_i, and the first impact time t_1. The initial conditions first yield that each Fourier coefficient is proportional to the nondimensional displacement,

$$C_i = \delta\alpha_i, \;\; D_i = \delta\beta_i \tag{2.31}$$

for multipliers α_i and β_i found by setting $t = 0$ in Eq. (2.29) and solving for C_i and D_i in terms of δ using the following,

$$\begin{Bmatrix} C_1 \\ D_1 \\ . \\ . \\ . \\ C_M \\ D_M \end{Bmatrix} = \begin{bmatrix} 1 & 0 & \dots & \zeta_{M,1} & 0 \\ 0 & 1 & \dots & 0 & \zeta_{M,1}\omega_M \\ \vdots & \vdots & \vdots & \ddots & \vdots \\ 1 & 0 & \dots & \zeta_{M,M} & 0 \\ 0 & 1 & \dots & 0 & \zeta_{M,M} \end{bmatrix}^{-1} \begin{Bmatrix} \delta \\ 0 \\ . \\ . \\ . \\ 0 \\ 0 \end{Bmatrix} \tag{2.32}$$

Substituting Eq. (2.31) into Eq. (2.29) with the first impact condition provides the final expression for impact time t_1,

$$(\alpha_1 + \beta_1 t_1)\zeta_{1,M} + \sum_{i=2}^{M} \zeta_{i,M} \left\{\alpha_i \cos(\omega_i t_1) + \beta_i \sin(\omega_i t_1)\right\} = \frac{g_0}{\delta} \tag{2.33}$$

Importantly, Eq. (2.33), incorporates δ, which facilitates quantifying the slope trend seen in Figure. 2.14a. Thus $t_1 = f_1(\frac{g_0}{\delta})$ and it can be noted that the impact times

decrease with increasing δ.

After finding the first impact time t_1, the process for finding all other impacts is similar, except the third subdomain must now enter the solution procedure. The system of equations (2.29 - 2.30) is reinitialized (i.e., a new time begins from zero). All positions and velocities at the new time start from their values at t_1, except the velocity of the contacting masses, which change by using the definition of the CoR, Eqs. (3.3). To facilitate the analysis, a new coordinate is defined for all masses in the first and second subdomains by setting their zero position at the first impact location. This removes g_0 from the expressions analogous to Eqs. (2.29) and (2.32), and thus conditions (2.31) reoccur *ad infinitum* due to the reappearance of δ as the only parameter in the system. Since the displacement of the first mass of the last subdomain is known at the first impact, Eq. (2.30) can be solved to find the time of the second impact. Further, since both sides have δ terms, they cancel, and the final form of the impact condition is,

$$\alpha_1 + \beta_1 t_1 + \sum_{i=2}^{M} \zeta_{i,M} \left\{ \alpha_i \cos(\omega_i t_1) + \beta_i \sin(\omega_i t_1) \right\} =$$

$$\sum_{i=M+1}^{N} \zeta_{i,M} \left\{ \alpha_i \cos(\omega_i t_1) + \beta_i \sin(\omega_i t_1) \right\} \tag{2.34}$$

Since the time of each impact is small for small initial displacements, a Taylor

expansion of the above equation yields an expression for t_2,

$$\alpha_1 + \beta_1 t_2 + \sum_{i=2}^{M} \zeta_{i,M}(\alpha_i + \beta_i t_2) = \sum_{i=M+1}^{N} \pm\zeta_{i,M}(\alpha_i + \beta_i t_2)$$

$$\rightarrow t_2 = \frac{\alpha_1 + \sum_{i=2}^{N} \pm\zeta_{i,M}\alpha_i}{\beta_1 + \sum_{i=2}^{N} \pm\zeta_{i,M}\beta_i\omega_i} \tag{2.35}$$

Finally, substituting the impact time t_2 into Eq. (2.29) yields the position of the last mass of the second subdomain at impact via,

$$x_m \cong \delta \left[\alpha_1 + \beta_1 t_2 + \sum_{i=2}^{N_A+N_B} \zeta_{i,M}\{\alpha_i \cos(\omega_i t_2) + \beta_i \sin(\omega_i t_2)\} \right] \tag{2.36}$$

Note that δ cancels from the right-hand side of Eq. (2.36) due to the definitions in Eq. (2.31). Importantly, it is noted that Eqs. (2.35) and (2.36) compose an approximate, closed-form Poincaré map taking one impact location to the next, $\phi_i : x_M(t_i) \in \Sigma \rightarrow x_M(t_{i+1}) \in \Sigma$. This map greatly simplifies the analysis and provides a complete picture of dynamics on simply by iterating on the known impact times. It can also be used to generate further bifurcation studies (grazing, etc.) beyond the scope of the present paper. Algorithm 2 provides the map in procedural form, starting with a known value for t_1 found using Eq. (2.33).

Based on Eq. (2.36) and Figure. 2.13, it can be concluded for the n_{th} impact that the position x_M is not a function of input energy (i.e., δ) and is nearly the same for all values of input initial displacements. The number of impacts depends on the

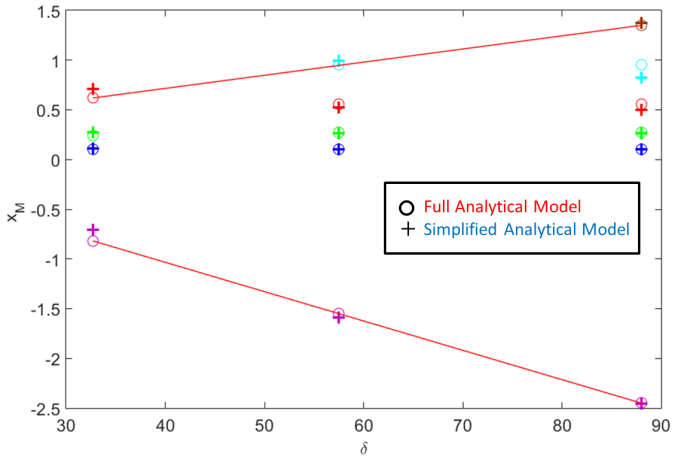

Figure 2.15: ***Comparison of results using exact analytical method and approximate Poincaré map.***

magnitude of excitation, as it specifies whether or not Eq. (2.34) has a solution at the next impact. Both observations are verified in Figures. 2.13 and 2.14 where the x_M locations form nearly straight lines with respect to the bifurcation parameter δ, with the number of lines increasing with increasing δ. Figure 2.15 directly compares impact displacements x_M predicted by the full analytical method (i.e., Algorithm 1) with slope behavior predicted using the approximate Poincaré map and three values of nondimensional impact δ. It is evident from the figure that the boundary slopes of populated impacts (i.e., top and bottom lines in the figure) agree well with the full analytical model. In addition, predicted impacts x_M are in close agreement (see agreement in circular and plus markers).

2.5 Experimental Setup and Apparatus

The clearance-type nonlinearity is also explored herein using a simple experimental setup based on an air track, an electromagnet, an impact hammer, and laser Doppler vibrometers (as shown in Figure. 2.16). The experimental setup is limited to off-the-shelf components available to the authors, to include two different sliding masses produced by the air track manufacturer, and coil springs available in a typical supply catalog. The intent is to demonstrate experimentally a harvesting benefit of incorporating the clearance-type NES into the system. As with the models detailed above, the experiment contains three different mass-spring subdomains (each containing three masses): subdomain A, where the first mass receives the excitation; subdomain B, which impacts subdomain C; and subdomain C, which terminates with a coil and magnet used to convert the trapped energy into electrical power using the resistance of the coil (measured to be 333 Ω). Displacements of the masses and the voltage of the coil are measured with two laser vibrometers (LDV: Polytec V-100), and a National Instrument NI data acquisition system (model cDAQ-9178), respectively, as pictured in Figure 16. An electrical piezoelectric hammer (PCB Model 086C03) is used to excite the system, producing an initial velocity for the first mass. One of the laser vibrometers measures this velocity. Alternatively, initial energy is imparted by compressing the first spring of the system. Using these initial excitations, the input energy is calculated via Eqs. (2.6)-(2.7). The air track provides a nearly-lossless propagation of the imparted energy through the subdomains, closely replicating the model studied. Ninety experiments were carried-out and used to report average data.

$t_j^+ = 0$

$X_j = 0$

while $X_j > 0$

$t_{j+1} = \phi_j(t_j^*)$

$\left(\vec{\boldsymbol{p}}(t_{j+1}^+)\right) = [\boldsymbol{R}]\left(\vec{\boldsymbol{p}}(t_{j+1})\right)$

$X_j = x_M(t_{j+1}^+)$

End

Return X_j, t_j

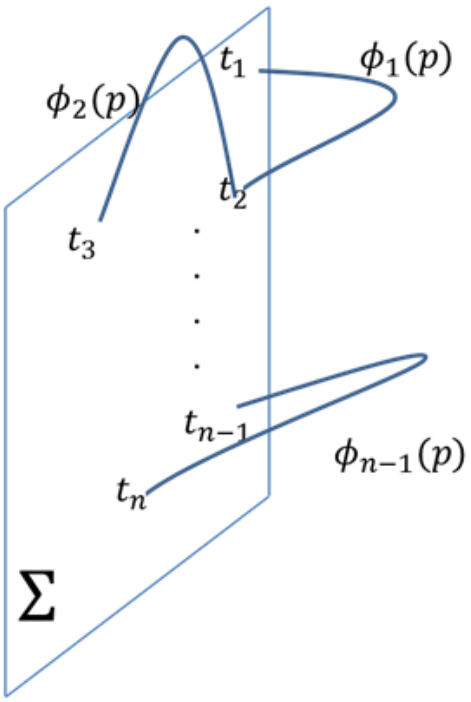

Algorithm 2. Approximate, closed-form Poincaré map

Thirty different scenarios have been tested to compare the harvested energy of the system with and without clearance gap, as follows. Five parameter cases composed of different springs and masses are listed in Table 2.5. For each parameter set, six subcases, as shown in Table 2.6, combine an excitation type (ID or IV), and a contact case (with spring between contacting masses, or missing a spring). The cases without a contact spring most-closely resemble analytical models employing a coefficient of restitution (assumed to be one).

Table 2.5: ***Parameter sets considered (with and without gap).***

Case	$\kappa_B = \frac{k_B}{k_A}$	$\kappa_c = \frac{k_C}{k_A}$	$m_A(gr)$	$m_B(gr)$	$m_C(gr)$
1	1	0.083	135	135	135
2	1	2	135	135	135
3	1	0.5	135	135	135
4	0.0833	0.0833	135	280	135
5	12.01	1	280	135	135

Table 2.6: ***Tested subcases considered (with and without gap).***

Subcase	1	2	3	4	4	6
Initial excitation	IV	ID	IV	ID	IV	ID
Gap modeling	CoR	CoR	GS	GS	No gap	No gap

Since the experimental setup uses off-the-shelf components not comparable to the optimized cases explored above, its purpose is to only realize the effectiveness of a clearance-type NES for enhancing wave energy harvesting. Experiments were carried out for each case listed in Table 2.5 and total energy produced in the coil was calculated from the obtained voltage data by using $E_{tot} = \int V^2/R\,dt$. Figure 2.17

Figure 2.16: ***The experimental setup, which includes 1-Magnet, 2-Coil, 3-NI data acquisition system, 4-impact hammer signal conditioner, 5-Laser Doppler vibrometers, 6-Impact hammer, 7-Air track.***

shows the percent of transferred electrical energy ($\mu = \frac{Transfered\ Electrical\ Energy}{Total\ Energy} \times 100$) for all cases. The resistance of the coil was measured to be 333 Ohms. Recall from Tables 2.5 and 2.6 that three different springs and two identical masses have been used in the experiment. Figure 2.17 clearly exhibits the benefits of using the clearance joint in enhancing wave energy harvesting. In nearly all cases, the harvested energy with the clearance NES exceeds that for the cases without the NES. To enhance the wave energy harvesting, the largest possible mechanical energy from the vibration of the system should be transferred through the clearance joint to the harvesters subdomain. To increase this wave energy, the impedance of the second subdomain

should be bigger than the impedance of the third. Increasing the impedance of the second domain is possible either by having a larger mass or spring stiffness. On the other hand, if the impedance of the second subdomain is equal to the third subdomain, i.e. $m_A k_A = m_B k_B$, the chance of producing electrical energy is less. For Case 5, the impedance of the second subdomain is much higher than the impedance of the third subdomain (e.g., larger mass), and thus more energy is transferred to the third subdomain through the clearance in comparison to other cases. In contrast, for the third and fourth cases, the impedance of the second and third subdomain are nearly the same resulting in less electrical energy harvested, as expected. Finally, it is noted from Figure 2.17 that the percentage of harvested electrical energy is more for cases with initial velocity excitation than initial displacement, except for Case 5, as discussed above. Moreover, the results for both GS (gap spring present) and CoR (gap spring absent) exhibit similar trends across cases, implying that the two approaches for realizing and modeling the clearance have little effect on its operation and effectiveness.

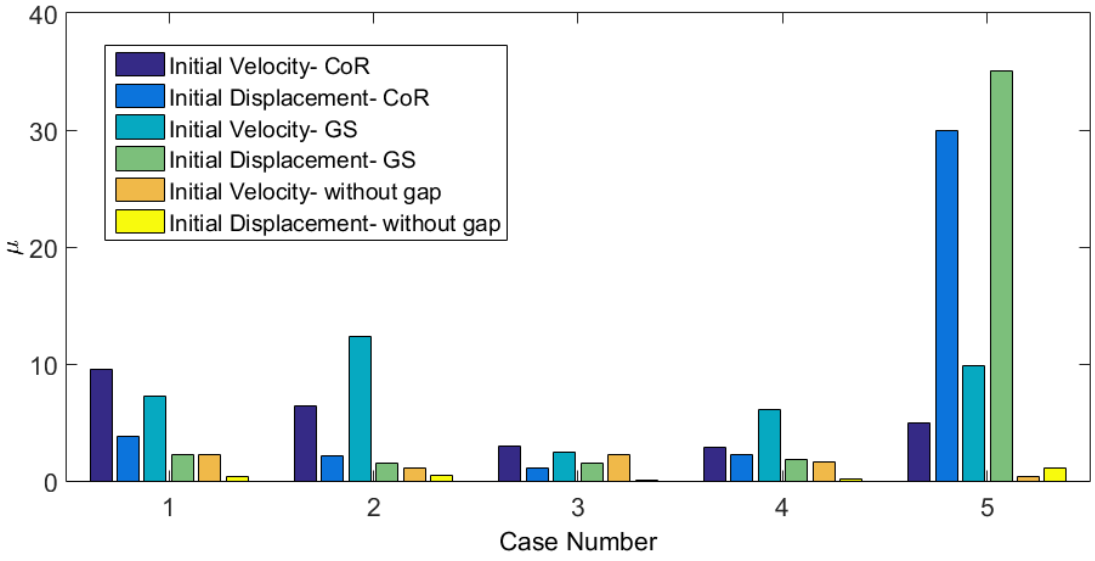

Figure 2.17: ***Percent of transferred energy for each experimental case.***

Chapter 3

Energy Harvesting in Piezoelectric Plate-Harvester Systems

3.1 Overview

Acoustoelastic wave energy harvesting in thin plates and other structures has recently gained attention from the energy harvesting research community. Metamaterial-inspired concepts for enhancing wave power generation have been investigated, including metamaterial funnels, mirrors, and defect-based resonators. In support of such concepts, this chapter introduces an analytical framework for predicting wave energy harvested by a circular piezoelectric disk attached to a thin plate. An harmonic point source excitation generates waves that are then incident on a piezoelectric disk - summing responses due to all such excitation enables general forcing profiles to be considered. The analysis approach decomposes the coupled system into two subdomains, one being the piezoelectric disk, and the other an infinite plate for which a Green's function is readily available. Interaction forces between the two subdomains couple the problems and lead to a closed-form solution for the propagation, transmission, and reflection of waves over the entire domain. In addition, the voltage generated by the harvester is calculated using coupled electromechanical equations.

The analysis approach is first validated by comparing predicted response quantities to those computed using numerical simulations, documenting good agreement. The

system is then studied in the frequency domain and the optimum harvester resistance is found for generating the most electrical energy. Representative experiments are carried out to demonstrate the validity of the analytical approach and verify the harvested energy versus resistance trend.

The chapter is organized as follows: first an analytical model is introduced for predicting the complete wave field of a system composed of a circular piezoelectric layer, attached to an infinite host layer, and subjected to point source excitation. The system model is then validated via transient simulations performed using COMSOL. Optimization of a coupled resistive circuit is also detailed. Guided by these studies, analytical and experimental results are then presented which compare the peak power generated by the system as a function of excitation frequency; very good agreement is documented.

3.2 System Model

Figure 3.1 depicts the system of interest and geometry necessary for model development. As illustrated, a circular piezoelectric disk with radius r_0 and thickness h_p is bonded to an infinite thin plate (i.e., the substrate) of thickness h_s. Cylindrical coordinates (r, θ), assigned to the middle of the piezoelectric disk, locate the point source and plate displacements. Harmonic, transverse excitation $F_0 e^{\hat{i}\omega t}$, located at (r_1, θ_1), generates the incident wave field. Since the Green's function governing the wave response of the plate to a harmonic point source excitation is well-known, the approach taken herein is to break the introduced system into two subdomains: one for

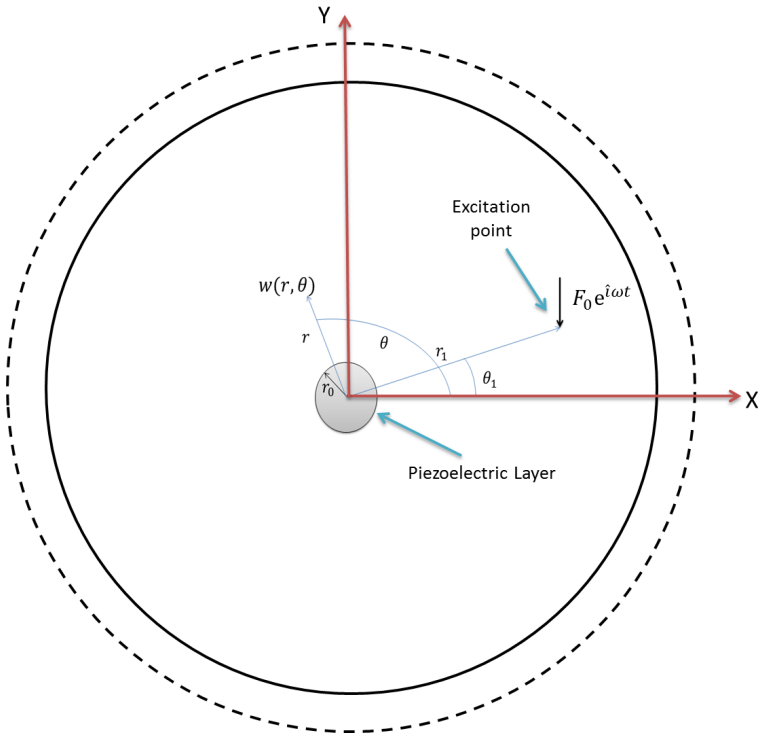

Figure 3.1: ***In plain schematic of the plate system with a piezoelectric energy harvester under the excitation of a harmonic force.***

the infinite plate, and the other for the piezoelectric disk. As depicted in Figure 3.2, each subdomain is then subject to equal and opposite interaction forces, in addition to the point force acting on the substrate. Since the piezoelectric disk is finite in extent, a modal approach is used for its modeling.

The substrate response is formed from the superposition of plate displacements due to the harmonic force excitation w_F, and displacements due to interaction forces w_f. For the piezoelectric disk, w_P captures displacements due to an equal-and-opposite set of interaction forces. Setting equal the response of both subdomains in the adjoining regions, the unknown distributed interaction forces between the piezoelectric and infinite layer can be identified. Expressing the substrate's displacement

as,

$$w_{plate}(r,\theta,t) = w_F(r,\theta,t) + w_f(r,\theta,t,f(r,\theta)), \tag{3.1}$$

and the disk's displacement as,

$$w_{disk}(r,\theta,t) = w_P(r,\theta,t,-f(r,\theta)), \tag{3.2}$$

then the adjoining condition requires

$$w_F(r,\theta,t,F) + w_f(r,\theta,t,f(r,\theta)) = w_P(r,\theta,t,-f(r,\theta))\Big|_{r<r_0}. \tag{3.3}$$

Displacement fields appearing in Eq. (3.3) require further development before returning to find the interaction forces.

Since the steady-state behavior of the system is desired at the excitation frequency ω, and the model is strictly linear, each displacement field can be written as,

$$w_\Gamma(r,\theta,t) = \phi_\Gamma(r,\theta)e^{\hat{i}\omega t}, \tag{3.4}$$

where subscript Γ can be either F, f, or P. Using the known Green's function, the displacement of the plate due to the harmonic point force is given as,

$$\phi_F(r,\theta) = \frac{F_0}{8BIk_B^2\hat{i}}[H_0^{(2)}(k_B\rho_1) - H_0^{(2)}(-\hat{i}k_B\rho_1)], \tag{3.5}$$

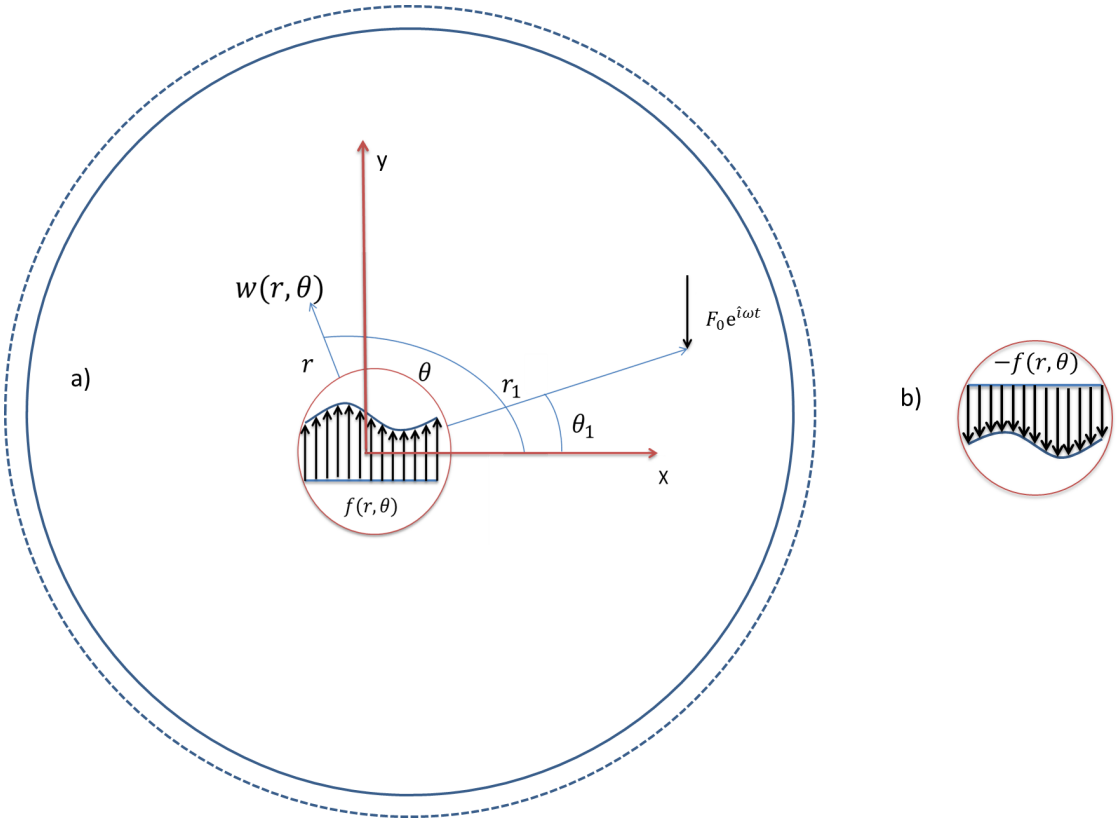

Figure 3.2: ***Schematic of a) the substrate without piezoelectric disk and b) isolated piezoelectric disk under the excitation of interaction forces***

where $\rho_1 = \sqrt{r_1^2 + r^2 - 2rr_1 cos(\theta - \theta_1)}$ denotes the distance between the source and any location (r, θ), $H_i^{(2)}$ denotes the Hankel function of the second kind at the ith order, $k_B = \frac{\omega}{c_B}$ the flexural wave number, $c_B = \sqrt[4]{\frac{B}{m}}\sqrt{\omega}$ the phase velocity of bending waves, $B = \frac{E}{1-\nu^2}$ the bending stiffness, E Young's Modulus, ν Poisson's ratio, $I = \frac{h_s^3}{12}$ the cross-sectional moment of inertia, and m the mass per unit area. The same Green's function can be used to find the response of the plate due to distributed interaction forces $f(r, \theta)$,

$$\phi_f(r,\theta) = \frac{1}{8BIk_B^2\hat{i}}\left(\int_0^{2\pi}\int_0^{r_0} f(r^*,\alpha)\Pi(k_B,\rho_0)\, r^* dr^*\, d\alpha\right), \tag{3.6}$$

where $\rho_0 = \sqrt{r^{*2} + r^2 - 2rr^* cos(\theta - \alpha)}$ denotes the distance between the distributed interaction force at (r^*, α) and any location (r, θ). In addition, $\Pi(k_B, \rho_0)$ is defined as

$$\Pi(k_B, \rho_0) = [H_0^{(2)}(k_B\rho_0) - H_0^{(2)}(-\hat{i}k_B\rho_0)]. \tag{3.7}$$

As illustrated in Figure 3.2, the final submodel captures the displacements of the piezoelectric disk resulting from the same interaction forces as used in Eq. (3.2). Considering an infinitesimal element of the circular disk in polar coordinates, the plate equations of motion can be derived in polar coordinates and are given as [51],

$$\frac{\partial M_r}{\partial r} + \frac{1}{r}\frac{\partial M_{r\theta}}{\partial \theta} + \frac{M_r - M_\theta}{r} - Q_r = 0, \tag{3.8}$$

$$\frac{\partial M_{r\theta}}{\partial r} + \frac{1}{r}\frac{\partial M_{r\theta}}{\partial \theta} + \frac{2}{r}M_{r\theta} - Q_\theta = 0, \tag{3.9}$$

$$\frac{\partial Q_r}{\partial r} + \frac{1}{r}\frac{\partial Q_{r\theta}}{\partial \theta} + \frac{Q_r}{r} + f - \rho_p h_p \frac{\partial^2 w}{\partial t^2} - c\frac{\partial w}{\partial t} = 0, \tag{3.10}$$

where $w(x, t)$ denotes the transverse displacement; M_r, M_θ and $M_{r\theta}$ represent the radial, tangential and twisting moments, respectively; Q_r and Q_θ denote radial and tangential forces, respectively; f holds any external forces exciting the system, ρ_p is the density of the disk; and c is the damping of the piezoelectric. The piezoelectric

moment resultants are given as,

$$M_r = -BI\Big[\frac{\partial^2 w}{\partial r^2} + \nu\Big(\frac{1}{r}\frac{\partial w}{\partial r} + \frac{1}{r^2}\frac{\partial^2 \theta}{\partial r^2}\Big)\Big] +$$

$$\hat{\theta} v(t)[H(\theta) - H(\theta - 2\pi)][H(r) - H(r - r_0)], \tag{3.11}$$

$$M_\theta = -BI\Big[\frac{1}{r}\frac{\partial w}{\partial r} + \frac{1}{r^2}\frac{\partial^2 \theta}{\partial r^2} + \nu\frac{\partial^2 w}{\partial r^2}\Big] + \hat{\theta} v(t)[H(\theta) - H(\theta - 2\pi)][H(r) - H(r - r_0)], \tag{3.12}$$

$$M_r = -BI(1-\nu)\frac{\partial}{\partial r}\Big(\frac{1}{r}\frac{\partial w}{\partial \theta}\Big) + \hat{\theta} v(t)[H(\theta) - H(\theta - 2\pi)][H(r) - H(r - r_0)], \tag{3.13}$$

where $H(x)$ denotes the Heaviside function, $v(t)$ the harvester voltage, and $\hat{\theta}$ is the electrostatic coupling term arrived at through consideration of the neutral axis of bending,

$$\hat{\theta} = \frac{\bar{e}_{31}}{4h_p}((h_p + \frac{h_s}{2})^2 - h_s^2/4), \tag{3.14}$$

and where $\bar{e}_{31}$ is the stiffness of the plate in the normal direction, h_p is the thickness of the piezoelectric disk, and h_s is the thickness of the substrate. Note that Heaviside functions are necessary since moment derivatives appear in the plate equations of

motion. Similarly, the shear force resultants can be expressed as,

$$Q_r = -BI\frac{\partial}{\partial r}(\bigtriangledown^2 w), \tag{3.15}$$

$$Q_\theta = -BI\frac{1}{r}\frac{\partial}{\partial \theta}(\bigtriangledown^2 w), \tag{3.16}$$

where

$$\bigtriangledown^2 = \frac{\partial^2}{\partial r^2} + \frac{1}{r}\frac{\partial}{\partial r} + \frac{1}{r^2}\frac{\partial^2}{\partial \theta^2}. \tag{3.17}$$

Finally, collecting Eqs. (3.8)-(3.17), the field equation governing vibrations of a circular piezoelectric disk is given as,

$$BI\ \bigtriangledown^4 w + \rho_p h_p \frac{\partial^2 w}{\partial t^2} - \hat{\theta} v(t)\frac{1}{r}P(r,\theta) + c\frac{\partial w}{\partial t} = f(r,\theta,t), \tag{3.18}$$

where

$$P(r,\theta) = \Big(\frac{\partial(\delta(r) - \delta(r-r_0))}{\partial r}\Big)\Big(H(\theta) - H(\theta - 2\pi)\Big) +$$

$$r\Big((\delta(r) - \delta(r-r_0)\Big)\Big(H(\theta) - H(\theta-2\pi)\Big) + 2r\Big(\delta(r) - \delta(r-r_0)\Big)\Big(\delta(\theta) - \delta(\theta-2\pi)\Big) +$$

$$2\Big(H(r) - H(r-r_0)\Big)\Big(\delta(\theta) - \delta(\theta-2\pi)\Big)$$

$$+2\Big(\frac{\partial(\delta(\theta)-\delta(\theta-2\pi))}{\partial\theta}\Big)\Big(H(r)-H(r-r_0)\Big). \tag{3.19}$$

Note that in the above equation, $\delta(x)$ represents the Dirac delta function and

$$v(t) = V_0 e^{\hat{i}\omega t}, \tag{3.20}$$

$$f(r,\theta,t) = \tilde{f}(r,\theta)e^{\hat{i}\omega t}, \tag{3.21}$$

where V_0 is the peak voltage of the piezoelectric energy harvester.

Using a separation of variables method [51], the solution of Eq. (3.18) is decomposed into the usual product of polar and radial basis functions ($e^{\hat{i}m\theta}$ and $J_m(\lambda_{mn}r)$) and accompanying coefficients η_{mn} using an inverse Hankel transform,

$$w(r,\theta,t) = \sum_{n=0}^{\infty}\sum_{m=0}^{\infty}\eta_{mn}e^{\hat{i}m\theta}J_m(\lambda_{mn}r)e^{\hat{i}\omega t}, \tag{3.22}$$

where J_m denotes the m_{th} order Bessel function of the first kind and eigenvalues λ_{mn} follow from application of the free boundary conditions to the excitation-free system. Substituting the expansion Eq. (3.22) into (3.18), multiplying both sides by $J_k(\lambda_{kl}r)e^{-\hat{i}k\theta}$ and integrating over the area yields,

$$-\omega^2\eta_{mn} + \omega_{mn}^2\eta_{mn} - \tilde{\theta}_{mn}V_0 + 2\hat{i}\zeta_{mn}\omega\omega_{mn} = f_{mn}, \tag{3.23}$$

where ω_{mn} is the undamped natural frequency related to eigenvalue λ_{mn},

$$\omega_{mn} = \lambda_{mn}^2 \sqrt{\frac{BI}{2\rho_p h_p}}, \tag{3.24}$$

and external forcing is represented similar to the displacement such that

$$f_{mn} = \frac{1}{N_n^{(m)}} \int_0^{2\pi} \int_0^{r_0} \tilde{f}(r,\theta) J_m(\lambda_{mn} r) e^{-\hat{i}m\theta}\, r dr\, d\theta, \tag{3.25}$$

has been used in arriving at Eq. (3.23). Coefficients $N_n^{(m)}$ result from boundary condition-specific orthogonality conditions [**?**],

$$\int_0^{r_0} \int_0^{2\pi} J_m(\lambda_{mn} r) e^{\hat{i}m\theta} J_k(\lambda_{kl} r) e^{-\hat{i}k\theta}\, r dr\, d\theta =$$

$$\begin{cases} 2\pi N_n^{(m)} \equiv 2\pi \frac{r_0^2}{2}(1 - \frac{m^2}{(\lambda_{mn} r_0)^2}) J_m^2(\lambda_{mn} r_0) & \text{if } k = m, l = n \\ 0 & otherwise \end{cases}. \tag{3.26}$$

Finally, the coupling term $\tilde{\theta}_{mn}$ arises from $P(r,\theta)$ and is given by,

$$\tilde{\theta}_{mn} = \frac{\hat{\theta}}{N_n^{(m)}} \int_0^{2\pi} \int_0^{r_0} P(r,\theta) J_m(\lambda_{mn} r) e^{-\hat{i}m\theta} r dr d\theta =$$

$$\begin{cases} \frac{1}{N_n^{(m)}} \hat{\theta} r_0 \frac{\partial J_m(\lambda_{mn} r)}{\partial r}\Big|_{r=r_0} & \text{if } m = 0 \\ 0 & otherwise \end{cases}, \tag{3.27}$$

which implies that the voltage of the harvester is only a function of r_0. It then follows from Eq. (3.23) that the desired coefficients are

$$\eta_{mn} = \frac{f_{mn} + \tilde{\theta}_{mn} V_0}{\omega_{mn}^2 - \omega^2 + 2\hat{i}\zeta_{mn}\omega\omega_{mn}}. \tag{3.28}$$

Following the circular plate modal approach [51, 52], the displacement of the circular disk is given by:

$$\phi_P(r,\theta) = \sum_{n=0}^{\infty}\sum_{m=0}^{\infty} \eta_{mn} e^{\hat{i}m\theta} J_m(\lambda_{mn} r), \tag{3.29}$$

where λ_{mn} denotes the eigenvalues for free edge boundary conditions and J_m denotes the m_{th}-order Bessel functions of the first kind. For a piezoelectric circular disk, η_{mn} are found to be,

$$\eta_{mn} = \frac{-f_{mn} + \tilde{\theta}_{mn} V_0}{\omega_{mn}^2 - \omega^2}, \tag{3.30}$$

where V_0 denotes the peak voltage (i.e., harvester voltage is given by $v(t) = V_0 e^{\hat{i}\omega t}$). Note that since forces $-f(r,\theta)$ are considered to act on the disk, a minus sign appears in front of f_{mn} in Eq. (3.30), which is absent from Eq. (3.28). Finally, note that $\tilde{\theta}_{mn}$ is non-zero for $m = 0$ only. This implies that $\tilde{\theta}_{mn}$ is solely a function of r.

The peak voltage V_0 requires final consideration before returning to the adjoining condition. The integral form of Gauss's equation provides an electromechanical

coupling equation which relates the harvester's displacement to its voltage,

$$\frac{d}{dt}\int_A \mathbf{D}\cdot\mathbf{n}dA = \frac{v(t)}{R_l}, \tag{3.31}$$

where $\mathbf{n}$ denotes the unit vector outward from electrode surface, $\mathbf{D}$ the electric displacement vector, R_l the resistance of the electrical circuit, and A the electrode's surface area over which the integral is performed over. The inner product between the unit vector $\mathbf{n}$ and the electric displacement $\mathbf{D}$ vector yields electric displacement component D_3. Substituting the disk's displacement field into the above equation, and following a standard evaluation procedure provided in [53] for a rectangular piezoelectric plate (herein the cylindrical-form of the operators are required) yields,

$$\hat{i}\omega C_p V_0 + \frac{V_0}{R_l} + \sum_{m=0}^{\infty}\sum_{n=0}^{\infty}\eta_{mn}\hat{\theta}_{mn}\hat{i}\omega = 0, \tag{3.32}$$

where $C_p = (\pi r_p^2 \bar{\varepsilon}_{33}^S)/h_p$ is the equivalent capacitance of the electrical circuit and $\bar{\varepsilon}_{33}^S$ denotes a permittivity component. Eqs. (3.29) and (3.32) then represent coupled equations for the disk displacement and voltage.

With the displacement fields and electric circuit completely specified, attention can return to the adjoining equation to eliminate interaction forces. Substituting Eqs. (3.5)-(3.6) and (3.29) into (3.3) yields an updated condition,

$$\frac{F_0}{8BIk_B^2\hat{i}}\Big(H_0^{(2)}(k_B\rho_1) - H_0^{(2)}(-\hat{i}k_B\rho_1)\Big)\Big|_{r<r_0} +$$

$$\frac{1}{8BIk_B^2\hat{i}}\Big(\int_0^{2\pi}\int_0^{r_0} f(r^*,\alpha)\Pi(k_B,\rho_0)\,r^*dr^*\,d\alpha\Big)\Big|_{r<r_0} =$$

$$\sum_{n=0}^{\infty}\sum_{m=0}^{\infty}\Big(\frac{-f_{mn}+\tilde{\theta}_{mn}V_0}{\omega_{mn}^2-\omega^2}\Big)e^{\hat{i}m\theta}J_m(\lambda_{mn}r)\Big|_{r<r_0}. \tag{3.33}$$

The first term on the left hand side of Eq. (3.33) is then converted from its Hankel form,

$$\frac{F_0}{8BIk_B^2\hat{i}}[H_0^{(2)}(k_B\rho_1)-H_0^{(2)}(-\hat{i}k_B\rho_1)]=\sum_{n=0}^{\infty}\sum_{m=0}^{\infty}E_{mn}e^{\hat{i}m\theta}J_m(\lambda_{mn}r), \tag{3.34}$$

where

$$E_{mn}=\frac{F_0}{16\hat{i}\pi BIk_B^2N_n^{(m)}}\int_0^{2\pi}\int_0^{r_0}\Big[H_0^{(2)}(k_B\rho_1)-H_0^{(2)}(-\hat{i}k_B\rho_1)\Big]e^{-\hat{i}m\theta}J_m(\lambda_{mn}r)r\,dr\,d\theta \tag{3.35}$$

are easily computed and

$$N_n^{(m)}=\frac{r_0^2}{2}(1-\frac{m^2}{(\lambda_{mn}r_0)^2})J_m^2(\lambda_{mn}r_0) \tag{3.36}$$

results from orthogonality relationships. Similarly, the second term on the left hand side of Eq. (3.33) is expressed as,

$$\frac{1}{8BIk_B^2\hat{i}}\Big(\int_0^{2\pi}\int_0^{r_0} f(r^*,\alpha)\Pi(k_B,\rho_0)\,r^*dr^*\,d\alpha\Big)=\sum_{n=0}^{\infty}\sum_{m=0}^{\infty}X_{mn}e^{\hat{i}m\theta}J_m(\lambda_{mn}r), \tag{3.37}$$

where

$$X_{mn} = \frac{1}{16\hat{i}\pi BIk_B^2 N_n^{(m)}} \int_0^{2\pi}\int_0^{r_0} \Big[\int_0^{2\pi}\int_0^{r_0} \sum_{l=0}^{\infty}\sum_{k=0}^{\infty} f_{kl} \cdot e^{\hat{i}k\alpha} J_k(\lambda_{kl} r^*)\Pi(k_B,\rho_0) r^*\, dr^*\, d\alpha \Big] e^{-\hat{i}m\theta} J_m(\lambda_{mn} r) r\, dr\, d\theta, \tag{3.38}$$

and $f(r^*, \alpha)$ is replaced by its Hankel form using Eqs. (3.25).

Placing Eqs. (3.35)-(3.38) into Eq. (3.33), simplifying, and arranging the coefficients of Bessel functions yields,

$$\sum_{n=0}^{\infty}\sum_{m=0}^{\infty} \Big(E_{mn} e^{\hat{i}m\theta} J_m(\lambda_{mn} r) + X_{mn} e^{\hat{i}m\theta} J_m(\lambda_{mn} r) \Big)\Big|_{r<r_0} =$$

$$\sum_{n=0}^{\infty}\sum_{m=0}^{\infty} \Big(\frac{-f_{mn} + \tilde{\theta}_{mn} V_0}{\omega_{mn}^2 - \omega^2} \Big) e^{\hat{i}m\theta} J_m(\lambda_{mn} r)\Big|_{r<r_0}. \tag{3.39}$$

Equating coefficients of $e^{\hat{i}m\theta} J_m(\lambda_{mn} r)$ then yields,

$$\begin{cases} E_{0n} + X_{0n} = \frac{-f_{0n} + \tilde{\theta}_{0n} V_0}{\omega_{0n}^2 - \omega^2} & \text{if } m = 0 \\ E_{mn} + X_{mn} = \frac{-f_{mn}}{\omega_{mn}^2 - \omega^2} & otherwise \end{cases}. \tag{3.40}$$

The peak voltage V_0 still requires incorporation into the expressions. From the circuit equation, Eq. (3.32),

$$V_0 = -\hat{i}\omega \frac{\sum_{n=0}^{\infty}\sum_{m=0}^{\infty} \eta_{mn}\tilde{\theta}_{mn}}{\hat{i}\omega C_p + \frac{1}{R_l}}, \tag{3.41}$$

which when followed by substitution of Eq. (3.30) yields,

$$V_0 = \hat{i}\omega \frac{\sum_{n=0}^{\infty}\sum_{m=0}^{\infty}\frac{f_{mn}\tilde{\theta}_{mn}}{\omega_{mn}^2-\omega^2}}{\hat{i}\omega C_p + \frac{1}{R_l} + \sum_{n=0}^{\infty}\sum_{m=0}^{\infty}\frac{\hat{i}\omega\tilde{\theta}_{mn}^2}{\omega_{mn}^2-\omega^2}}. \tag{3.42}$$

The result of Eqs. (3.40) and (3.42) is now an implicit system of equations containing the desired f_{mn}, which can be posed as

$$[\mathscr{L}]\mathscr{F} = \mathscr{E} \tag{3.43}$$

where

$$\mathscr{F} = [f_{00}\ \ f_{01}\ \ f_{02} \ldots f_{10}\ \ f_{11} \ldots f_{MN}]^T, \tag{3.44}$$

$$\mathscr{E} = [E_{00}\ \ E_{01}\ \ E_{02} \ldots E_{10}\ \ E_{11} \ldots E_{MN}]^T, \tag{3.45}$$

and $\mathscr{L}$ is a coefficient matrix whose elements follow from Eqs. (3.40) and (3.42), and where M and N denote the series' truncation sizes. The final step in quantifying the interaction forces is the inversion of $[\mathscr{L}]$,

$$\mathscr{F} = [\mathscr{L}]^{-1}\mathscr{E}. \tag{3.46}$$

3.3 Results

This section generates analytically-predicted steady-state results for the system's response quantities (displacements and voltages), and compares these quantities to those obtained using both numerical and experimental means. The frequency response of the combined harvester/plate system is also studied, and an analysis of the electrical resistance needed to optimize harvested power is presented.

3.3.1 Numerical model and validation

As a first means to validating the analytical model presented in Sec. 3.2, transient numerical simulations are performed and results compared to those generated using the analytical model. The numerical model incorporates many of the same assumptions as the analytical model and allows for precise specification of material/system parameters and loading, thus comparisons with the analytical approach are expected to show close agreement. In contrast, experimentally-obtained results (appearing in Sec. 3.3.3) are expected to show larger errors due to uncertainties associated with material parameters such as stiffness and density, non-ideal source specification due to the use of a finite-sized piezoelectric device, unintended reflections from imperfections and boundaries, etc.

Numerical results are computed using the commercial finite element package COMSOL. A model is assembled using COMSOL's time domain solver together with the *Piezoelectric Devices* and *Solid Mechanics* interfaces in the *Structural Mechanics Module*, and the *Electrical Circuit* interface in the *AC/DC Module*. As shown in Fig-

ure 3.3a, the numerical model has a symmetry axis that can be exploited to decrease the computational cost. The thickness of the aluminum host plate and piezoelectric disk are modeled as $h_s = 1mm$ and $h_p = 0.9mm$, respectively. In addition, the radius of the piezoelectric disk is chosen to be $r_0 = 15mm$. Similar to previous studies, the forcing frequency is specified to be $f = 50kHz$. Steady-state behavior is achieved using a simulation extent of $t = [0, 1ms]$. The modeled substrate extent is chosen to be large enough (150 $\times$ the diameter of the piezoelectric disk) to prevent propagating waves from returning to measurement points during the simulation. In addition, an infinite element domain has been added to the model as a means to achieve a non-reflecting boundary condition. Representative points are selected in the domain to record simulated displacements for comparison to those predicted by the analytic model, as depicted in Figure 3.3b. Five points are chosen on the plate domain, of which three lie on the boundary of the piezoelectric patch. Point 1 locates the harmonic point source. The position of each point is tabulated in Table 3.1, where the origin is assumed to be at the center of the piezoelectric disk. Figure 3.4 depicts the mesh employed, which consists of three-dimensional tetrahedral solid elements. Due to accuracy and efficiency considerations, the mesh density is high near the piezoelectric disk and becomes increasingly more coarse as the outer edges are approached.

Figure 3.5 presents the numerically-computed time response of the chosen points not on the boundary of the piezoelectric disk. Based on inspection of this figure, the time for each point to reach steady state is nearly the same and approximately $400\mu s$. In addition, the figure suggests that points closer to the excitation source have more

Table 3.1: *Coordinates of the chosen points on the plate and circular piezoelectric disk*

point	1	2	3	4	5	6	7	8
x	0	$3r_0$	$2r_0$	$3r_0$	0	0	r_0	0
y	$20r_0$	$3r_0$	0	$-6r_0$	$-10r_0$	r_0	0	$-r_0$

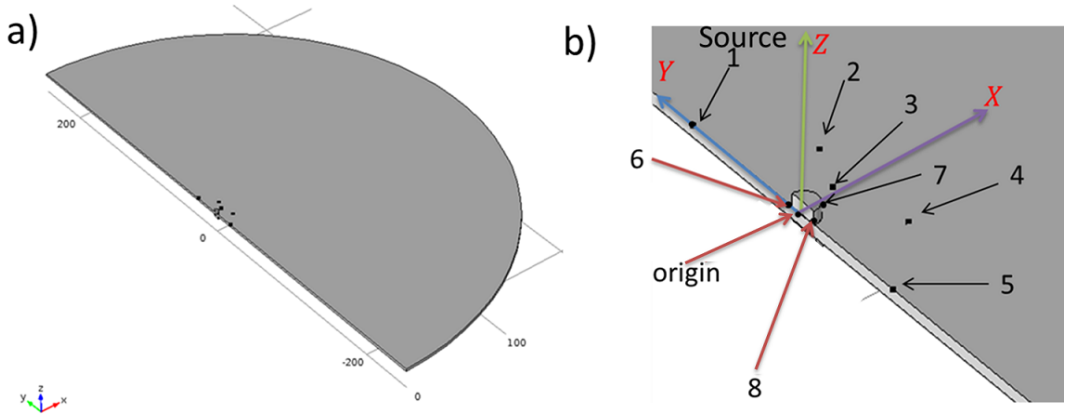

Figure 3.3: *a) Schematic of the COMSOL model including circular harvester b) Visual location of measurement points on the plate model.*

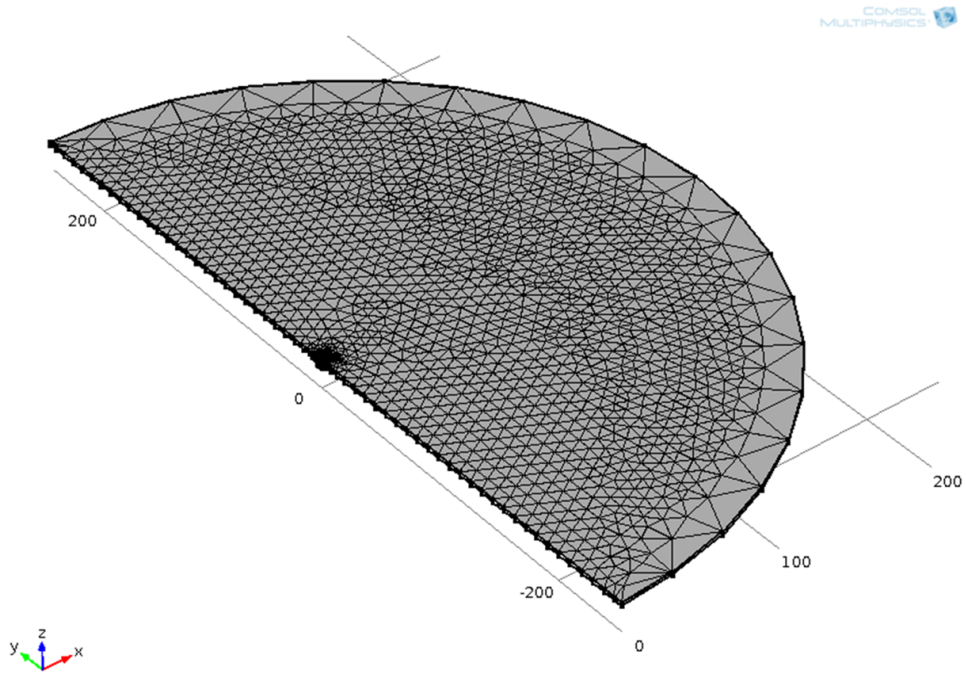

Figure 3.4: ***Tetrahedral mesh employed in numerical studies.***

displacement amplitude than those further away, as expected. Since only the steady-state portion of the response can be compared to the analytical results, the transient response is removed from results presented in Figure 3.6. There, a comparison is made between the displacements predicted by the analytical and numerical models. For all analytical results presented herein, based on the results of a convergence study (not provided), the series' truncation values are chosen to be $M = 10$ and $N = 6$. Note that all response quantities compared in Figure 6 exhibit very good agreement, although a small phase difference is evident for points 4 and 5. Similarly, for points 6 – 8 lying on the boundary of the piezoelectric disk, Figure 3.7 documents good agreement in displacement time histories, with phase errors on the order of that observed for points 4 and 5. Due to the location of points 4 and 5 (in the wake of the piezoelectric disk) and the similar phase error to points 6 – 8, this would suggest that

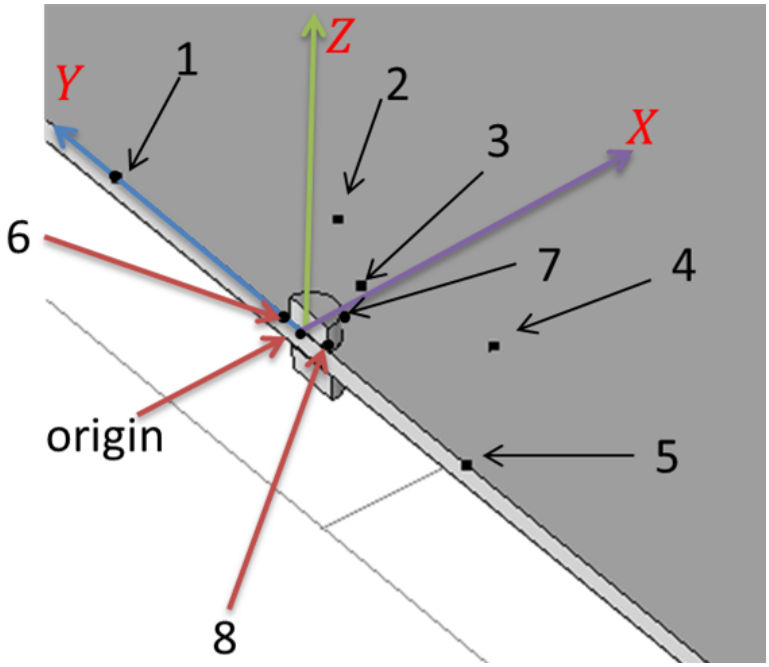

Figure 3.5: ***Numerically-computed temporal response of points a) 2, b) 3, c) 4, and d) 5 due to point force excitation.***

the phase error is in fact due to small modeling errors associated with the disk-plate interface. There, the numerical model strictly enforces displacement continuity, while the analytical model satisfies the condition weakly as the series truncation approaches infinity.

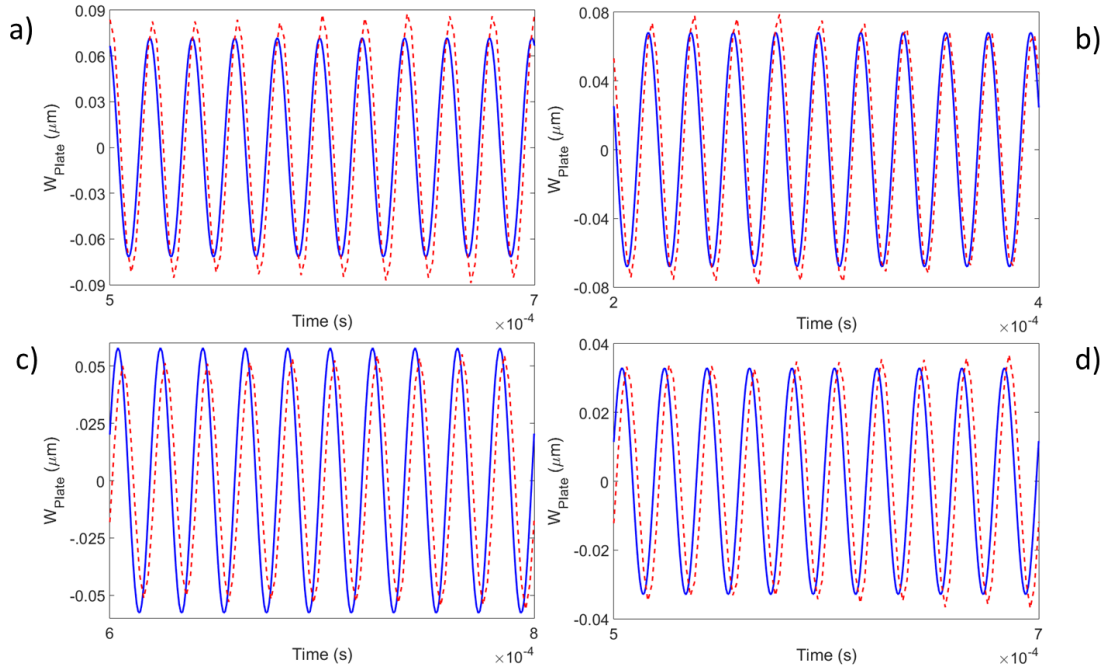

Figure 3.6: ***Steady state response of points a) 2, b) 3, c) 4, and d) 5 due to point force excitation. Solid lines depict analytical results; dashed lines depict numercal results.***

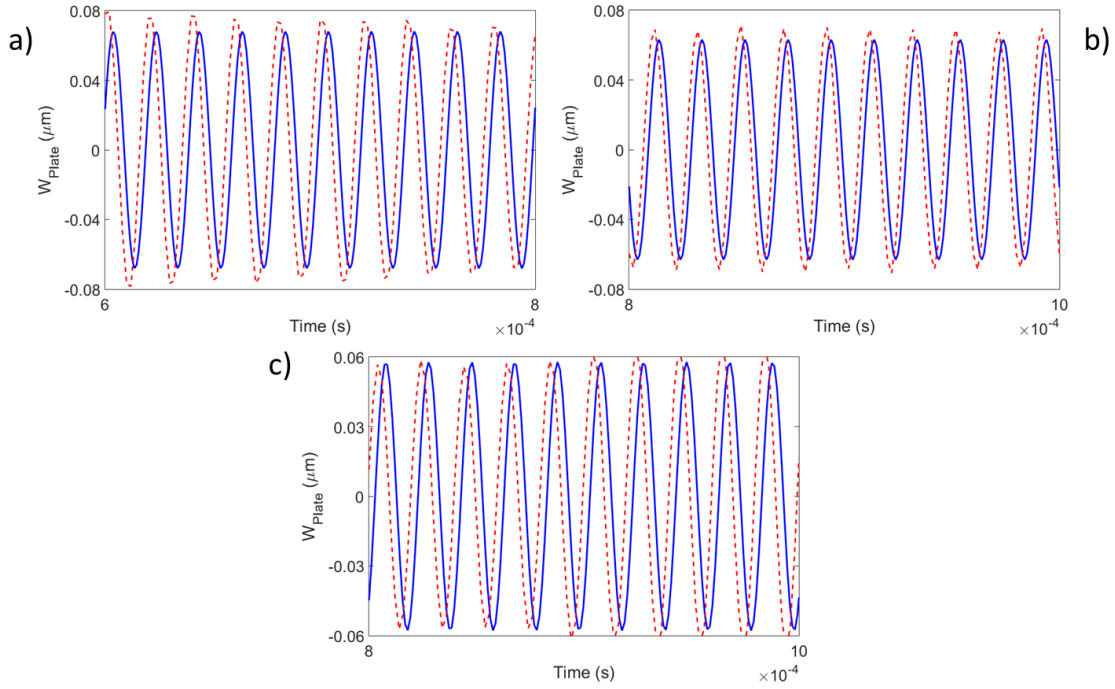

Figure 3.7: ***Steady-state response of points a) 6, b) 7, and c) 8 due to point force excitation. Solid lines depict analytical results; dashed lines depict numerical results.***

3.3.2 Frequency response

This section computes the frequency response of the system using both the analytical and numerical models. In comparison to cases without a substrate (i.e., solely a piezoelectric circular plate), the coupled system has a much larger effective mass, and thus decreases in the natural frequencies are expected. To explore this effect, system response is computed with and without the substrate. For the case without a substrate, the bottom-center of the piezoelectric disk is chosen for source excitation.

For both cases, Figure 3.8 provides the computed displacement of point 7 on the boundary of the piezoelectric disk as a function of frequency, while Figure 3.9 provides the accompanying short-circuit voltage. The amplitude of the peak responses have been normalized such that both (i.e., with and without substrate) are approximately equal. As observed in the figures, the analytical approach yields a fundamental natural frequency of the coupled system equal to approximately 1.92 Hz, and approximately 9125 Hz for the case without substrate, in agreement with the expected trend. Inspection of Figures 3.8a and 3.9a shows a small difference between the fundamental natural frequency computed using the analytical and numerical models for the system. This difference is most likely due to the finite size of the COMSOL model, which results in a lower mass and thus a higher frequency. Note that the case with a substrate does *not* have a natural frequency of zero, as might be expected from an unrestrained system. The presence of a non-zero fundamental frequency is due to the concept of phase closure by which a wave propagating through the disk reflects at the far edge, and then reflects again when it reaches the incident edge, establishing a

wavelength and phase change associated with resonance behavior.

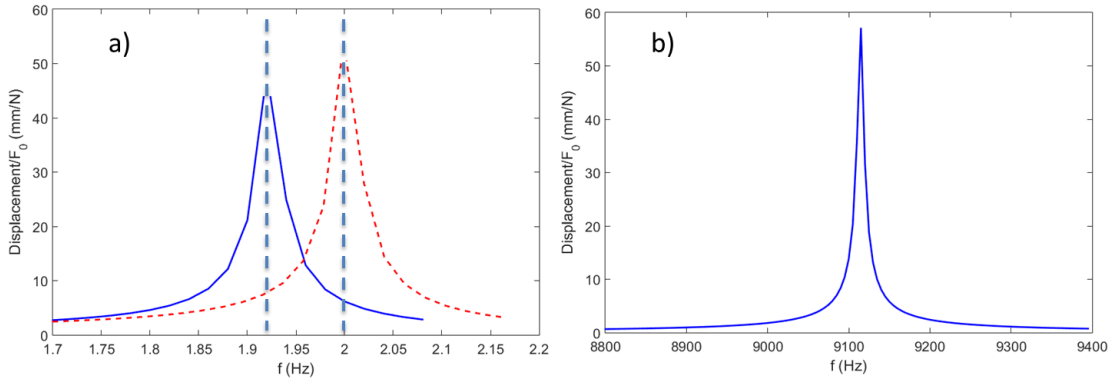

Figure 3.8: ***Frequency response (displacement) of the considered system due to point force excitation for a) case with an infinite host substrate and b) case without a host substrate. Solid lines depict analytical results; dashed lines depict numerical results.***

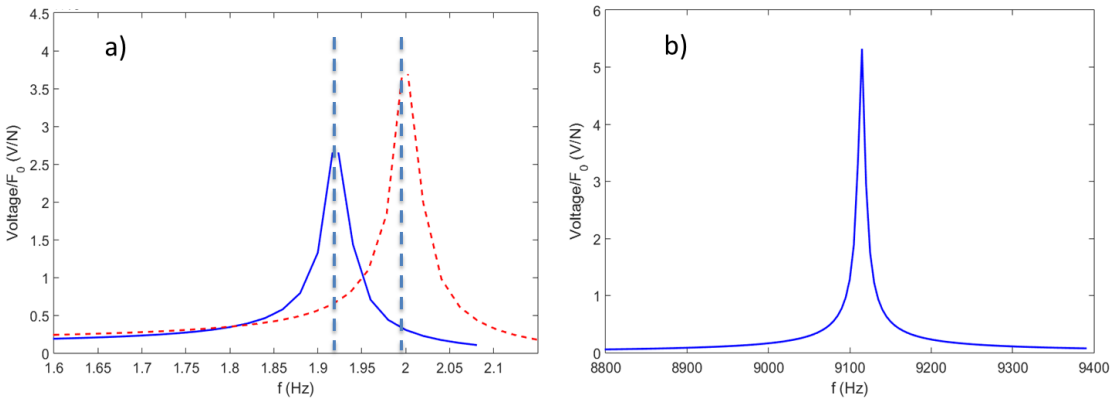

Figure 3.9: ***Frequency response (short-circuit voltage) of the considered system due to point force excitation for a) case with an infinite host substrate and b) case without a host substrate. Solid lines depict analytical results; dashed lines depict numerical results.***

3.3.3 Experimental apparatus and validation

This section describes a set of experiments aimed at further validation of the presented analytical modeling approach. The experiments are limited to measuring the surface displacement field (due to use of a scanning laser vibrometer) and harvester

voltage. To excite the system, an epoxy-bonded piezoelectric transducer (Steiner Martins SMD50T25F15R, 3M DP270 Epoxy Adhesive) produces plate displacements in response to a generated voltage profile. A second transducer of the same type is used for the harvester. The aluminum host plate and piezoelectric disks have thicknesses $h_s = 1mm$ and $h_p = 0.9mm$, respectively. The disks have a radius of $15mm$ and an effective capacitance of $C_p = 3.5nF$. As shown in Figure 3.10, the first transducer is excited by 40 cycles of $f = 50kHz$ voltage using a function generator (Agilent 33220A) coupled to a voltage amplifier (B&K 1040L). A Polytec PSV-400 scanning laser Doppler vibrometer measures the resulting wave field, over a $16cm \times 16cm$ square area, using the backside of the plate and a 250×250 grid resolution. The distance between the excitation and harvester centers is $30cm$. Wave-field images and RMS distributions are obtained by recording the out-of-plane plate response covering the piezoelectric harvester and the square subdomain. Proper triggering of the laser measurements allows the reconstruction of the out-of-plane velocity field, while time integration of the recorded responses yields RMS distributions.

Figure 3.11 presents the plate displacement contours obtained experimentally using an attached 10 Ω (short circuit) resistor connected to the piezoelectric disk. Clearly evident in this figure is the location of the piezoelectric harvester, which appears as diminished displacement response, demonstrating harvester effectiveness. Figure 3.12 presents experimentally-obtained transient and steady-state results for the same plate points labeled in Figure 3.3b. Also presented in this figure are analytical results, which are only valid in the steady-state region. For comparison to the analytical model, the equivalent value of the point force needed is found by ap-

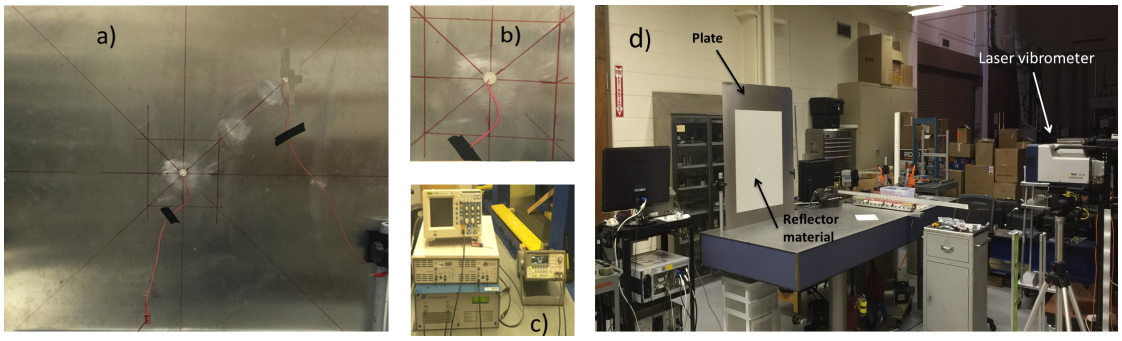

Figure 3.10: ***Experimental setup including a) an aluminum plate hosting piezoelectric transducers for exciting and harvesting waves, b) scaled picture of a circular piezoelectric disk, c) function generator and amplifier for generating requisite voltage profiles, and d) overall setup showing mounted plate (left) and laser vibrometer (right) used to measure transverse plate velocities on the plate's backside, which is covered in reflective material.***

plying the source voltage and waveform to the piezoelectric disk attached to a host plate without a harvester. Then, by measuring the displacement of a point $10cm$ away from the transducer, excitation force F_0 is inferred using Eq. (3.5). As can be observed in Figure 3.12, good agreement between both sets of results is documented in the steady-state, except at the outer edge of the piezoelectric disk (i.e., point 8). This discrepancy is likely due to the inherent discontinuity in the physical system at this point and the subsequent potential for separation of the disk from the plate at the outer edges - note that the response of the experiment is indeed less than that predicted analytically.

3.3.4 Resistance optimization

The circuit resistance corresponding to maximum harvested power is explored next. The average power produced by the system is given by $P = \frac{V_0^2}{2R_l}$. Taking the derivative

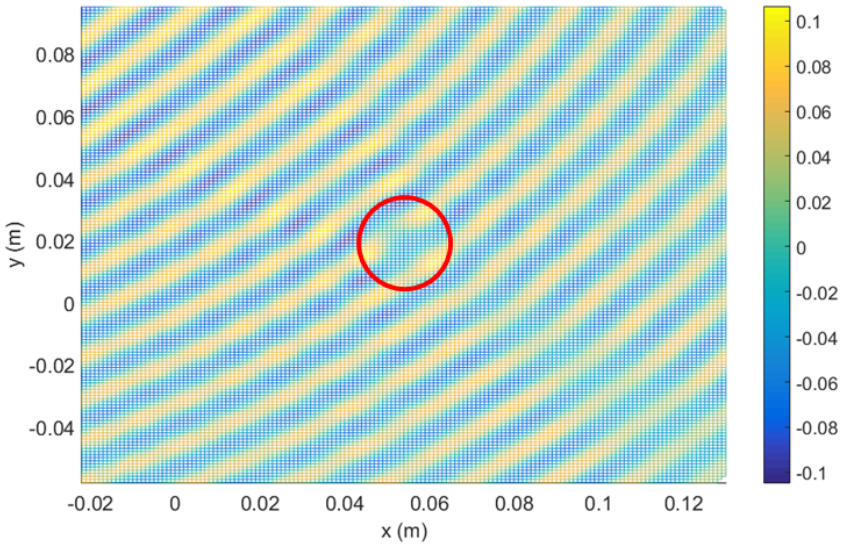

Figure 3.11: ***Experimentally-obtained displacement field contours for*** $\boldsymbol{f}$**=**$50kHz$**,** $\boldsymbol{R}$**=**10Ω**.**

of the average power with respect to the resistance load, $\frac{dP}{dR_l}$, setting to zero,

$$\frac{1}{2}\frac{2V_0\frac{dV_0}{dR_l}-V_0^2}{R_l^2}=0, \tag{3.47}$$

and then using Eq. (3.42) yields,

$$\frac{2}{R_l}\frac{R_l^2\left[\sum_{n=0}^{\infty}\sum_{m=0}^{\infty}\frac{\frac{df_{mn}}{dR_l}\tilde{\theta}_{mn}}{\omega_{mn}^2-\omega^2}\right]\left[\hat{i}\omega C_p+\frac{1}{R_l}+\sum_{n=0}^{\infty}\sum_{m=0}^{\infty}\frac{\hat{i}\omega\tilde{\theta}_{mn}^2}{\omega_{mn}^2-\omega^2}\right]+\sum_{n=0}^{\infty}\sum_{m=0}^{\infty}\frac{f_{mn}\tilde{\theta}_{mn}}{\omega_{mn}^2-\omega^2}}{\hat{i}\omega C_p+\frac{1}{R_l}+\sum_{n=0}^{\infty}\sum_{m=0}^{\infty}\frac{\hat{i}\omega\tilde{\theta}_{mn}^2}{\omega_{mn}^2-\omega^2}}$$

$$=\sum_{n=0}^{\infty}\sum_{m=0}^{\infty}\frac{f_{mn}\tilde{\theta}_{mn}}{\omega_{mn}^2-\omega^2}. \tag{3.48}$$

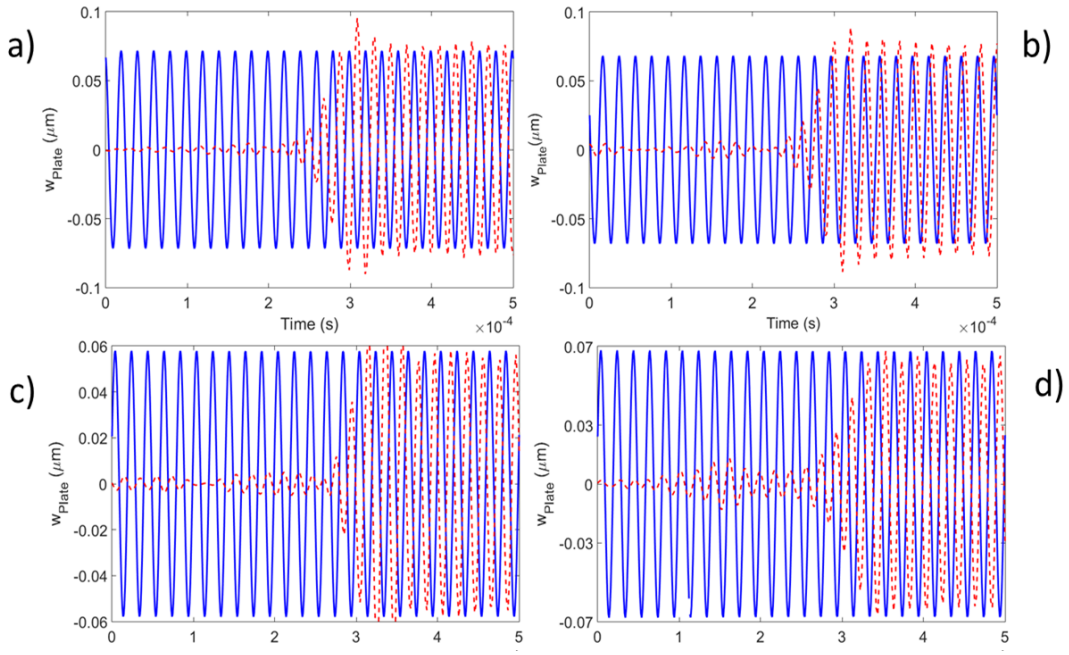

Figure 3.12: ***Steady state response of points a) 2, b) 3, c) 4, d) 6, e) 7, and f) 8. Solid lines depict analytical results; dashed lines depict experimental results.***

Note that if operating frequency is near one of the piezoelectric disk's natural frequencies, ω_r, the optimization condition can be greatly simplified to,

$$\frac{2R_l\left[\frac{\frac{df_r}{dR_l}\tilde{\theta}_r}{\omega_r^2-\omega^2}\right]\left[\hat{i}\omega C_p+\frac{1}{R_l}+\frac{\hat{i}\omega\tilde{\theta}_r^2}{\omega_r^2-\omega^2}\right]+\frac{2f_r\tilde{\theta}_r}{\omega_r^2-\omega^2}}{\hat{i}\omega C_p+\frac{1}{R_l}+\frac{\hat{i}\omega\tilde{\theta}_r^2}{\omega_r^2-\omega^2}}=\frac{f_r\tilde{\theta}_r}{\omega_r^2-\omega^2}, \tag{3.49}$$

where quantities with a subscript r are those evaluated using the r_{th} natural frequency. Since the 50 kHz excitation employed herein falls between two natural frequencies, solution of Eq. 3.47 must be employed to find optimum resistance R_l. Doing so results in one real and one complex value for the resistance. The real value is the only physically-realizable one and is found to be approximately 1000 Ω.

Figure 3.13 presents the analytically-predicted and experimentally-measured peak power as a function of load resistance R_l at the excitation frequency of $50kHz$. A

resistance substituter (IET Labs model RS-200) is used to generate a full sweep of resistance from 10 Ω (close to short-circuit condition) to 10 $M\Omega$ (close to open-circuit condition). Using a National Instruments data acquisition system (Model cDAQ-9178), voltage across the resistor is measured and output power is calculated accordingly. The maximum of the peak power for the case studied has a resistance near 1000 Ω, which is closer to the short-circuit condition rather than the open-circuit condition, and matches closely with the predicted optimum resistance value. This optimal resistance produces approximately 4 mW of electric power. Note that the figure documents close agreement between the predicted and experimental peak power over a large range of load resistances.

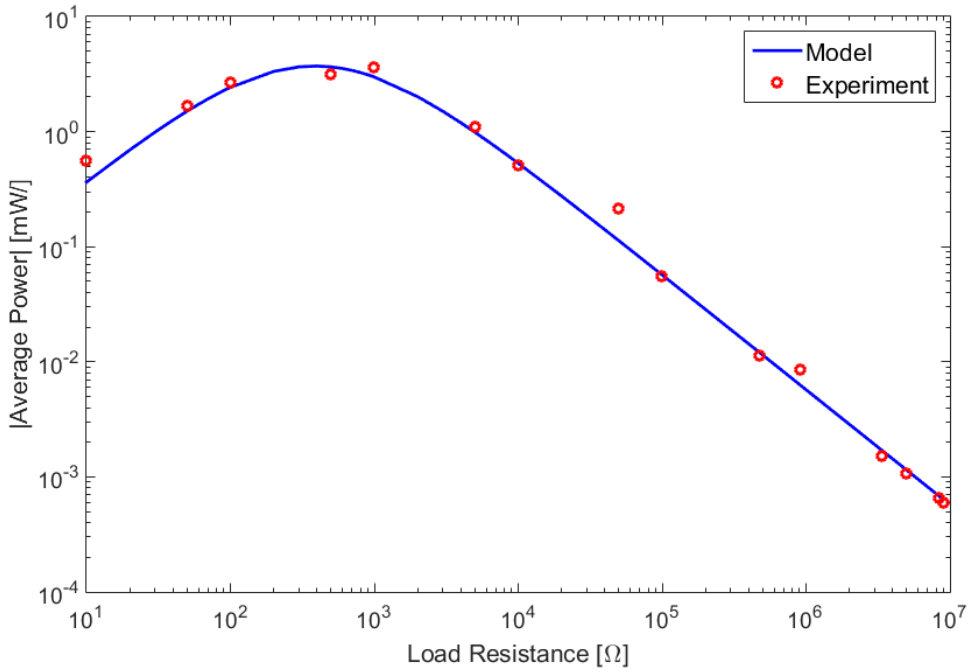

Figure 3.13: ***Peak power generated by the piezoelectric harvester for varying values of load resistance.***

Chapter 4

Multiple Scattering of Acoustoelastic Waves Energy Harvesting

4.1 Overview

This chapter presents an electromechanically-coupled, multiple scattering formulation in which elastic scatterers (e.g., cylindrical inclusions and voids) are coupled with the piezoelectric scatterer considered in the previous chapter. This enables high-fidelity, coupled electromechanical modeling of MEH concepts to be explored for the first time. Following development, the formulation is applied to determining optimal arrangements of scatterers, nominally in a semi-elliptical path, which maximize electrical power harvested. This is done, in part, by diminishing side lobes resulting from ellipse truncation observed in past studies [39]. Optimization results exhibit minimized side lobes and harvester power nearly ten times that of the non-optimized case. Finally, an experimental study is presented which confirms many of the model predictions.

Multiple metamaterial energy harvesting (MEH) approaches were introduced by Carrara *et al.* [39, 40], consisting of metamaterial arrangements with (i) an introduced defect resonator, (ii) a funnel-shaped waveguide, and (iii) a lens-shaped mirror. Each concept included a piezoelectric transducer for harvesting wave energy. In all these studies, the harvesting element (i.e., piezoelectric disk) was not part of the analytical

or numerical model and detailed predictions of harvesting performance were not made. Among the MEH concepts introduced to date, the elliptical MEH mirror appears to hold the most promise since a source at one focal point of an ellipse can be perfectly focused at the other focal point. However, in practice, only a small portion of the ellipse is used, which while focusing much of the incident energy, results in spurious effects such as side lobes and other unfocused artifacts. As a follow-on, a Fourier transform-based harvester design was introduced to enhance the energy extracted from the finite mirror [41], which works by covering a larger space using patterned electrode arrangements to harvest from the focal point and side lobes. Although effective, it requires a complex transducer shape and specialized fabrication.

4.2 System Model

4.2.1 Overview of elastodynamic multiple scattering problem

The governing equation for wave propagation in a thin, infinite plate is given as

$$D \bigtriangledown^4 w + \rho h \frac{\partial^2 w}{\partial t^2} = f(r, \theta, t) \tag{4.1}$$

where w denotes the displacement of the plate, $f(r, \theta, t)$ the distributed external forces, h and ρ the thickness and mass density, respectively, and D denotes the plate's flexural stiffness given as $\frac{Eh^3}{12(1-\nu^2)}$ where E represents Young's modulus and ν Poission's ratio. All incident and scattered waves considered herein satisfy Eq. 4.1.

Further, scatterers are considered to be singular points within the domain which transform incident waves into scattered waves.

Figure 4.1 depicts a representative geometry for multiple-scattering occurring in the infinite host plate. A total of N scatterers are embedded in the host plate. As this figure illustrates, scatterer i with radius a_i is located at (d_{s_i}, θ_{s_i}) with respect to a global coordinate system. A local coordinate system (r_i, θ_i), attached to the center (X_i, Y_i) of the scatterer, is also used to locate any point on the plate. This latter coordinate system is the most natural one for formulating a transformation matrix relating incident and scattered wave coefficients.

In the multiple scattering context, the initial wavefield and all scattered waves, except that due to self-scattering, are incident on scatterer i and then further scattered. This statement can be made for each scatterer j such that the total wavefield must be consistent. To aid in forming a consistent mathematical statement, a linear transformation between the scattered and the incident waves for each scatterer is introduced using the single scatterer T-matrix. The individual T-matrices are obtained by the conventional separation of variables approach and the matching of boundary conditions. Before applying the T-matrix transformation, all waves must be expressed in scatterer i's local coordinate system. Once the T-matrix for an inclusion type is obtained, it can be applied in the multiple scattering process.

Cai *et al.* formulated the multiple scattering problem on thin plates [50] employed herein, to include the requisite T-matrices for various inclusions such as rigid, void and elastic cylindrical. For circular inclusions of radius a_j subject to an incident wave,

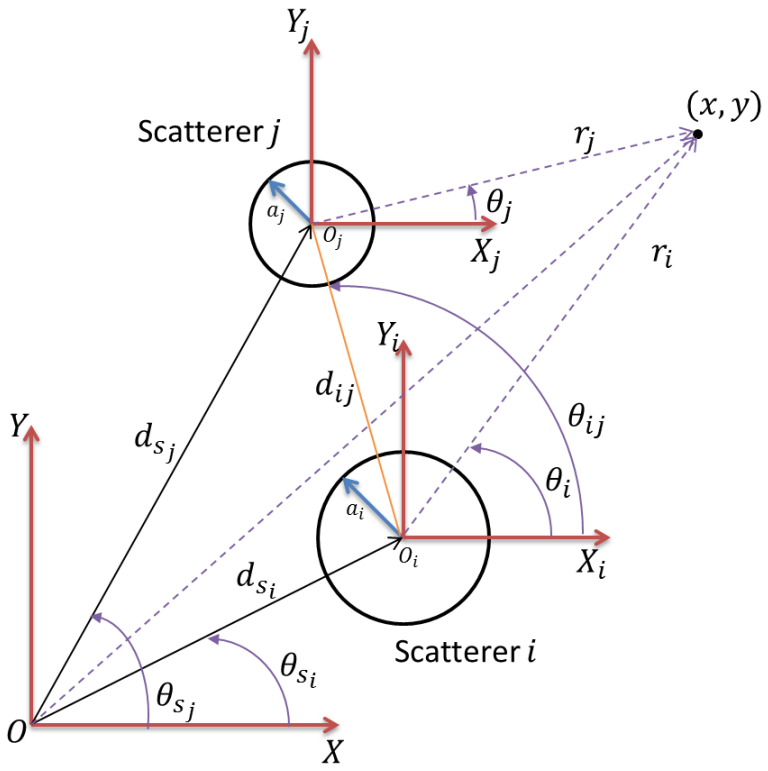

Figure 4.1: ***Schematic of multiple-scattering problem.***

the incident wave is expressible as

$$w^{inc} = \Big(\{\mathbf{A}^p\}^T\{\mathbf{J}(r,\theta)\} + \{\mathbf{A}^e\}^T\{\mathbf{I}(r,\theta)\}\Big)e^{\hat{i}\omega t} \tag{4.2}$$

and the wave scattered by an individual scatterer is expressible as,

$$w_i^{scr} = \Big(\{\mathbf{B}_i^p\}^T\{\mathbf{H}(r_i,\theta_i)\} + \{\mathbf{B}_i^e\}^T\{\mathbf{K}(r_i,\theta_i)\}\Big)e^{\hat{i}\omega t} \tag{4.3}$$

where $\{\Omega(r,\theta)\}_n = \Omega_n(kr)e^{\hat{i}n\theta}$, $k^2 = \omega\sqrt{\frac{\rho h}{D}}$ and ω is the excitation frequency. $\{\mathbf{A}^p\}$, $\{\mathbf{A}^e\}$ denote arrays holding the expansion (or wave) coefficients of the propagating and and evanescent incident waves, respectively. Similarly, $\{\mathbf{B}_i^p\}$, $\{\mathbf{B}_i^e\}$ denote arrays

containing expansion (or wave) coefficients for propagating and evanescent scattered waves, respectively. Finally, $\{\mathbf{J}(r,\theta)\}$, $\{\mathbf{I}(r,\theta)\}$, $\{\mathbf{H}(r,\theta)\}$ and $\{\mathbf{K}(r,\theta)\}$ represent arrays holding Bessel functions of the first kind, modified Bessel functions of the first kind, Hankel functions of the first kind and the modified Bessel functions of the second kind, respectively.

Following the approach detailed by Cai [50] for multiple scattering, the wave scattered by scatterer j is expressed in the coordinate system of scatterer i through rotation matrices,

$$w_j^{scr} = \Big(\{\mathbf{B}_j^p\}^T[\mathbf{R}_{ji}^p]\{\mathbf{J}(r_i,\theta_i)\} + \{\mathbf{B}_j^e\}^T[\mathbf{R}_{ji}^e]\{\mathbf{I}(r_i,\theta_i)\}\Big)e^{\hat{i}\omega t} \tag{4.4}$$

where the entries of the rotation matrices $[\mathbf{R}_{ij}^p]$ and $[\mathbf{R}_{ij}^e]$ at the n_{th} row and m_{th} column are given by,

$$[R_{ij}^p]_{nm} = e^{\hat{i}(n-m)\theta_{ij}} J_{n-m}(kd_{ij}) \tag{4.5}$$

$$[R_{ij}^e]_{nm} = (-1)^m e^{\hat{i}(n-m)\theta_{ij}} K_{n-m}(kd_{ij}) \tag{4.6}$$

such that (d_{ij},θ_{ij}) are the polar coordinates associated with O_j, the origin of scatter j, in i's local coordinate system. After all waves incident on scatterer i are expressed in i's coordinate system, i's T-matrix ($[\boldsymbol{\tau_i}]$) yields an expression relating the wave

coefficients at i to those at all other scatterers $j = 1, 2, ..., N$,

$$\{\mathbf{B}_i\} = [\boldsymbol{\tau}_i]\left(\{\mathbf{A}_i\} + \sum_{j=1, j\neq i}^{N} [\boldsymbol{\mathscr{R}}_{ji}]^T \{\mathbf{B}_j\}\right), \tag{4.7}$$

where N denotes the total number of scatterers,

$$\boldsymbol{\mathscr{R}}_{ji} = \begin{bmatrix} [\mathbf{R}^p_{ji}] & 0 \\ 0 & [\mathbf{R}^e_{ji}] \end{bmatrix}, \tag{4.8}$$

and $\{\mathbf{A}_i\} = \begin{Bmatrix} \{\mathbf{A}^p_i\} \\ \{\mathbf{A}^e_i\} \end{Bmatrix}$, $\{\mathbf{B}_i\} = \begin{Bmatrix} \{\mathbf{B}^p_i\} \\ \{\mathbf{B}^e_i\} \end{Bmatrix}$ denote the generalized expansion coefficients in scatterer i's local coordinate system. As indicated in Eq. (4.7), self-scattering does not contribute to $\{\mathbf{B}_i\}$.

Collecting all N instances of Eq. (4.7) results in the following relationship for the unknown coefficients of the scattered wave,

$$\{\boldsymbol{\mathscr{B}}\} = [\boldsymbol{\mathscr{L}}]\{\boldsymbol{\mathscr{A}}\} \tag{4.9}$$

where

$$\{\mathscr{B}\} = \begin{Bmatrix} \{\mathbf{B}_1\} \\ \{\mathbf{B}_2\} \\ . \\ . \\ . \\ \{\mathbf{B}_N\} \end{Bmatrix}, \quad \{\mathscr{A}\} = \begin{Bmatrix} [\boldsymbol{\tau}_1]\{\mathbf{A}_1\} \\ [\boldsymbol{\tau}_2]\{\mathbf{A}_2\} \\ . \\ . \\ . \\ [\boldsymbol{\tau}_N]\{\mathbf{A}_N\} \end{Bmatrix}, \tag{4.10}$$

and the elements of $[\mathscr{L}]$ contain rotation and transmission matrices. Note that the T-matrix entries are detailed in [50]for both rigid and void cylindrical inclusions.

4.2.2 Coupled electroacoustic multiple scattering problem

A model of an unbounded plate with a piezoelectric harvester and semi-elliptical shaped scatterers under harmonic point source excitation is developed next. A schematic of the system under consideration is shown in Figure 4.2 consisting of a circular piezoelectric disk with radius r_0 bonded to an infinite substrate layer. A global coordinate system (X, Y) is assigned to the center of the piezoelectric disk and polar coordinates (r, θ) are used in locating the orientation and response of the point source and plate displacements. A harmonic point excitation $F_0 e^{\hat{i}\omega t}$ at a distance (r_1, θ_1) from the defined origin generates incident waves - generalization to more complex loading can be realized through superposition of multiple point sources. Scatterers are placed on a semi-elliptical path with the major radius given by a and minor given by b. Later, these positions are assumed to vary. For a full ellipse, these scatterers

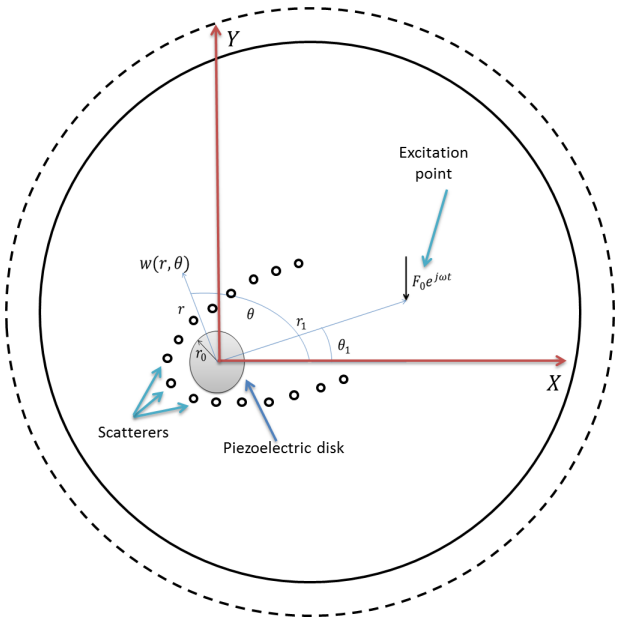

Figure 4.2: ***Schematic of a plate with bonded piezoelectric patch and scatterers under the excitation of harmonic force.***

focus energy originating at one focal point onto the other focal point. By placing a piezoelectric energy harvester close to one focal point, source energy originating from the other focal point can be converted to electrical power using an attached electrical circuit. Note that the harvester itself is a source of scattering, and thus its presence disrupts the ideal focusing behavior.

To predict the electromechanical response of the coupled system, two subsystems are introduced which exchange distributed interaction forces, $f(r,\theta)$. Since the piezoelectric disk is finite in extent, a modal approach is used to describe its response. Similar to that done in [54], the first subsystem consists of an infinite plate without a harvester, which experiences displacements due to external harmonic forces arising from the the interaction between the plate and the circular piezoelectric disk, and displacements due to interactions with the scatterers. The second subsystem consists of the piezoelectric disk in isolation and under the same interaction forces in an opposite

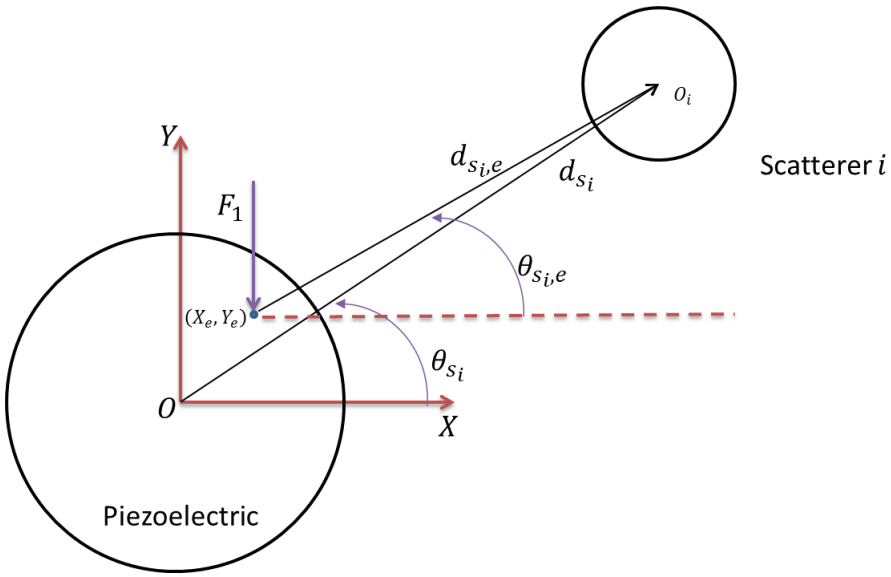

Figure 4.3: ***Equivalent excitation force, force location, and associated geometry for multiple scattering problem.***

sense, $-f(r,\theta)$. For the first subsystem, three different field quantities superimpose to form the response of the plate: plate displacements due to the harmonic force excitation w_F, the response to interaction forces w_f, and the reflected wavefield from the scatterers $\sum_{j=1}^{N} w_j^{scr}$. For the piezoelectric patch, w_P captures displacements due to interaction forces.

To incorporate the piezoelectric disk model into the multiple scattering formulation, the wavefield incident on the scatterers is treated as a combination of disturbances generated by the harmonic point source excitation and disturbances generated by the distributed forces associated with the piezoelectric patch,

$$w^{inc}(r,\theta,t) = w_F(r,\theta,t) + w_f(r,\theta,t) \tag{4.11}$$

As reviewed in Sec. 4.2.1, in the multiple-scattering context, the incident wavefield

must be expressed in the local coordinate system of each scatterer, which can be accomplished using coordinate transformations similar to Eqs. (4.5-4.6). Specifically, for the ith scatterer,

$$w_i^{inc}(r_i,\theta_i) = \Big(\{\mathbf{A}_i^p\}^T\{\mathbf{J}(r_i,\theta_i)\} + \{\mathbf{A}_i^e\}^T\{\mathbf{I}(r_i,\theta_i)\}\Big)e^{\hat{i}\omega t} \tag{4.12}$$

$$\{\mathbf{A}_i^p\} = \{\mathbf{A}_{i,1}^p\} + \{\mathbf{A}_{i,2}^p\} \tag{4.13}$$

$$\{\mathbf{A}_i^e\} = \{\mathbf{A}_{i,1}^e\} + \{\mathbf{A}_{i,2}^e\} \tag{4.14}$$

where subscripts 1 and 2 denote wave coefficients generated by the excitation force and distributed forces associated with the piezoelectric disk, respectively. Using the coordinate transformations Eqs. (4.5-4.6) and the identity $H_0^{(2)}(\hat{i}z) = (\frac{-2\hat{i}}{\pi}K_0(z))$, the excitation wave coefficients are expressed as

$$\{A_{i,1}^p\}_n = (-1)^n\frac{\hat{i}}{\Delta}e^{-\hat{i}\theta_i}H_n(kd_i) \tag{4.15}$$

$$\{A_{i,1}^e\}_n = \frac{-2}{\pi\Delta}e^{-\hat{i}\theta_i}K_n(kd_i) \tag{4.16}$$

where $\Delta = 8k^2B/F_0$ and (d_i,θ_i) denotes the location of the point source in the (x_i,y_i) coordinate system. The incident wave coefficients (Eqs. (4.13-4.14)) are now

substituted into Eq. (4.9) to yield an updated multiple scattering formulation,

$$\{\mathscr{B}\} = [\mathscr{L}]\{\mathscr{A}_1\} + [\mathscr{L}]\{\mathscr{A}_2\} \tag{4.17}$$

to be used with Eq. 4.4. It remains to determine the incident coefficients held by $\{\mathscr{A}_2\}$, which ultimately requires determination of the distributed forces $f(r,\theta)$.

Returning to the two coupled subdomains, and setting equal their responses in their adjoining regions, the unknown distributed interaction forces between the piezoelectric and infinite layer can be identified. Expressing the plate's displacement field as,

$$w_{plate}(r,\theta,t) = w_F(r,\theta,t) + w_f(r,\theta,t,f(r,\theta)) + \sum_{j=1}^{N} w_j^{scr}(r,\theta,t,f(r,\theta)), \tag{4.18}$$

and the disk's displacement field as,

$$w_{disk}(r,\theta,t) = w_P(r,\theta,t,-f(r,\theta)), \tag{4.19}$$

the adjoining condition requires

$$w_F(r,\theta,t,F) + w_f(r,\theta,t,f(r,\theta)) + \sum_{j=1}^{N} w_j^{scr}(r,\theta,t,f(r,\theta))$$

$$= w_P(r,\theta,t,-f(r,\theta)) \quad \forall\theta \text{ and } r < r_0 \tag{4.20}$$

Displacement fields appearing in Eq. (4.20) require further development before returning to find the interaction forces.

Since the steady-state behavior of the system is desired at the excitation frequency ω, and since the model is strictly linear, each displacement field can be written as,

$$w_\Gamma(r,\theta,t) = \phi_\Gamma(r,\theta)e^{\hat{i}\omega t} \tag{4.21}$$

where subscript Γ can assume either F, f or P. Using the thin plate Green's function, the displacement of the plate due to an applied harmonic point force is given as [55, 56],

$$\phi_F(r,\theta) = \frac{F_0}{8BIk_B^2\hat{i}}[H_0^{(2)}(k_B\rho_1) - H_0^{(2)}(-\hat{i}k_B\rho_1)], \tag{4.22}$$

where $\rho_1 = \sqrt{r_1^2 + r^2 - 2rr_1cos(\theta-\theta_1)}$ denotes the distance between the source and any location (r,θ), $H_i^{(2)}$ denotes the Hankel function of the second kind at the ith order, $k_B = \frac{\omega}{c_B}$ the flexural wave number, $c_B = \sqrt[4]{\frac{B}{m}}\sqrt{\omega}$ the phase velocity of bending waves, $B = \frac{E}{1-\nu^2}$ the bending stiffness, E Young's Modulus, ν Poisson's ratio, $I = \frac{h_s^3}{12}$ the cross-sectional moment of inertia, and m the mass per unit area. The same Green's function can be used to find the response of the plate due to distributed interaction forces $f(r,\theta)$,

$$\phi_f(r,\theta) = \frac{1}{8BIk_B^2\hat{i}}\left(\int_0^{2\pi}\int_0^{r_0} f(r^*,\alpha)\Pi(k_B,\rho_0)\, r^* dr^*\, d\alpha\right), \tag{4.23}$$

where $\rho_0 = \sqrt{r^{*2} + r^2 - 2rr^*cos(\theta-\alpha)}$ denotes the distance between the distributed

interaction force at (r^*, α) and any location (r, θ). In addition, $\Pi(k_B, \rho_0)$ is defined as

$$\Pi(k_B, \rho_0) = [H_0^{(2)}(k_B\rho_0) - H_0^{(2)}(-\hat{i}k_B\rho_0)]. \tag{4.24}$$

The unknown distributed force $f(r^*, \alpha)$ on the right-hand side of Eq. (4.23) is represented in expanded form using an array of Bessel functions,

$$f(r^*, \alpha) = \{\mathbf{f}\}^T\{\mathbf{J}^*(r^*, \alpha)\} \tag{4.25}$$

where $\{J^*(r, \theta_i)\}_{mn} = J_m(\lambda_{mn}r)e^{\hat{i}m\theta_i}$, λ_{mn} denotes the eigenvalues for free edge boundary conditions [57] and J_m denotes the mth-order Bessel functions of the first kind. The array $\{\mathbf{f}\}$ holds expansion coefficients f_{mn} (see Chapter 3) determined simultaneously with the scattered wave coefficients at the end of the analysis procedure. Note that $\{\mathbf{J}^*\}$ is distinct from $\{\mathbf{J}\}$ introduced earlier. To simplify the analysis, the distributed forces are represented as a single point force,

$$F_1 = \{\mathbf{f}\}^T \int_0^{2\pi} \int_0^{r_0} \{\mathbf{J}^*(r^*, \alpha)\} r^* \, dr^* \, d\alpha \tag{4.26}$$

located at an equivalent location determined by,

$$X_e = \{\mathbf{f}\}^T \int_0^{2\pi} \int_0^{r_0} \{\mathbf{J}^*(r^*, \alpha)\} r^* r^* cos\alpha \, dr^* \, d\alpha \tag{4.27}$$

$$Y_e = \{\mathbf{f}\}^T \int_0^{2\pi} \int_0^{r_0} \{\mathbf{J}^*(r^*, \alpha)\} r^* r^* sin\alpha \, dr^* \, d\alpha \tag{4.28}$$

Finally, the wave expansion coefficients for the distributed force generated by the piezoelectric disk $\{A^p_{i,2}\}_n$, $\{A^e_{i,2}\}_n$ can be expressed as,

$$\{A^p_{i,2}\}_n = (-1)^n \frac{\hat{i}}{\hat{\Delta}} e^{-\hat{i}\theta_{s_i,e}} H_n(kd_{s_i,e}) \tag{4.29}$$

$$\{A^e_{i,2}\}_n = \frac{-2}{\pi\hat{\Delta}} e^{-\hat{i}\theta_{s_i,e}} K_n(kd_{s_i,e}) \tag{4.30}$$

where $\hat{\Delta} = 8k^2B/F_1$ and $(d_{s_i,e}, \theta_{s_i,e}) = (\sqrt{X_e^2 + Y_e^2}, tan^{-1}\frac{Y_e}{X_e})$ are the coordinates of the equivalent interaction force in the (x_i, y_i) coordinate system. In order to completely specify, these coefficients still require solution of f_{mn}.

The piezoelectric disk's displacement transforms according to,

$$\phi_P(r,\theta) = \{\boldsymbol{\eta}\}^T \{\mathbf{J}^*(r,\theta)\} \tag{4.31}$$

where $\{\boldsymbol{\eta}\}$ holds expansion coefficients η_{mn} related to f_{mn} by

$$\eta_{mn} = \frac{-f_{mn} + \tilde{\theta}_{mn} V_0}{\omega^2_{mn} - \omega^2 + 2\hat{i}\zeta_{mn}\omega\omega_{mn}}, \tag{4.32}$$

and where V_0 denotes the peak voltage (harvester voltage given by $v(t) = V_0 e^{\hat{i}\omega t}$), ω_{mn} represent undamped natural frequencies and ζ_{mn} denote modal damping coefficients. Note that since forces $-f(r,\theta)$ are considered to act on the disk, a minus sign appears in front of f_{mn} in Eq. (4.32), which is absent from Eq. (2.20). Finally, note that $\tilde{\theta}_{mn}$ is non-zero for $m = 0$ only. This implies that $\tilde{\theta}_{mn}$ is solely a function of r.

The peak voltage V_0 requires final consideration before returning to the adjoin-

ing condition. The integral form of Gauss's equation provides an electromechanical coupling equation which relates the harvester's displacement to its voltage,

$$\frac{d}{dt}\int_A \mathbf{D}\cdot\mathbf{n}dA = \frac{v(t)}{R_l}, \tag{4.33}$$

where $\mathbf{n}$ denotes the unit vector outward from electrode surface, $\mathbf{D}$ the electric displacement vector, R_l the resistance of the electrical circuit, and A the electrode's surface area over which the integral is performed. The inner product between the unit vector $\mathbf{n}$ and the electric displacement $\mathbf{D}$ vector yields the electric displacement component D_3. Substituting the disk's displacement field into the above equation, and following a standard evaluation procedure provided in [53] for a rectangular piezoelectric plate (herein the cylindrical-form of the operators are required) yields,

$$\hat{i}\omega C_p V_0 + \frac{V_0}{R_l} + \hat{i}\omega\{\boldsymbol{\eta}\}^T\{\hat{\boldsymbol{\theta}}\} = 0, \tag{4.34}$$

where $\{\hat{\boldsymbol{\theta}}\}$ denotes an array holding $\tilde{\theta}_{mn}$, $C_p = (\pi r_0^2 \bar{\varepsilon}_{33}^S)/h_p$ is the equivalent capacitance of the electrical circuit and $\bar{\varepsilon}_{33}^S$ denotes a permittivity component. Eqs. (4.31) and (4.34) then represent coupled equations for the disk displacement and voltage.

With the displacement fields and electric circuit completely specified, attention can return to the adjoining equation used, in part, to determine interaction forces. Substituting Eqs. (4.4) and Eqs. (4.31) into Eq. (4.20) yields an updated condition,

$$\left(\{\mathbf{A}_O^p\}^T\{\mathbf{J}(r,\theta)\} + \{\mathbf{A}_O^e\}^T\{\mathbf{I}(r,\theta)\} + \sum_{j=1}^{N}\{\mathbf{B}_j^p\}\{\mathbf{J}(r,\theta)\} + \{\mathbf{B}_j^e\}\{\mathbf{I}(r,\theta)\}\right)\Big|_{r<r_0}$$

$$= \{\boldsymbol{\eta}\}^T \{\mathbf{J}^*(r,\theta)\}\Big|_{r<r_0} \tag{4.35}$$

where $\{\mathbf{A}_o^{p,e}\}$ denote incident wave coefficients referencing the piezoelectric disk's coordinate system. Identities must be employed such that a common set of expansion functions are used in all expressions of Eq. (4.34). Transforming from $\{\mathbf{J}(r,\theta)\}$ to $\{\mathbf{J}^*(r,\theta)\}$ is accomplished via,

$$\{J(r,\theta)\}_m = J_m(kr)e^{\hat{i}m\theta} = \sum_{n=0}^{\infty} b_{mn} J_m(\lambda_{mn} r) e^{\hat{i}m\theta} \tag{4.36}$$

$$\{I(r,\theta)\}_m = I_m(kr)e^{\hat{i}m\theta} = \sum_{n=0}^{\infty} c_{mn} J_m(\lambda_{mn} r) e^{\hat{i}m\theta} \tag{4.37}$$

where

$$b_{mn} = \int_0^{\infty} \sqrt{\lambda_{mn}} J_m(kr) J_m(\lambda_{mn} r) r \, dr, \quad c_{mn} = \int_0^{\infty} \sqrt{\lambda_{mn}} I_m(kr) J_m(\lambda_{mn} r) r \, dr \tag{4.38}$$

Introducing

$$\{\tilde{A}^p\}_{mn} = \{A^p\}_m b_{mn} \tag{4.39}$$

$$\{\tilde{A}^e\}_{mn} = \{A^e\}_m c_{mn} \tag{4.40}$$

$$\{\tilde{B}_j^p\}_{mn} = \{B_j^p\}_m b_{mn} \tag{4.41}$$

$$\{\tilde{B}_j^e\}_{mn} = \{B_j^e\}_m c_{mn} \tag{4.42}$$

and substituting Eqs. (4.36-36) into equation (4.35) yields,

$$\left\{ \{\tilde{\boldsymbol{A}}^p_{O,1}\}^T\{\mathbf{J}^*(r,\theta)\} + \{\tilde{\boldsymbol{A}}^e_{O,1}\}^T\{\mathbf{J}^*(r,\theta)\} + \{\tilde{\boldsymbol{A}}^p_{O,2}\}^T\{\mathbf{J}^*(r,\theta)\} + \{\tilde{\boldsymbol{A}}^e_{O,2}\}^T\{\mathbf{J}^*(r,\theta)\} \right.$$

$$\left. \left(\sum_{j=1}^{N} \{\tilde{\boldsymbol{B}}^p_j\}^T[\mathbf{R}^p_{jO}]\{\mathbf{J}^*(r,\theta)\} + \{\tilde{\boldsymbol{B}}^e_j\}^T[\mathbf{R}^e_{jO}]\{\mathbf{J}^*(r,\theta)\} \right) \right\} \Bigg|_{r<r_0} = \{\boldsymbol{\eta}\}^T\{\mathbf{J}^*(r,\theta)\} \Bigg|_{r<r_0} \quad (4.43)$$

The peak voltage V_0 still requires incorporation into the expressions. From the circuit equation, Eq. (**??**),

$$V_0 = -\frac{\hat{i}\omega}{\hat{i}\omega C_p + \frac{1}{R_l}} \{\boldsymbol{\eta}\}^T\{\tilde{\boldsymbol{\theta}}\}, \quad (4.44)$$

which when followed by substitution of Eq. (4.32) yields,

$$V_0 = \hat{i}\omega \frac{\sum_{n=0}^{\infty}\sum_{m=0}^{\infty} \frac{f_{mn}\tilde{\theta}_{mn}}{\omega^2_{mn}-\omega^2+2\hat{i}\zeta_{mn}\omega\omega_{mn}}}{\hat{i}\omega C_p + \frac{1}{R_l} + \sum_{n=0}^{\infty}\sum_{m=0}^{\infty} \frac{\hat{i}\omega\tilde{\theta}^2_{mn}}{\tilde{\theta}^2_{mn}-\omega^2+2\hat{i}\zeta_{mn}\omega\omega_{mn}}}. \quad (4.45)$$

The collected equations for the electroacoustic multiple scattering problem are now readily assembled. Equations (4.17), (4.43), and (4.45) form a system of equations sufficient for finding the desired expansion coefficients f_{mn}. Their solution is complicated by the fact that coefficients f_{mn} appear in the nonlinear expression $\theta_{s_i,e} = tan^{-1}\frac{Y_e}{X_e}$. However, the system can be posed in a linear form using the reasonable assumption that $\theta_{s_i,e} \approx \theta_{s_i}$, or equivalently that $\sqrt{X_e^2 + Y_e^2} \ll d_{s_i}$ for each scatterer i (see

Figure 4.3), yielding

$$[\mathscr{U}]\mathscr{F} = \mathscr{E} \tag{4.46}$$

where

$$\mathscr{F} = [f_{00} \;\; f_{01} \;\; f_{02} \ldots f_{10} \;\; f_{11} \ldots f_{MS}]^T \tag{4.47}$$

holds the distributed force expansion coefficients truncated to sizes M and S, and $\mathscr{U}$ denotes a coefficient matrix whose elements follow from Eqs. (4.17), (4.43), and (4.45). The final step in quantifying the interaction forces is the inversion of $[\mathscr{U}]$,

$$\mathscr{F} = [\mathscr{U}]^{-1}\mathscr{E} \tag{4.48}$$

With expressions now known for all f_{mn}, all other response quantities follow by back-substitution.

4.3 Modeling Results

4.3.1 MEH inclusion study

Results are first generated using the developed formulation to assess the focusing efficacy of multiple inclusion types. Two elliptical arrangements of scatterers are used which are similar in size and shape to that studied previously [39] using raised stubs. Here, instead, through-holes and rigid inclusions are studied such that the height of

rigid scatterers is equal to the thickness of the host plate. The first arrangement has major and minor radii $a = 10cm$ and $b = 9cm$, respectively, and the second has $a = 4cm$ and $b = 3cm$. Twenty-five scatterers with radius $a_i = 3mm$ for the first case, and $a_i = 1mm$ for the second case, are evenly-spaced in the x-direction along a semi-elliptical path. The number of scatterers chosen was arrived at after simulating multiple scenarios. Using less scatterers resulted in a weaker focal point, while using more scatterers decreased the spacing between each scatterer, resulting in computational difficulties[1] without significant changes to the focal intensity. A point source excitation is placed at the first focal point of the complete ellipse. Consequently, for the larger complete ellipse the first focal point is calculated to be at $x = 0.04358$, $y = 0cm$ (where the system is excited) while the second focal point is at $x = -0.04358$, $y = 0cm$ (where the piezoelectric disk will be located later). The first focal point of the smaller complete ellipse is calculated to be at $x = 0.0264$, $y = 0cm$, while the second focal point is at $x = -0.0264$, $y = 0cm$. The origin of the ellipse is at $x = 0$, $y = 0$. In order to enhance the effectiveness of the system, the spacing between scatterers should be on the order of the incident wavelength, which is related to the excitation frequency. If the host layer material is aluminum with a thickness of $h = 1mm$, the excitation frequency should be greater than $f = 1000Hz$ for the first case and $f = 5000Hz$ for the second.

Figure 4.4 depicts the scattered wavefield displacement amplitude of the plate at excitation frequencies of $f = 2kHz$ and $f = 3.5kHz$ for the rigid and void inclusions,

[1] As described in [58], the validity criteria for the Bessel function transformations used herein requires that no scatterer's origin falls within the footprint of another scatterer.

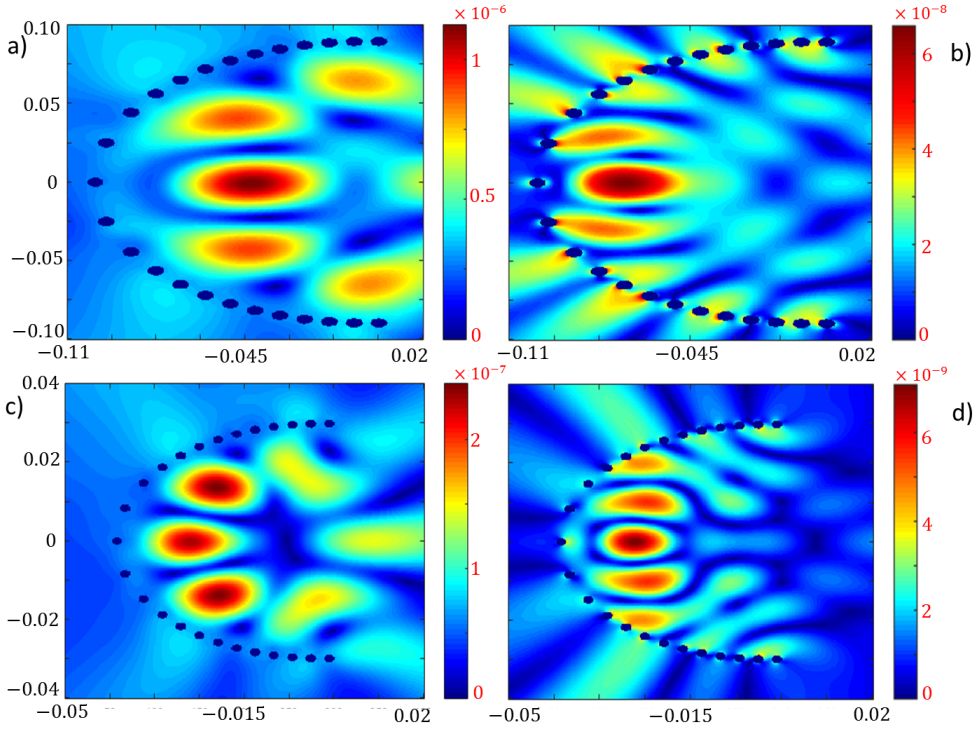

Figure 4.4: ***Scattered wave displacement amplitude from the a) rigid inclusion*** *($a = 10$* ***and*** *$b = 9$**cm**)**, **b) void inclusion*** *($a = 10$* ***and*** *$b = 9$**cm**)**, **c) rigid inclusion*** *($a = 4$* ***and*** *$b = 3$**cm**)**, **and d) void inclusion*** *($a = 4$* ***and*** *$b = 3$**cm**)**.*

respectively, when $a = 10cm$. For the smaller case ($a = 4cm$), frequencies $17kHz$ and $30kHz$ are used for the rigid and void inclusions, respectively. The left column depicts results for rigid inclusions, while the right depicts results for voids. Notable in all sub-figures are undesirable side lobes, above and below the main focal point, observed in other studies [39, 40, 41] and attributed to the truncated elliptical shape. Note that the frequencies chosen for each ellipse and inclusion type are those that roughly minimize these side lobes, thus enabling fair performance comparisons. For equal inclusion sizes, Figure 4.4 indicates that the rigid inclusion type focuses more energy inwards, leaks less energy outwards, and exhibits lower-magnitude side lobes compared to voids. Although this study suggests performance with rigid inclusions

outperforms voids, plates with rigid inclusions can be difficult to manufacture and likely increase weight, and thus voids may be the more attractive option.

4.3.2 Shape optimization without harvester

To enhance the efficiency of the MEH system, an *ad hoc* optimization is performed next whereby elliptical aspect ratios are evaluated in an effort to reduce side lobes and increase harvested power. During this optimization, the major radius of the ellipse is fixed consistent with the two values considered in Sec. 5.3.1 ($a = 4, 10\ cm$), with 7 different values (from 1.0 to 2.5 in 0.25 increments) chosen for the a/b ratio. Frequency is constant during the optimization and is same as Sec. 4.3.1. The positions of scatterers are again evenly-spaced along the x-direction.

To optimize the energy of the system near the harvesting focal point, the system is first divided into five zones (see Figure 4.5). Zone 1 is centered at the focal point and has a radius equal to the the harvester radius (added later), Zone 2 consists of an annulus about Zone 1, and Zones 3 and 4 contain the area where side lobes are observed. All other areas are covered by Zone 5. Since the maximum energy close to the focal area is desired, the optimization cost function to be minimized is defined as,

$$f_{cost} = -2w_1 - 1.5w_2 + 2w_3 + w_4 + 0.5w_5 \tag{4.49}$$

where w_j stands for the average displacement magnitude of all points in zone j. The optimization is relatively insensitive to the weightings chosen as long as Zones 1 and 2 are weighted negatively (thus rewarding focusing), and Zones 3 - 5 positively (thus

penalizing side lobes).

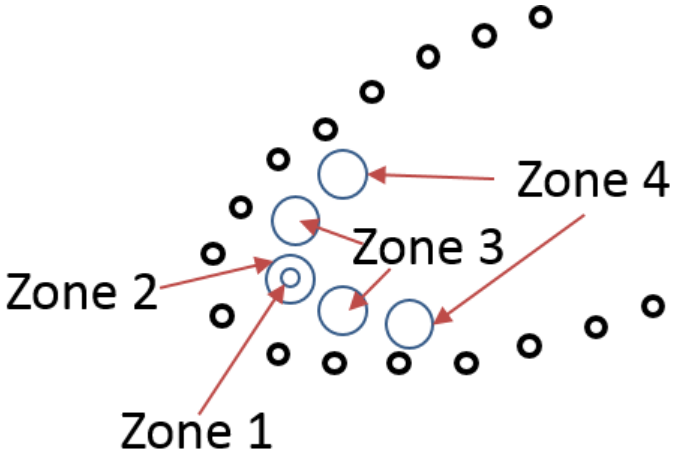

Figure 4.5: ***Zones employed for system optimization.***

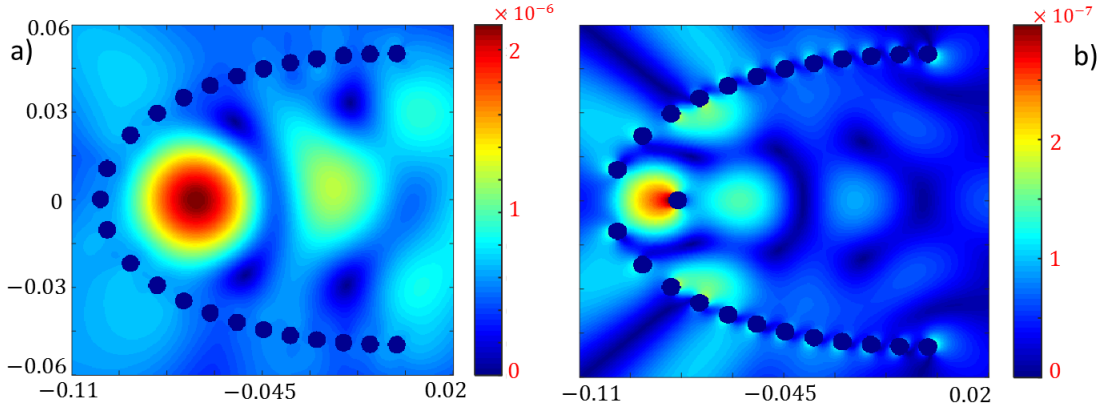

Figure 4.6: ***Optimized shape of scattered wave displacement for the a) rigid and b) void inclusion for*** $a = 10\ cm$.

Figure 4.6 depicts the scattered wave response after performing the ratio optimization for the elliptical pattern scatterers characterized by $a = 10\ cm$, for both rigid and inclusions; Figure 4.7 depicts similar results for $a = 4\ cm$. For both cases and both inclusion types, best performance is obtained for a ratio of $a/b = 2$. Note that the performance of the void inclusions has been improved by placing the scatterer previously located at $x = -a, y = 0$ to the right of the ellipse's focal point. This

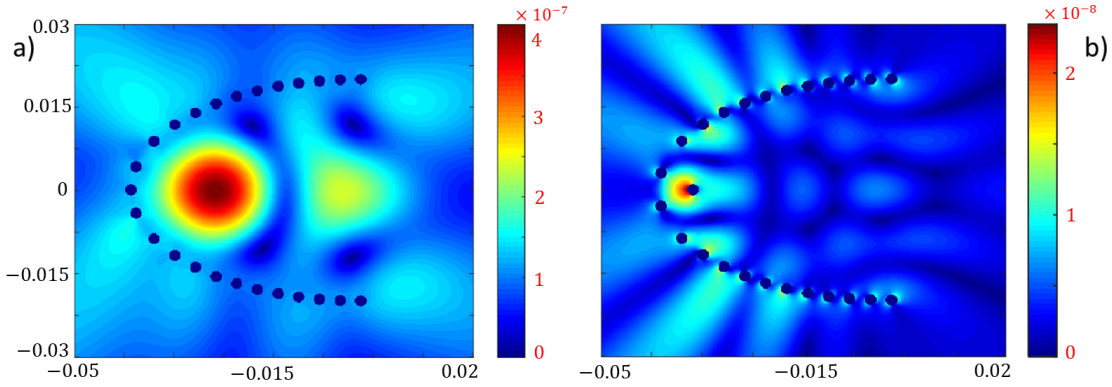

Figure 4.7: ***Optimized elliptical aspect ratio of scattered wave displacement for the a) rigid and b) void inclusion for*** $a = 4\ cm$***.***

sharpens the focal point by reflecting energy radiating from the scatterers and to the right of the focal point, and directing it back towards the focal point. This strategy is found not to be effective for the rigid inclusions.

The *ad hoc* optimized systems strongly focus a majority of incident energy very near the focal point locating the piezoelectric disk. In addition, these optimized designs effectively remove side lobes. From this point forward, only the case with a smaller ellipse and void inclusions is considered in anticipation of comparisons to experiments where the ease of manufacturing voids, and the smaller domain required by higher frequencies, make this choice most attractive.

4.3.3 Frequency analysis of the system

The chosen optimized system is next evaluated over a range of frequencies to characterize its broadband nature. In particular, efficacy of the design at each frequency is based on the appearance, or not, of focal points without side or spurious lobes. It is found that the minimum frequency which results in only one focal point, without side lobes, is determined to be approximately $\omega_{min} = 12.5kHz$, and the maximum

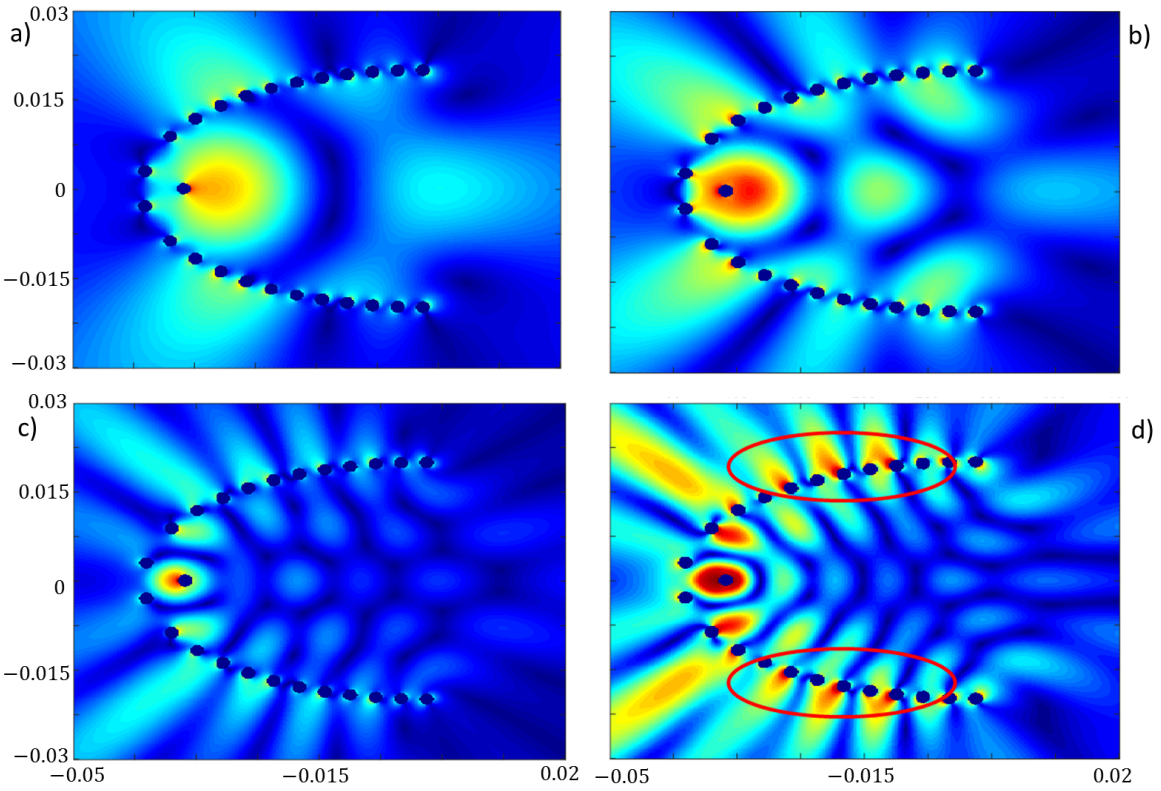

Figure 4.8: ***System wavefield displacement generated by point source excitation at frequency a)*** $\omega = 5kHz$***, b)*** $\omega_{min} = 12.5kHz$***, c)*** $\omega_{max} = 45kHz$***, and d)*** $\omega = 60kHz$***.***

frequency is determined to be approximately $\omega_{max} = 45kHz$. Figure 4.8 depicts the system response at these and other frequencies. As indicated, for frequencies less than ω_{min}, no discernible focal point is observed (see Figure 4.8a) since the associated wavelength at these lower frequencies is larger than that of the scatterer's lattice spacing, reducing scattering intensity. For frequencies exceeding ω_{max}, the scatterers generate additional propagating modes of varying direction. Thus spurious lobes (see red ovals in Figure 4.8d) begin to appear which decrease harvested power. A qualitative summary of these considerations is provided in Figure 4.9a, while Figure 4.9b quantifies the normalized displacement at the focal point as a function of frequency.

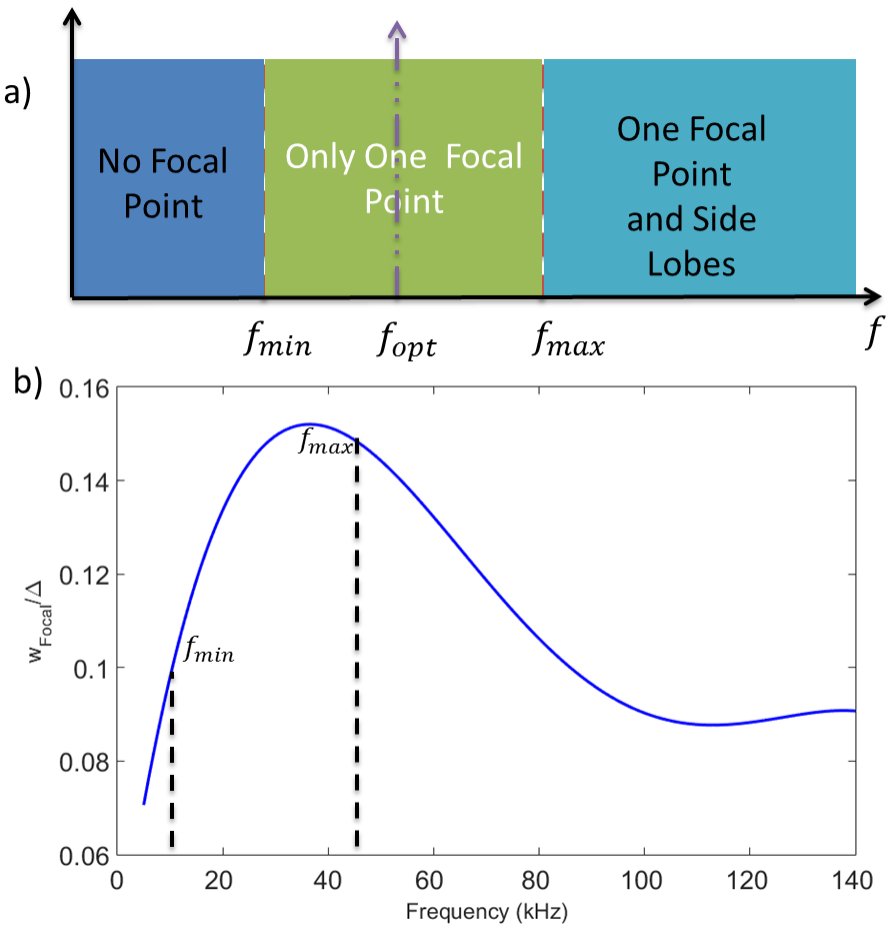

Figure 4.9: ***Results for optimized system: a) qualitative system behavior as a function of frequency, and b) normalized focal displacement.***

4.3.4 Shape optimization with harvester

The previous sections performed optimization to remove side lobes and increase performance in the absence of the piezoelectric harvester. Next, further optimization is performed with the piezoelectric harvester present. As such, the material properties of SM111 are used for modeling the harvester [54]. The thickness of the piezoelectric disk chosen is $h_p = 0.4mm$, and the radius of the disk is $r_0 = 0.75mm$. In the final optimization, the y-position of each scatterer is varied using the chosen excitation

frequency of $f = 30kHz$. More specifically, the vertical location of each scatterer is allowed to vary from $y_{0i} - 1\ mm$, to $y_{0i} + 1\ mm$, where y_{0i} is the original location of scatterer i. The cost function defined in Sec. 4.3.2 is retained and optimization is performed using a standard MATLAB unconstrained optimization function call. Figure 4.10 documents the perturbed scatterer locations and wavefield obtained after optimization. The optimization results in small, but evident, y-offsets for several scatterers. Predicted response results show that in comparison to Figure 4.6b, the displacement magnitude at the focal point has been further increased (the placement of the harvester at this point prevents reporting of the true magnitude increase).

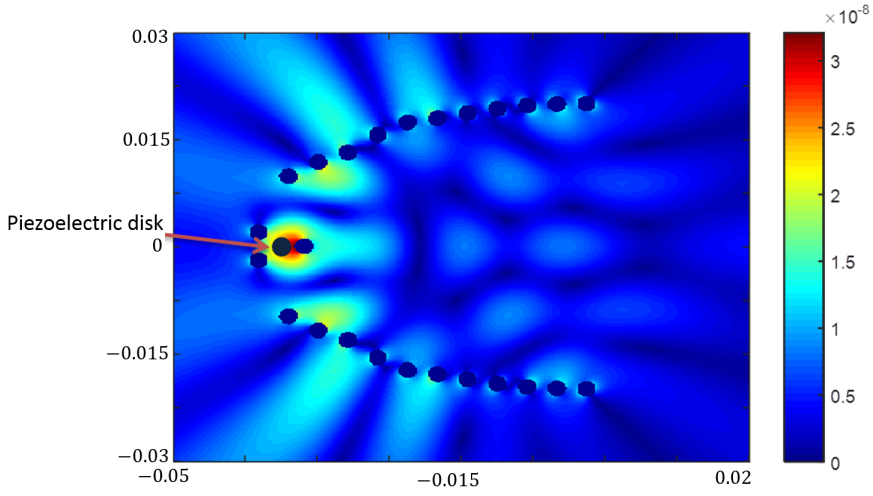

Figure 4.10: ***Scattered wavefield displacement generated by point source excitation when the piezoelectric disk is present at the second focal point (following optimization).***

To measure the improvement in harvested power from the non-optimized case, the system of Figure 4.4d was simulated with the piezoelectric harvester. This results in a predicted generation of approximately 0.4 μW of electric power ($P = V_0^2/2R_l$) using a resistor characterized by $R_l = 1000\Omega$. Using the same resistor, the predicted

generated power for the optimized case is 0.074 mW, which represents an approximate increase of 185 fold.

4.3.5 Experimental apparatus and validation

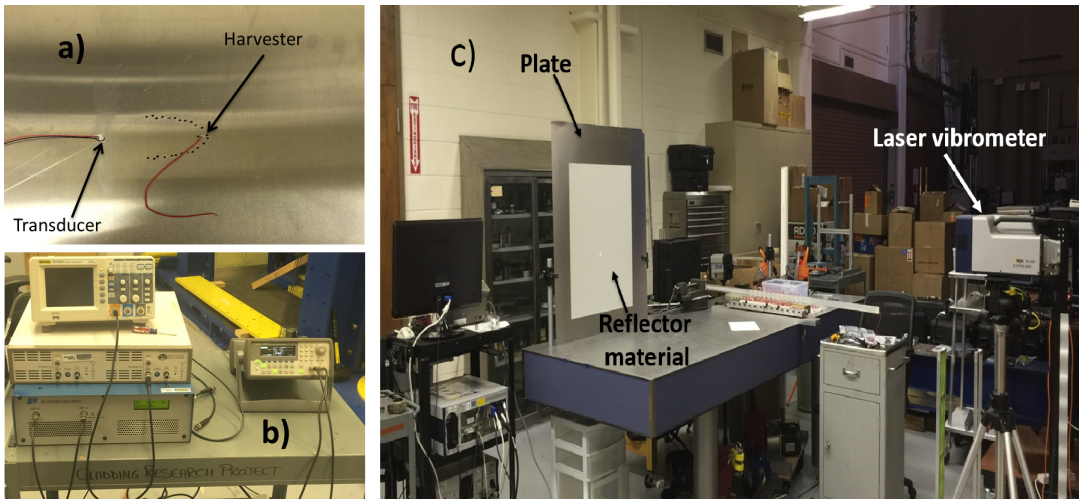

Figure 4.11: ***Experimental setup including a) an aluminum plate hosting piezoelectric transducers for exciting and harvesting waves, b) function generator and amplifier for generating requisite voltage profiles, and c) overall setup showing mounted plate (left) and laser vibrometer (right) used to measure backside transverse plate velocities.***

This section describes a set of experiments aimed at validating the presented analytical modeling approach. Figure 4.11 details the experimental setup. The experiments are limited to measuring the surface displacement field (using a scanning laser vibrometer) and harvester voltage. An epoxy-bonded piezoelectric transducer (Steiner Martins SMD05T04R111WL, 3M DP270 Epoxy Adhesive) with thickness $h_p = 0.4mm$ excites the system in response to a generated voltage profile. The disk has a radius of $2.5mm$ and an effective capacitance of $C_p = 1nF$. A second transducer (Steiner Martins SMD03T04S311) is used for the harvester. This disk has a radius of $1.5mm$ and an effective capacitance of $C_p = 0.5nF$, respectively. The alu-

minum host plate disk has thickness $h_s = 1mm$ (see Table. 4.1, which lists other experiment parameters). Note that material damping values are set to zero since their effect is minor in comparison to the radiative damping resulting from the infinite plate. The first transducer is excited by 40 cycles of $f = 30kHz$, 100 mV_{pp} voltage using a function generator (Agilent 33220A) coupled to a voltage amplifier (B&K 1040L). A Polytec PSV-400 scanning laser Doppler vibrometer measures the resulting wavefield over a $10cm \times 8cm$ square area, using the backside of the plate, with a 250×250 grid resolution. The distance between the excitation and harvester centers is 3.4 cm. Wavefield images and RMS distributions are obtained by recording the out-of-plane plate response covering the piezoelectric harvester and the square subdomain. Proper triggering of the laser measurements allows the reconstruction of the out-of-plane velocity field, while time integration of the recorded responses yields RMS distributions.

Table 4.1: ***Properties, materials and electrical parameters***

Domain	Material	Thickness mm	Radius mm	Capacitance	*Damping*
Piezoelectric harvester	SMD03T04S311	0.4	1.5	0.5	0
Piezoelectric transducer	SMD05T0R111WL	0.4	2.5	1	0
Host layer	Aluminum	1	∞	0	0

Void inclusions are created in the aluminum plate using the perturbed center locations resulting from the final optimization study. Figure 4.12 presents the the scattered wave contour obtained experimentally using a 1000 Ω resistor connected to the piezoelectric disk. The measured wavefield of Figure 4.12 closely matches that predicted in Figure 4.10. A strong focus can be observed in both figures, with a

notable absence of side lobes in the vicinity of the harvester. Weak leakage, and its associated direction, is also in agreement in both results sets. Figure 4.13 presents a comparison of the analytically-predicted and experimentally-measured peak voltage as a function of load resistance R_l at $30kHz$. A resistance substituter (IET Labs model RS-200) is used to generate a full sweep of resistance from 100 Ω (close to short-circuit condition) to 10 $M\Omega$ (close to open-circuit condition). Using a National Instruments data acquisition system (Model cDAQ-9178), voltage across the resistor is measured and output power is calculated accordingly. For comparison to the analytical model, the equivalent value of the point force needed is found by applying the source voltage and waveform to the piezoelectric disk attached to a host plate without a harvester. Then, by measuring the displacement of a point $10cm$ away from the transducer, excitation force F_0 is inferred. Note that the figure documents good agreement between the analytically-predicted and experimentally-obtained peak voltage over a large range of load resistances.

A final comparison documenting enhanced performance following optimization is given in Figure 4.14. There, a plate produced with voids corresponding to the non-optimized pattern shown in Figure 4.4d is experimentally explored and the average peak power versus load resistance trend is compared to the final optimized case. It can be observed that the optimized case outperforms the non-optimized case over all resistances considered, typically by two orders of magnitude in average power. Note also that the peak resistance value of both cases roughly conforms to that predicted using a classical weakly-coupled prediction of $1/(\omega C_p) = 5200\Omega$.

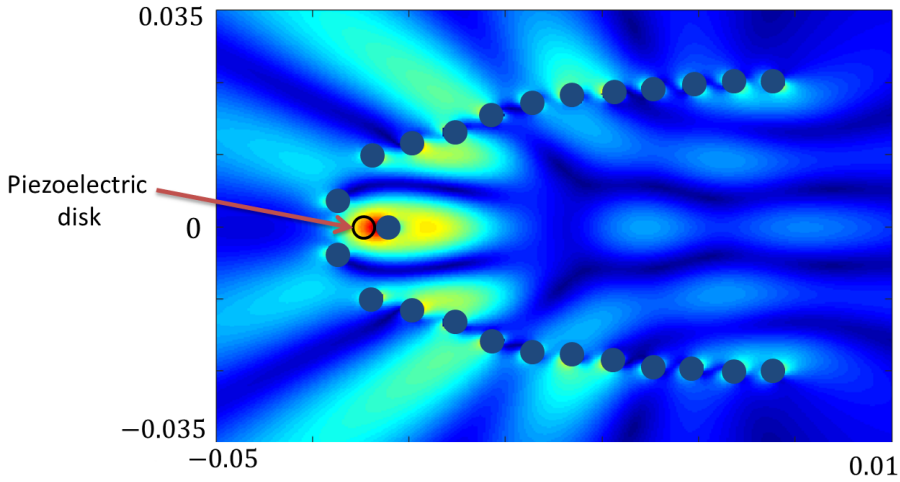

Figure 4.12: ***Scattered wavefield displacement generated by point source excitation when the piezoelectric disk is presented at the second focal point after performing optimization.***

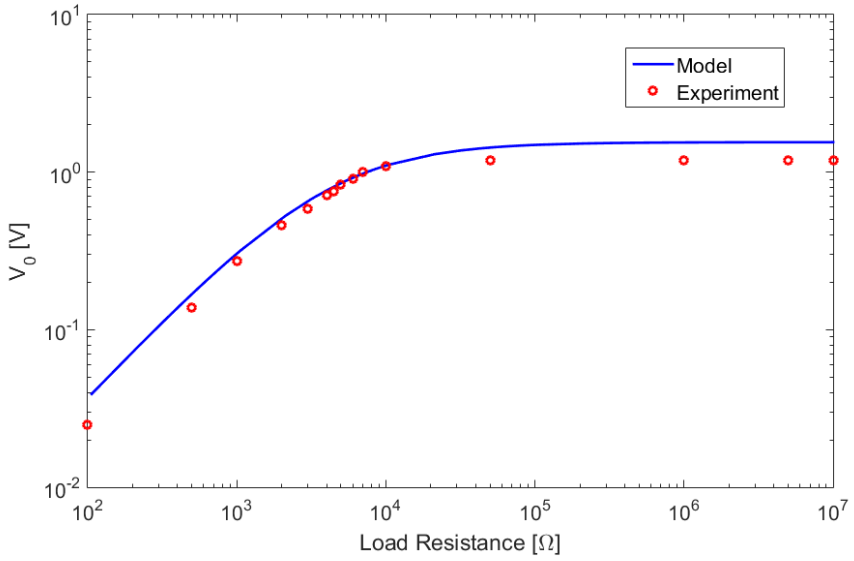

Figure 4.13: ***Voltage generated by the piezoelectric harvester for varying values of load resistance.***

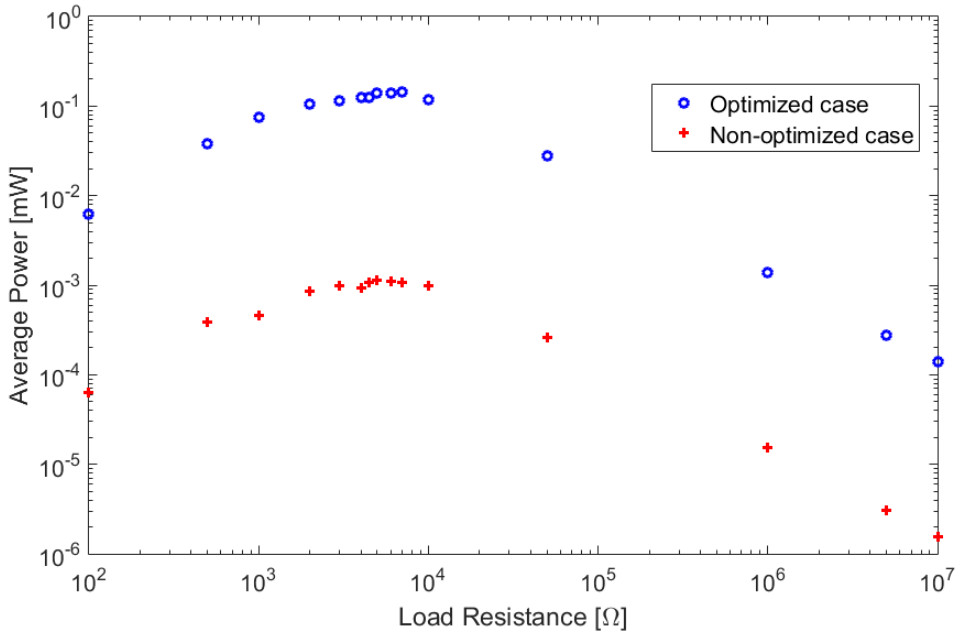

Figure 4.14: ***Average power generated by the piezoelectric harvester for varying values of load resistance.***

Chapter 5

Piezoelectric T-Matrix

5.1 Overview

To support continued MEH concept development, this chapter proposes a fully-coupled T-matrix formulation for analyzing scattering of incident wave energy from a piezoelectric patch attached to a thin plate. In comparison to Chapter 4 where a specialized multiple scattering approach was developed around a single piezoelectric harvester, this chapter formulates a re-usable T-matrix for the piezoelectric harvester, which in turn can be used in multiple scattering scenarios incorporating several harvesters. Such a T-matrix may have utility outside of MEH studies, such as in diagnostics of defects using propagating waves, and other scenarios where piezoelectric disks are used to generate and/or sense propagating waves. Similarly, while the previous chapter placed emphasis on modal Bessel functions arising from patch vibration modes, the present chapter places this emphasis on wave coefficients referencing unbounded Bessel functions. This enables isolation of the piezoelectric patch as a global source of wave scattering, and thus ultimately leads to determination of the desired characteristic T-matrix.

The utility of a T-matrix formalism is most apparent in scenarios employing multiple piezoelectric harvesters, where it can be re-used with other T-matrices in a multiple scattering context to compute the total wavefield and other response quantities,

such as harvested power. Following development of the requisite T-matrix, harvesting in an example funnel-shaped metamaterial waveguide structure is predicted using the multiple scattering approach. Enhanced wave energy harvesting predictions are verified through comparisons to experimental results of a funnel-shaped waveguide formed by placing rigid aluminum inclusions in, and multiple piezoelectric harvesters on, a Lexan plate.

The present chapter is organized as follows: first, a multiple scattering formalism is reviewed for predicting the total wavefield resulting from plane waves incident on multiple scatters attached to an infinite host plate. Then a T-matrix for a circular piezoelectric disk bonded to the aforementioned infinite plate is derived. Using rigid inclusion as a means of scattering, the response of a funnel-shaped MEH structure incorporating several harvesters is computed to assess its potential for wave energy harvesting. Following these studies, a set of experiments is described whose results are in very good agreement with those predicted using the newly formulated T-matrix.

5.2 Piezoelectric T-matrix and Multiple Scattering Implementation

5.2.1 Overview of elastodynamic multiple scattering

Figure 5.1 depicts a representative schematic for multiple-scattering of flexural waves in an infinite host plate incorporating Z-number of scatterers. As illustrated, scatterer i with radius a_i is located at (d_{s_i}, θ_{s_i}) with respect to a global coordinate system. A local coordinate system (r_i, θ_i), attached to the center (X_i, Y_i) of the ith scatterer,

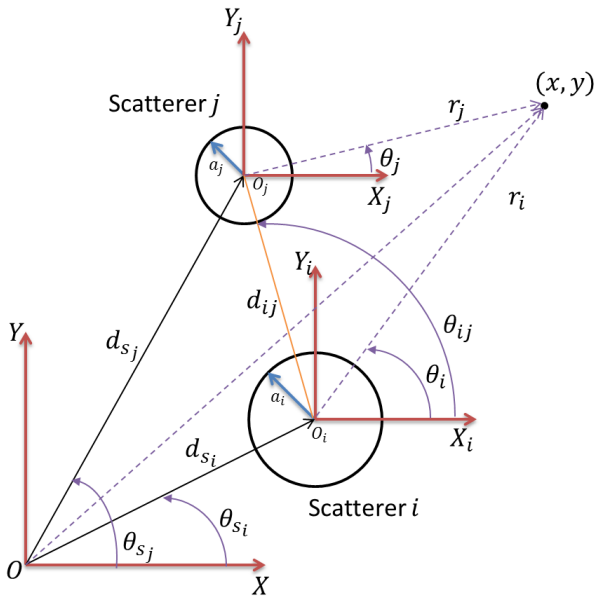

Figure 5.1: ***Schematic of multiple-scattering problem.***

locates any point on the plate. This latter coordinate system is the most natural one for formulating a transformation matrix relating incident and scattered wave coefficients.

In the multiple scattering paradigm, the incident wavefield and all waves generated by scatterers (except those due to self-scattering) are incident on scatterer i and then subsequently re-scattered. This scenario holds for each scatterer j. When known, it is convenient to employ a linear transformation (i.e., T-matrix) for each scatterer which relates the scattered wavefield to the incident wavefield. Before applying the T-matrix transformation to any one scatterer, all waves must be expressed in the ith scatterer's local coordinate system.

The governing equation for wave propagation in a thin, infinite plate is given as

$$D \bigtriangledown^4 w + \rho h \frac{\partial^2 w}{\partial t^2} = f(r, \theta, t) \tag{5.1}$$

where w denotes the plate displacement, $f(r,\theta,t)$ the distributed external forces, h and ρ the thickness and mass density, respectively, and D denotes the plate's flexural stiffness given as $\frac{Eh^3}{12(1-\nu^2)}$ where E represents Young's modulus and ν Poission's ratio. All incident and scattered waves considered herein satisfy Eq. (5.1). Anticipating cylindrical inclusions of radius a_j, the incident wavefield is represented in Bessel form as

$$w^{inc} = \Big(\{\mathbf{A}^p\}^T\{\mathbf{J}(r,\theta)\} + \{\mathbf{A}^e\}^T\{\mathbf{I}(r,\theta)\}\Big)e^{\hat{i}\omega t}, \tag{5.2}$$

and the wavefield scattered by the ith individual scatterer as,

$$w_i^{scr} = \Big(\{\mathbf{B}_i^p\}^T\{\mathbf{H}(r_i,\theta_i)\} + \{\mathbf{B}_i^e\}^T\{\mathbf{K}(r_i,\theta_i)\}\Big)e^{\hat{i}\omega t}, \tag{5.3}$$

where k_B denotes the flexural wave number related to frequency ω by $k_B^2 = \omega\sqrt{\frac{\rho h}{D}}$, $\hat{i} = \sqrt{-1}$. $\{\mathbf{A}^p\}$, $\{\mathbf{A}^e\}$ denote arrays containing the expansion (or wave) coefficients of the propagating and and evanescent incident waves, respectively. Similarly, $\{\mathbf{B}_i^p\}$, $\{\mathbf{B}_i^e\}$ denote arrays holding expansion (or wave) coefficients for propagating and evanescent scattered waves, respectively. Moreover, $\{\mathbf{J}(r,\theta)\}$, $\{\mathbf{I}(r,\theta)\}$, $\{\mathbf{H}(r,\theta)\}$ and $\{\mathbf{K}(r,\theta)\}$ denote arrays holding Bessel functions of the first kind, modified Bessel functions of the first kind, Hankel functions of the first kind, and the modified Bessel functions of the second kind, respectively. These functions compose an orthogonal set of solutions to Eq. (5.1) in radial coordinates. Bessel functions $\mathbf{J}(r,\theta)$ and $\mathbf{I}(r,\theta)$ represent incident waves due to their finite value at the origin, while $\mathbf{H}(r,\theta)$ and $\mathbf{K}(r,\theta)$ represent

scattered waves due to their boundedness at infinity. Any element of these arrays can be represented in separable form, with respect to r and θ, by $\{\mathbf{\Omega}(r,\theta)\}_n = \Omega_n(k_B r)e^{\hat{i}n\theta}$ where n denotes the order of the Bessel function. Expressing the incident and all scattered waves in the ith scatterer's coordinate system, the scatterer's T-matrix ($[\boldsymbol{\tau_i}]$) yields an expression relating the wave coefficients at i to those at all other scatterers $j \neq i$, $j \in \{1, 2, ..., Z\}$,

$$\{\mathbf{B}_i\} = [\boldsymbol{\tau}_i]\left(\{\mathbf{A}_i\} + \sum_{j=1, j\neq i}^{Z} [\boldsymbol{\mathscr{R}}_{ji}]^T \{\mathbf{B}_j\}\right), \tag{5.4}$$

where

$$\boldsymbol{\mathscr{R}}_{ji} = \begin{bmatrix} [\mathbf{R}^p_{ji}] & 0 \\ 0 & [\mathbf{R}^e_{ji}] \end{bmatrix} \tag{5.5}$$

$$[R^p_{ij}]_{nm} = e^{\hat{i}(n-m)\theta_{ij}} H_{n-m}(k_B d_{ij}) \tag{5.6}$$

$$[R^e_{ij}]_{nm} = (-1)^m e^{\hat{i}(n-m)\theta_{ij}} K_{n-m}(k_B d_{ij}), \tag{5.7}$$

and $\{\mathbf{A}_i\} = \begin{Bmatrix} \{\mathbf{A}^p_i\} \\ \{\mathbf{A}^e_i\} \end{Bmatrix}$, $\{\mathbf{B}_i\} = \begin{Bmatrix} \{\mathbf{B}^p_i\} \\ \{\mathbf{B}^e_i\} \end{Bmatrix}$ denote the generalized expansion coefficients in the ith scatterer's local coordinate system. Collecting all Z instances of Eq. (5.4) results in the following relationship for the unknown coefficients of the

scattered waves,

$$\{\mathscr{B}\} = [\mathscr{L}]\{\mathscr{A}\}, \tag{5.8}$$

where

$$\{\mathscr{B}\} = \begin{Bmatrix} \{\mathbf{B}_1\} \\ \{\mathbf{B}_2\} \\ . \\ . \\ . \\ \{\mathbf{B}_Z\} \end{Bmatrix}, \quad \{\mathscr{A}\} = \begin{Bmatrix} [\boldsymbol{\tau}_1]\{\mathbf{A}_1\} \\ [\boldsymbol{\tau}_2]\{\mathbf{A}_2\} \\ . \\ . \\ . \\ [\boldsymbol{\tau}_Z]\{\mathbf{A}_Z\} \end{Bmatrix}, \tag{5.9}$$

and the elements of $[\mathscr{L}]$ hold transformation matrices.

The general format of the T-matrix is

$$[\boldsymbol{\tau}] = \begin{bmatrix} [\mathbf{T}^{pp}] & [\mathbf{T}^{pe}] \\ [\mathbf{T}^{ep}] & [\mathbf{T}^{ee}] \end{bmatrix}. \tag{5.10}$$

where the first superscript specifies the scattered wave type (evanescent or propagating), while the second superscript specifies the incident wave type. Since rigid inclusions are exploited as a means of scattering in this paper, a brief review of their T-matrix development is detailed below. The boundary conditions for the inclusion

at its outer edge, $w_r(a) = \frac{\partial w}{\partial r}(a) = 0$, yield [50]:

$$B_n^p H_n(k_B a) + B_n^e K_n(k_B a) = -A_n^p J_n(k_B a) - A_n^e I_n(k_B a) \tag{5.11}$$

$$B_n^p H_n'(k_B a) + B_n^e K_n'(k_B a) = -A_n^p J_n'(k_B a) - A_n^e I_n'(k_B a). \tag{5.12}$$

Rearranging the above determines the elements of the T-matrix,

$$[T^{pp}]_{nn} = [-J_n(k_B a)K_n'(k_B a) + J_n'(k_B a)K_n(k_B a)]/\Delta_n \tag{5.13}$$

$$[T^{ep}]_{nn} = \frac{2\hat{i}}{\Delta_n \pi k_B a} \tag{5.14}$$

$$[T^{pe}]_{nn} = \frac{1}{\Delta_n k_B a} \tag{5.15}$$

$$[T^{pp}]_{nn} = [I_n(k_B a)H_n'(k_B a) - I_n'(k_B a)H_n(k_B a)]/\Delta_n, \tag{5.16}$$

where

$$\Delta_n = [H_n(k_B a)K_n'(k_B a) - H_n'(k_B a)K_n(k_B a)]/\Delta_n. \tag{5.17}$$

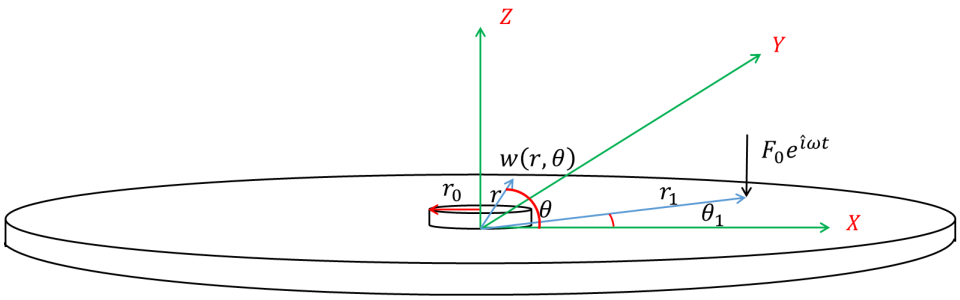

Figure 5.2: ***Equivalent excitation incident wave, source location, and associated geometry for multiple scattering problem.***

5.2.2 Circular piezoelectric patch T-matrix

This section develops a T-matrix for a circular piezoelectric disk, connected to an external circuit, and bonded to the surface of a thin plate. Figure 5.2 depicts the scatterer and the geometry necessary for model development. A circular piezoelectric disk with radius r_0 and thickness h_p is bonded to a substrate of thickness h_s. A global coordinate system (X, Y) is assigned to the center of the piezoelectric disk and polar coordinates (r, θ) locate a point source and plate displacements. Harmonic incident wave excitation, either a point source located at (r_1, θ_1) as shown in Figure 5.2, or a plane wave source, generates the incident wavefield. The general approach taken herein is to break the introduced system into two subdomains: one for the infinite plate, and the other for the piezoelectric disk. Each subdomain is then subject to equal and opposite interaction forces $f(r, \theta)$.

Similar to that done in previous chapters, the substrate response is formed from the superposition of plate displacements due to the incident wavefield w_F, and displacements due to interaction forces w_f. For the piezoelectric disk, w_P captures displacements due to an equal-and-opposite set of interaction forces. Setting equal

the response of both subdomains in the adjoining regions, the unknown distributed interaction forces between the piezoelectric and infinite layer can be identified,

$$w_F(r,\theta,t)\Big|_{r<r_0} + w_f(r,\theta,t,f(r,\theta))\Big|_{r<r_0} = w_P(r,\theta,t,-f(r,\theta))\Big|_{r<r_0}.$$

Since the steady-state behavior of the system is required at the excitation frequency ω, and the model is strictly linear, each displacement field can be written as,

$$w_\Gamma(r,\theta,t) = \phi_\Gamma(r,\theta)e^{\hat{i}\omega t}, \tag{5.18}$$

where subscript Γ can be either F, f, or P. Using the related Green's function, the displacement of the plate due to an harmonic incident wave is given as [50],

$$\phi_F(r,\theta) = \Big(\{\mathbf{A}^p\}^T\{\mathbf{J}(r,\theta)\} + \{\mathbf{A}^e\}^T\{\mathbf{I}(r,\theta)\}\Big). \tag{5.19}$$

The Green's function of an infinite plate under point source excitation [55, 56] can be used to find the response of the plate due to distributed interaction forces $f(r,\theta)$,

$$\phi_f(r,\theta) = \frac{1}{8Dk_B^2\hat{i}}\left(\int_0^{2\pi}\int_0^{r_0} f(r^*,\alpha)\Pi(k_B,\rho_0)\,r^*dr^*\,d\alpha\right), \tag{5.20}$$

where,

$$\Pi(k_B,\rho_0) = [H_0^{(2)}(k_B\rho_0) - H_0^{(2)}(-\hat{i}k_B\rho_0)], \tag{5.21}$$

and $\rho_0 = \sqrt{r^{*2} + r^2 - 2rr^* cos(\theta - \alpha)}$ denotes the distance between the distributed interaction force at (r^*, α) and any location (r, θ), while $H_i^{(2)}$ denotes the Hankel function of the second kind at the ith order.

Considering the displacement fields and the action of the electric circuit, the following relationships can be developed for the unknown interaction forces in the adjoining region,

$$\Big(\{\mathbf{A}^p\}^T\{\mathbf{J}(r,\theta)\} + \{\mathbf{A}^e\}^T\{\mathbf{I}(r,\theta)\}\Big)\Big|_{r<r_0} +$$

$$\frac{1}{8Dk_B^2\hat{i}}\Big(\int_0^{2\pi}\int_0^{r_0} f(r^*,\alpha)\Pi(k_B,\rho_0)\, r^* dr^*\, d\alpha\Big)\Big|_{r<r_0} =$$

$$\sum_{n=0}^{\infty}\sum_{m=0}^{\infty}\Big(\frac{-f_{mn} + \tilde{\theta}_{mn}V_0}{\omega_{mn}^2 - \omega^2 + 2\hat{i}\zeta_{mn}\omega\omega_{mn}}\Big)e^{\hat{i}m\theta}J_m(\lambda_{mn}r)\Big|_{r<r_0}, \tag{5.22}$$

where

$$f_{mn} = \frac{1}{N_n^{(m)}}\int_0^{2\pi}\int_0^{r_0} f(r,\theta)J_m(\lambda_{mn}r)e^{-\hat{i}m\theta}\, r dr\, d\theta \tag{5.23}$$

$$\tilde{\theta}_{mn} = \frac{\hat{\theta}}{N_n^{(m)}}\int_0^{2\pi}\int_0^{r_0} P(r,\theta)J_m(\lambda_{mn}r)e^{-\hat{i}m\theta}\, r dr\, d\theta \tag{5.24}$$

$$N_n^{(m)} = 2\pi\frac{r_0^2}{2}(1 - \frac{m^2}{(\lambda_{mn}r_0)^2})J_m(\lambda_{mn}r_0), \tag{5.25}$$

and $\hat{\theta}$ denotes the electrostatic coupling term arrived at through consideration of the neutral axis of bending, λ_{mn} denotes the eigenvalues for a free edge boundary condition, $\omega_{mn} = \lambda_{mn}^2\sqrt{\frac{D_p}{\rho_p h_p}}$ is the undamped natural frequency related to eigenvalue λ_{mn}, ρ_p and D_p are the denisty and flexural stiffness of the piezoelectric disk, respectively, and ζ_{mn} denote modal damping coefficients. $P(r,\theta)$ is a function that relates the moments of the plate to the voltage of the piezoelectric disk,

$$P(r,\theta) = \Big(\frac{\partial(\delta(r)-\delta(r-r_0))}{\partial r}\Big)\Big(H(\theta)-H(\theta-2\pi)\Big) + r\Big((\delta(r)-\delta(r-r_0)\Big)$$

$$\Big(H(\theta)-H(\theta-2\pi)\Big) + 2r\Big(\delta(r)-\delta(r-r_0)\Big)\Big(\delta(\theta)-\delta(\theta-2\pi)\Big) + 2\Big(H(r)-H(r-r_0)\Big)$$

$$\Big(\delta(\theta)-\delta(\theta-2\pi)\Big) + 2\Big(\frac{\partial(\delta(\theta)-\delta(\theta-2\pi))}{\partial\theta}\Big)\Big(H(r)-H(r-r_0)\Big), \qquad (5.26)$$

where $H(x)$ denotes the Heaviside function and $\delta(x)$ represents the Dirac delta function, respectively.

Similarly, the peak voltage V_0 follows from the integral form of Gauss's equation, which provides an electromechanical coupling equation relating the harvester's displacement to its voltage,

$$V_0 = \hat{i}\omega\frac{\sum_{n=0}^{\infty}\sum_{m=0}^{\infty}\frac{f_{mn}\tilde{\theta}_{mn}}{\omega_{mn}^2-\omega^2+2\hat{i}\zeta_{mn}\omega\omega_{mn}}}{\hat{i}\omega C_p + \frac{1}{R_l} + \sum_{n=0}^{\infty}\sum_{m=0}^{\infty}\frac{\hat{i}\omega\tilde{\theta}_{mn}^2}{\omega_{mn}^2-\omega^2+2\hat{i}\zeta_{mn}\omega\omega_{mn}}}, \qquad (5.27)$$

where C_p denotes the capacitance and R_l the resistance of the electric circuit, respec-

tively.

Similar to that detailed in past chapters, the Bessel function coefficients in Eq. (5.22) are re-arranged and Hankel transformations are performed, resulting in an implicit system of equations containing the desired f_{mn}, which can be stated as

$$\mathscr{F} = [\mathscr{L}]^{-1}[\mathscr{E}]\{\mathbf{A}\}, \tag{5.28}$$

where

$$\mathscr{F} = [f_{00} \;\; f_{01} \;\; f_{02} \ldots f_{10} \;\; f_{11} \ldots f_{MN}]^T, \tag{5.29}$$

and

$$\mathscr{E}_{hj} = \begin{cases} \frac{1}{2\pi N_n^{(m)}} \int_0^{2\pi} \int_0^{r_0} J_h(kr) e^{\hat{i}h\theta} e^{-\hat{i}m\theta} J_m(\lambda_{mn} r) r \, dr \, d\theta, & j < S+1 \\ \frac{1}{2\pi N_n^{(m)}} \int_0^{2\pi} \int_0^{r_0} I_h(kr) e^{\hat{i}h\theta} e^{-\hat{i}m\theta} J_m(\lambda_{mn} r) r \, dr \, d\theta, & otherwise \end{cases}, \tag{5.30}$$

$$\begin{cases} k = [\frac{j-1}{N+1}], \quad l = j - k(N+1) - 1 \\ m = [\frac{h-1}{N+1}], \quad n = h - m(N+1) - 1 \end{cases}. \tag{5.31}$$

In the above equations, $[\frac{a}{b}]$ denotes the floor of a divided by b, M and N denote the series' truncation sizes for piezoelectric modes and S denotes the series' truncation size for propagating waves. Moreover, $\mathscr{L}$ is the coefficient matrix whose elements

follow from Eqs. (5.22)-(5.27),

$$\begin{cases} \mathscr{L}_{hj} = \frac{C_{mn,kl}}{16\hat{i}\pi D k_B^2 N_n^{(m)}} + \frac{\delta_{hj}}{X_{mn}} - \frac{\hat{i}\omega}{X_{mn}} \frac{\frac{\tilde{\theta}_{kl}}{X_{kl}}}{\hat{i}\omega C_p + \frac{1}{R_l} + \sum_{q=0}^{\infty}\sum_{p=0}^{\infty} \frac{\hat{i}\omega\tilde{\theta}_{pq}^2}{X_{pq}}} & h < N+2 \\ \mathscr{L}_{hj} = \frac{C_{mn,kl}}{16\hat{i}\pi D k_B^2 N_n^{(m)}} + \frac{\delta_{hj}}{X_{mn}} & otherwise \end{cases}, \quad (5.32)$$

where

$$C_{mn,kl} = \int_0^{2\pi}\int_0^{2\pi}\int_0^{r_0}\int_0^{r_0} e^{\hat{i}(k\alpha - m\theta)} \Pi(k_B, \rho_0) J_k(\lambda_{kl} r^*) J_m(\lambda_{mn} r) r r^* \, dr^* \, dr \, d\theta \, d\alpha \quad (5.33)$$

$$X_{tz} = \omega_{tz}^2 - \omega^2 + 2\hat{i}\zeta_{tz}\omega\omega_{tz} \quad (5.34)$$

and δ_{hj} represents the Kronecker delta.

In contrast to prior chapter studies in which the patch's modal Bessel functions were used as the final basis functions for the plate-harvester system, here all wave coefficients reference the unbounded Bessel functions. This small, but important, change in perspective facilitates formulation of a stand-alone T-matrix. Following solution for the unknown distribution forces in Eq. (5.28), the net force F_{net} over the total area of the piezoelectric can be calculated as

$$F_{net} = [F]_{1\times 2S}\mathscr{F}, \quad (5.35)$$

where the elements of $[F]$ are given by

$$[F]_{1,j} = \int_0^{2\pi} \int_0^{r_0} J_m(\lambda_{mn} r) e^{\hat{i} m\theta} r \, dr d\theta. \tag{5.36}$$

Assuming the force resultant acts at the middle of the piezoelectric patch, the scattered wave coefficients of the multiple-scattering problem can be arranged as,

$$\{\mathbf{B}\} = \left\{ \begin{array}{c} \{\mathbf{B}^p\} \\ \\ \{\mathbf{B}^e\} \end{array} \right\} = [\mathscr{T}]_{2S\times 1} F_{net}, \tag{5.37}$$

where

$$\mathscr{T}_j = \begin{cases} \frac{\hat{i}}{8k_B^2 D}, & j = 1 \\ \frac{-1}{4\pi k_B^2 D}, & j = S+1 \\ 0, & otherwise \end{cases} . \tag{5.38}$$

Substituting Eqs. (5.35) and (5.37) into Eq. (5.28) results in a linear relationship between the incident and scattered wave (i.e., the T-matrix) for a circular piezoelectric disk,

$$\{\mathbf{B}\} = \overbrace{[\mathscr{T}][F][\mathscr{L}]^{-1}[\mathscr{E}]}^{T\text{-}matrix}\{\mathbf{A}\}. \tag{5.39}$$

In summary, the T-matrix developed yields an input-output relationship governing the scattering of incident waves by a circular piezoelectric disk, where Bessel function expansion coefficients characterize all incident and scattered waves.

5.2.3 Practical implementation and numerical considerations

A practical difficulty encountered when implementing Bessel functions as an expansion basis is their unboundedness at either the origin or infinity, which is exacerbated by increasing order. There are two instances where the Bessel behavior must be addressed: first, in the development of the T-matrix where $k_B a$ is a small term in the boundary condition development, and second in the computation with multiple scattering where evaluation of the functions is done at $k_B d_{ij}$. Therefore choosing the truncation size (refer to Eqs. (5.2-5.3)) must be done with care. The T-matrix considerations are discussed first, followed later by the multiple scattering considerations.

Two of the Bessel functions ($J_m(r,\theta)$ and $I_m(r,\theta)$), at a given r, approach zero as m increases, while the other two ($H_m(r,\theta)$ and $K_m(r,\theta)$) grow exponentially under the same conditions. The truncation order necessary to achieve a given T-matrix accuracy is a function of wavenumber and scatterer diameter. Defining $\gamma = k_B a_{i,min}$ as the product of the wavenumber and the smallest scatterer diameter lumps two of the dependencies together. The necessary considerations for a single scatterer, over a finite domain, can then be formulated for small γ and all m. If only a few orders m are included, inaccuracy may result; on the other hand, including too high an order results in diverging numerical values for the functions $H_m(r,\theta)$ and $K_m(r,\theta)$, yielding a T-matrix with an excessively large condition number.

To overcome these issues, implementation of the functions is done using their truncated series representation (as opposed to using existing function calls in mathematics packages, such as MATLAB) together with normalization. The full series used

to define truncated Bessel functions of integer order n are:

$$J_n(x) = \sum_{k=0}^{\infty} \frac{(-1)^k (\frac{x}{2})^{n+2k}}{k!(k+n)!} \tag{5.40}$$

$$Y_n(x) = \frac{2}{\pi} J_n(x)(ln\frac{x}{2} + 0.577) - \frac{1}{\pi} \sum_{k=0}^{n-1} \frac{(n-k-1)!}{k!} (\frac{x}{2})^{2k-n} + \frac{1}{\pi}$$

$$\sum_{k=0}^{\infty} \frac{(-1)^k \left[\Big(1 + 1/2 + 1/3 + ... + 1/k\Big) + \Big(1 + 2/2 + 1/3 + ... + 1/(k+n)\Big) \right]}{k!(k+n-1)!(\frac{x}{2})^{2k+n}}$$

$$\left(\frac{x}{2}\right)^{2k+n} \tag{5.41}$$

$$I_n(x) = \sum_{k=0}^{\infty} \frac{(\frac{x}{2})^{n+2k}}{k!(k+n)!} \tag{5.42}$$

$$K_n(x) = (\frac{\pi}{2x})^{\frac{1}{2}} e^{-x} \left[1 + \frac{(4n^2 - 1^2)}{1(8x)} \Big(1 + \frac{(4n^2 - 3^2)}{2(8x)} \Big(1 + \frac{(4n^2 - 5^2)}{3(8x)} (1 + ...) \Big) \Big) \right], \tag{5.43}$$

where

$$Y_n(x) = \frac{H_n(x) - J_n(x)}{\hat{i}}. \tag{5.44}$$

For all the defined series, if the argument x is small enough (i.e., $\gamma << 1$) and n is a positive integer, then for $J_n(x)$ and $I_n(x)$, truncation after the first 3 terms is used, while for $Y_n(x)$ and $K_n(x)$ the Maclaurin series is employed with truncation dependent on order n. These considerations lead to the small γ expressions,

$$J_n(x) = 1 - \frac{(\frac{x}{2})^{n+2}}{(n+1)!} + \frac{(\frac{x}{2})^{n+4}}{2!(n+2)!} \tag{5.45}$$

$$Y_n(x) = \begin{cases} \frac{2}{\pi}\Big(ln\frac{x}{2} + 0.577\Big) & n = 0 \\ -\frac{(n-1)!}{\pi}(\frac{2}{x})^n & else \end{cases} \tag{5.46}$$

$$I_n(x) = 1 + \frac{(\frac{x}{2})^{n+2}}{(n+1)!} + \frac{(\frac{x}{2})^{n+4}}{2!(n+2)!} \tag{5.47}$$

$$K_n(x) = \begin{cases} -\Big(ln\frac{x}{2} + 0.577\Big) & n = 0 \\ -\frac{(n-1)!}{2}(\frac{2}{x})^n & else \end{cases}. \tag{5.48}$$

To calculate the negative order of Bessel functions, identities are used as follows:

$$J_{-n}(x) = (-1)^n J_n(x) \tag{5.49}$$

$$Y_{-n}(x) = (-1)^n Y_n(x) \tag{5.50}$$

$$I_{-n}(x) = I_n(x) \tag{5.51}$$

$$K_{-n}(x) = K_n(x). \tag{5.52}$$

Together with their series forms, a normalization is also introduced, in effect defining new expansion coefficients denoted with a $\prime$. This is next illustrated for a rigid scatterer. Normalizing each coefficient, at each order n, using the value of the corresponding Bessel function at $k_B a$ defines the normalized coefficients,

$$B_n^{p\prime} \equiv B_n^p H_n(k_B a), \qquad B_n^{e\prime} \equiv B_n^e K_n(k_B a), \tag{5.53}$$

$$A_n^{p\prime} \equiv A_n^p J_n(k_B a), \qquad A_n^{e\prime} \equiv A_n^e I_n(k_B a). \tag{5.54}$$

These in turn can be substituted into the boundary conditions (e.g., Eqs. (5.11)-(5.12)) and any other relationships,

$$B_n^{p\prime} + B_n^{e\prime} = -A_n^{p\prime} - A_n^{e\prime}, \tag{5.55}$$

$$B_n^{p\prime} \frac{H_n'(k_B a)}{H_n(k_B a)} + B_n^{e\prime} \frac{K_n'(k_B a)}{K_n(k_B a)} = -A_n^{p\prime} \frac{J_n'(k_B a)}{J_n(k_B a)} - A_n^{e\prime} \frac{I_n'(k_B a)}{I_n(k_B a)}, \tag{5.56}$$

which upon re-arrangement yields a normalized T-matrix.

Separate considerations must be employed when using Bessel functions within the multiple scattering approach, where only then $H_n(k_B d_{ij}, \theta)$ and $K_n(k_B d_{ij}, \theta)$ need to be addressed. Accuracy issues arise with the transformation matrices (Eqs. (5.6)-(5.7)). This is important for problems in which the distance between each pair of scatterers d_{ij} varies from a small number to a large one (e.g., a row of fifty scatterers in one direction). In such cases, for a given n, $H_n(k_B d_{ij}, \theta)$ and $K_n(k_B d_{ij}, \theta)$ take on large values when $k_B d_{ij}$ is small, and conversely when $k_B d_{ij}$ is large, these two functions approach zero. No issue arises when $k_B d_{ij}$ is large, and no special truncation is needed. When $k_B d_{ij}$ is small, the expressions in Eqs. (5.46)-(5.48) are again employed.

5.3 Modeling Results

5.3.1 Funnel-shaped MEH structure without a harvester

Results demonstrating the utility of the piezoelectric T-matrix are generated next for an example funnel-shaped MEH structure. Carrara *et al.* [40] experimentally explored a funnel-shaped wave-guide formed from a periodic array of stubs on an aluminum plate. Note that the ability to utilize multiple harvesters in the funnel channel is an advantage the MEH funnel has over MEH structures, such as mirrors and defect resonators, which place a single harvester at the sole focal point. A similar structure on a Lexan host layer with thickness of $3.175mm$ is analyzed herein using rigid inclusions (as opposed to stubs) with diameter $d = 6.35mm$ and lattice spacing $a = 12.7mm$ - see Figure 5.3. Due to the periodic spacing of inclusions and the action of their scattering (termed Bragg scattering), a frequency bandgap emerges at

wavelengths of approximately $2a$ [59]. It is this bandgap that enables the proposed structure, at frequencies in the bandgap, to first geometrically focus the wave in the funnel, and to then guide it into an attached channel where multiple piezoelectric harvesters are located.

Figure 5.4 illustrates the band structure of the Lexan plate with rigid inclusions. The band structure was computed using a single unit cell (see inset of Figure 5.4) analyzed with built-in Floquet periodicity boundary conditions with wavenumbers chosen in a single direction inside the first Brillouin zone (i.e., along the $\Gamma - X$ direction). The nodal displacements were constrained to move only perpendicular to the plate. Solution of the resulting eigenvalue problem yields the band structure shown. As exhibited in the figure, the presence of the rigid inclusions yields a total bandgap between the first and second branches, from approximately $11kHz$ to $43kHz$. This guides the choice for funnel operating frequencies.

A plane wave source located $x_s = 2cm$ away from the entrance of the funnel is used to generate an incident wavefield. Similar to [50], the incident plane wave is modeled for each single scatterer as per Eq. (1), and a Hankel transformation is applied to find the incident wave coefficients,

$$\{A_i^p\}_n = e^{\hat{i}k_B X_i \hat{i}^n} \tag{5.57}$$

$$\{A_i^e\}_n = 0, \tag{5.58}$$

where X_i is the distance between the location of the plane wave source and the i_{th} scatterer. Figure 5.5 depicts the system's wavefield amplitude (absolute displace-

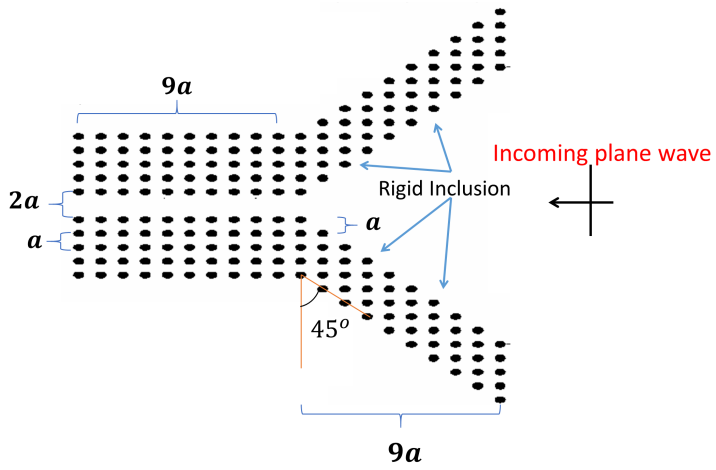

Figure 5.3: ***Schematic of the proposed funnel-shaped structure.***

ment), for multiple excitation frequencies, computed using the multiple scattering solution approach. All displacement values are normalized with respect to the amplitude of the plane wave. For this result, no piezoelectric harvesters are considered in order to assess the pristine wavefield through the structure. As depicted in the subfigures, the proposed structure effectively focuses and channels frequency content starting at approximately $11.5kHz$ and ending at approximately $19kHz$. Note that the funnel effectiveness occurs at frequencies lying in the bandgap, as expected. The strongest focusing and channeling occurs at approximately $17kHz$ for the parameters chosen, where magnification greater than $16\times$ exists in the channel. As expected, and strongly evident in these figures, is the opportunity to harvest at multiple locations along the channel extent. Also evident is transient spatial behavior where the largest wavefield amplitude occurs a few lattice spacings into the channel. Note that due to the propagating nature of the waves, to within a single lattice spacing, the locations of the largest displacement amplitude depends on the time chosen for plotting (or, equivalently, incident wave phase), which is in contrast to MEH mirrors

and resonators. Thus, precise location (to within a lattice spacing) is not critical.

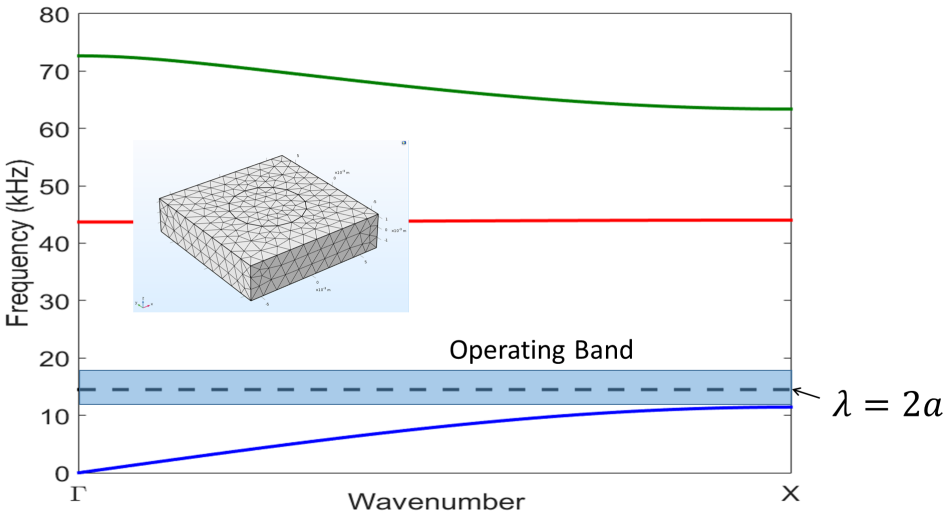

Figure 5.4: ***Band structure of the periodic material along the*** $\Gamma - X$ ***direction.***

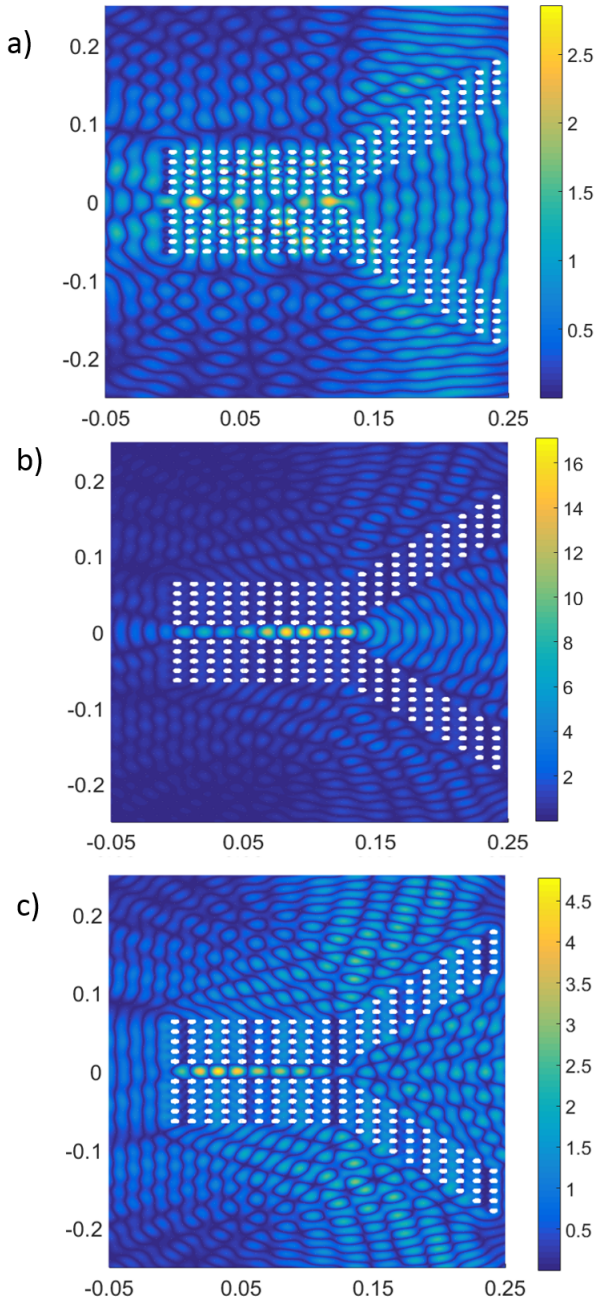

Figure 5.5: ***Computed displacement amplitude of the funnel structure as a function of excitation frequency:*** ***a)*** $\omega = 11.5kHz$, ***b)*** $\omega = 17kHz$, ***c)*** $\omega = 19kHz$.

5.3.2 Funnel-shaped MEH structure with piezoelectric harvesters

The funnel-shaped MEH structure is next assessed for its potential to generate power using piezoelectric harvesters. Considering the system in Figure 5.5b, thin cylindrical piezoelectric harvesters (based on Steiner & Martins, Inc., Model SMD07T03R411 patches) are placed at the focal areas of the structure and the system response is analyzed using the newly-developed T-matrix within the multiple scattering solution approach. Material properties of the SMD07T03R411 harvesters can be found in the previous chapter. The thickness of the piezoelectric disks is $h_p = 0.3mm$, and each radius is $r_0 = 3.5mm$. Figure 5.6 depicts the system's normalized displacement amplitude at $17kHz$ using three piezoelectric harvesters under open circuit conditions (i.e., $\frac{1}{R_L} = 0$ in Eq. (5.27)). As evident in the results, the low-impedance piezoelectric harvesters have little effect on the overall wavefield, and thus MEH design using pristine analyses (i.e., without the complexity of the harvester, as done in Sec. 2.1), is justified. However, prediction of harvested power requires full modeling, as does optimization of the external circuit.

With the piezoelectric patches are connected to an external circuit containing a resistor, harvested power can be predicted. Figure 5.7 presents the average peak power versus load resistance computed for each piezoelectric harvester. The maximum predicted electrical power generated by the first harvester is approximately 11 μW ($P = V_0^2/2R_l$) at $R_l = 30k\Omega$, while for the second and third harvesters this value increases to approximately 17 μW and 20 μW, respectively. This trend, namely that

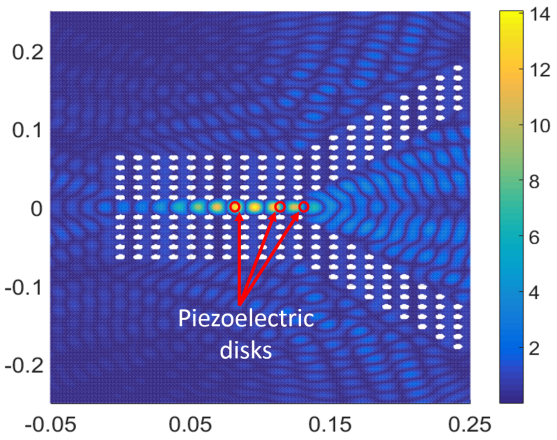

Figure 5.6: ***Computed wavefield displacement generated by plane wave excitation with three piezoelectric harvesters located in the funnel channel.***

the third harvested produces more power than the second, and the second produces more than the first, is supported by the displacement amplitudes previously noted in Figure 5.5. Note also that the peak resistance value roughly conforms to that predicted using a classical weakly-coupled prediction of $1/(\omega C_p) = 40k\Omega$.

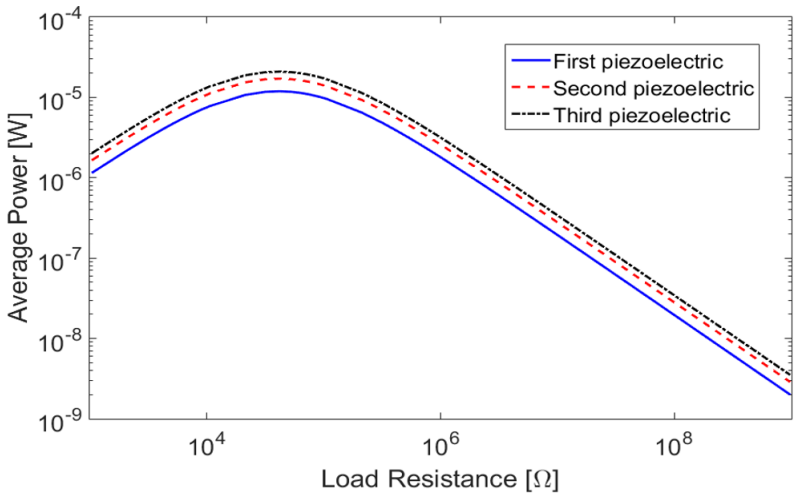

Figure 5.7: ***Computed average power generated by multiple piezoelectric harvesters as a function of load resistance.***

5.3.3 Experimental validation

This section describes a set of experiments aimed at validating the presented T-matrix and multiple scattering approaches. Aluminum (approximately 20× stiffer than the host Lexan material) cylinders with length $6mm$ and diameter $6.35mm$ serve as near-rigid inclusions. As in the computational studies, the Lexan host plate and piezoelectric transducers have thicknesses $h_s = 3.175mm$ and $h_p = 0.3mm$, respectively. The experiments are limited to measuring the surface displacement field (using a scanning laser vibrometer) and recording the harvester voltage. As shown in Figure 5.8, an array of epoxy-bonded piezoelectric transducers (Steiner Martins SMPL7W7T02412, 3M DP270 Epoxy Adhesive) is excited to produce an incident plane wave in response to a generated voltage profile. The excitation transducers are rectangles with dimension $7 \times 7mm$ and effective capacitance $C_p = 1.5nF$. The transducer array is excited by 10 cycles of $f = 17kHz$ voltage using a function generator (Agilent 33220A) coupled to a voltage amplifier (B&K 1040L). A Polytec PSV-400 scanning laser Doppler vibrometer then measures the resulting wavefield using the backside of the plate at a 200×200 grid resolution. Wavefield images and RMS distributions are obtained by recording the out-of-plane plate response covering the piezoelectric harvester and the square subdomain. Proper triggering of the laser measurements allows the reconstruction of the out-of-plane velocity field, while time integration of the recorded responses yields RMS distributions.

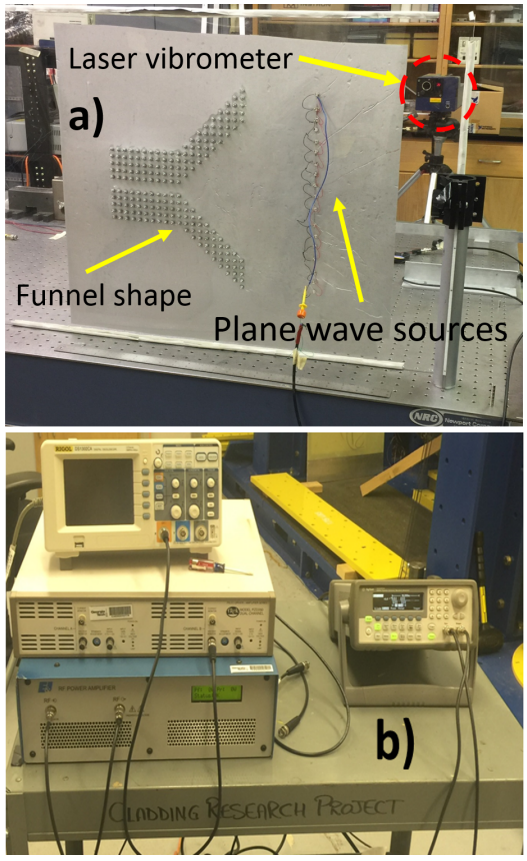

Figure 5.8: ***Experimental setup including a) a Lexan plate hosting piezoelectric transducers for exciting and harvesting waves and laser vibrometer used to measure transverse plate velocities on the plate's backside, which is covered in reflective material, b) function generator and amplifier for generating requisite voltage profiles.***

Figure 5.9 presents the the scattered wavefield obtained experimentally using an attached 1 $M\Omega$ resistor connected to each piezoelectric disk. Clearly evident in this figure is wave energy magnification and channeling at the locations of the piezoelectric disks. Similar to that predicted by the multiple scattering models (Figure 5.6), the funnel clearly focuses wave energy and directs it through to the channel, and overall qualitative behavior measured in the experiment closely matches that predicted using the multiple scattering model. However, the normalized displacement magnitudes in the channel exhibit mismatch (roughly 10.5 versus 16.5, respectively), which results from the non-ideal nature of the experiments compared to the numerical model. Non-ideal entities include the compliance of the aluminum inclusions, which are not truly rigid; imprecise mechanical and electrical material properties for the piezoelectric harvesters and Lexan material; disorder in the lattice structure composing the funnel and channel; and a non-ideal plane wave generated by the finite source.

Figure 5.10 presents a comparison of the analytically-predicted and experimentally-measured peak voltage as a function of load resistance at $17kHz$. For comparison to the computational model, the equivalent value of the point force needed is found by applying the source voltage and waveform to the piezoelectric disk attached to a host plate without a harvester. Then, by measuring the displacement of a point $10cm$ away from the transducer, excitation force F_0 is inferred. A resistance substituter (IET Labs model RS-200) is used to generate a full sweep of resistance from 10 Ω (close to short-circuit condition) to 100 MΩ (close to open-circuit condition). Using an oscilloscope, voltage across the resistor is then measured. As expected based on the previous wavefield results, the piezoelectric harvester closest to the channel entrance

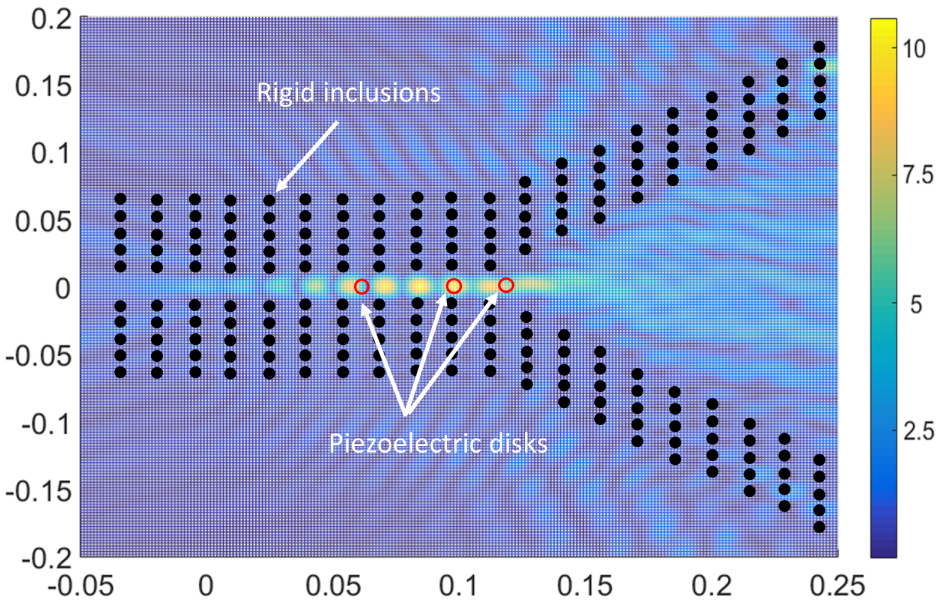

Figure 5.9: ***Experimentally measured scattered wavefield generated by plane wave excitation.***

generates the lowest voltage, while the harvester furthest into the channel produces the highest voltage. Overall, the figure documents good agreement between the predicted and measured peak voltage trends over the entire load resistance considered.

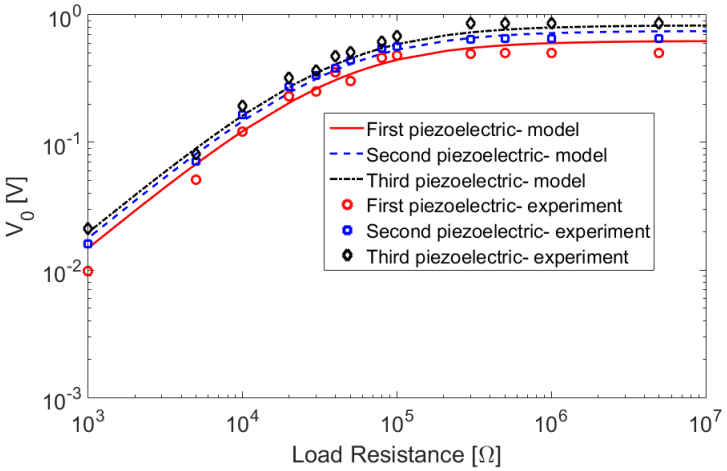

Figure 5.10: ***Experimentally measured peak voltage of the piezoelectric harvesters for varying values of load resistance.***

Chapter 6

Research Contributions and Future Work

This thesis presents a number of contributions to the field of wave energy harvesting. A clearance-type nonlinear energy sink has been introduced for trapping impact energy and extending the period of time over which this energy can be converted to electrical power. The effectiveness of the concept has been demonstrated through analytical, computational, and experimental means. The enhanced power generation, with a minimum amount of increased complexity and cost, may justify further exploration in which complex structures (e.g., plates and/or three-dimensional structures) incorporate one or more of the clearance-type NES's to enhance non-stationary electroacoustic wave energy harvesting.

A closed-form solution for the fully-coupled electromechanical wave response of a circular piezoelectric layer attached to an infinite host substrate has been presented. The proposed analytical approach quantifies the displacement and generated voltage of the system under harmonic point force excitation. The effectiveness of the approach has been validated through comparisons of predicted displacements, voltage, and peak power to those computed using a numerical model and obtained experimentally. The analytical solution provides rapid calculation of response quantities, to include the system's frequency response and optimal circuit resistance, and also provides valuable insight into the relationship between design parameters and system performance. In addition, the presented analysis framework is an important component of a larger

modeling capability aimed at determining optimal metamaterial energy harvester (MEH) approaches in which arrangements of disturbances (i.e., scatterers), attached to or in the host layer, focus and magnify incident wave energy on a piezoelectric harvester.

A multiple scattering approach has been developed for predicting the fully-coupled electromechanical response and energy harvesting capability of a thin plate system incorporating a bonded piezoelectric disk, multiple scatterers (void or rigid inclusions), and a coupled electric circuit. The framework is capable of accurately predicting plate displacements, voltage, and harvested power under harmonic point force excitation. The framework has been evaluated using an MEH concept in which twenty-five scatterers are placed along a semi-elliptical path, a piezoelectric harvester is placed at the nearest focal point, and an harmonic source is placed at the second focal point. The performance of the optimized MEH system is assessed as excitation frequency is varied, demonstrating that the concept effectively harvests wave power over a broad frequency range. Finally, experiments were presented which closely match predicted wavefield displacements and open circuit voltage, and confirm greatly enhanced performance of the optimized system over the non-optimized system.

A fully-coupled T-matrix formulation has been presented for assessing scattering of incident wave energy from a piezoelectric patch attached to a thin plate. Combined with a multiple scattering solution approach, the resulting formulation is capable of accurately predicting plate displacements, voltage, and harvested power resulting from incident plane wave excitation. The formulation has been verified using an experimental MEH concept in which two hundred aluminum inclusions are placed

in a thin Lexan plate, with multiple piezoelectric harvesters placed in the funnel channel. The performance of the MEH system was assessed as excitation frequency is varied, demonstrating that the concept effectively harvests wave power over a range of frequencies roughly satisfying $\lambda \approx 2a$, where λ denotes excitation wavelength and a denotes the lattice constant. Good agreement in predicted and measured response quantities has been documented. Using the newly-developed T-matrix formulation, it is anticipated that future MEH concepts can be explored, evaluated, and optimized with less need for expensive and time-consuming experimental testing.

Bibliography

[1] JA Paradiso and T Starner. Energy scavenging for mobile and wireless electronics. *IEEE Pervasive Computing*, 4(1):18–27, 2005.

[2] Z Chen, B Guo, Y Yang, and C Cheng. Metamaterials-based enhanced energy harvesting: A review. *Physica B: Condensed Matter*, 438:1–8, 2014.

[3] G Litak, MI Friswell, and S Adhikari. Magnetopiezoelastic energy harvesting driven by random excitations. *Applied Physics Letters*, 96(21):214103, 2010.

[4] S Roundy, PK Wright, and JM Rabaey. *Energy scavenging for wireless sensor networks*. Springer, 2003.

[5] P Glynne-Jones, MJ Tudor, SP Beeby, and NM White. An electromagnetic, vibration-powered generator for intelligent sensor systems. *Sensors and Actuators A: Physical*, 110(1):344–349, 2004.

[6] L Wang and FG Yuan. Vibration energy harvesting by magnetostrictive material. *Smart Materials and Structures*, 17(4):045009, 2008.

[7] A Darabi and MJ Leamy. Clearance-type nonlinear energy sinks for enhancing performance in electroacoustic wave energy harvesting. *Journal of Nonlinear Dynamics*, 87(4):2124–2146, 2017.

[8] W Cheng, J Wang, U Jonas, G Fytas, and N Stefanou. Observation and tuning of hypersonic bandgaps in colloidal crystals. *Nature Materials*, 5(10):830, 2006.

[9] B Bonello, C Charles, and F Ganot. Lamb waves in plates covered by a two-dimensional phononic film. *Applied Physics Letters*, 90(2):021909, 2007.

[10] TC Wu, TT Wu, and JC Hsu. Waveguiding and frequency selection of lamb waves in a plate with a periodic stubbed surface. *Physical Review B*, 79(10):104306, 2009.

[11] HX Sun, SY Zhang, and XJ Shui. A tunable acoustic diode made by a metal plate with periodical structure. *Applied Physics Letters*, 100(10):103507, 2012.

[12] AA Maznev, AG Every, and OB Wright. Reciprocity in reflection and transmission: What is a phonon diode? *Wave Motion*, 50(4):776–784, 2013.

[13] M Schmotz, J Maier, E Scheer, and P Leiderer. A thermal diode using phonon rectification. *New Journal of Physics*, 13(11):113027, 2011.

[14] B Liang, XS Guo, J Tu, D Zhang, and JC Cheng. An acoustic rectifier. *Nature materials*, 9(12):989–992, 2010.

[15] B Liang, B Yuan, and JC Cheng. Acoustic diode: Rectification of acoustic energy flux in one-dimensional systems. *Physical Review Letters*, 103(10):104301, 2009.

[16] XF Li, X Ni, L Feng, MH Lu, C He, and YF Chen. Tunable unidirectional sound propagation through a sonic-crystal-based acoustic diode. *Physical Review Letters*, 106(8):084301, 2011.

[17] S Zhu, T Dreyer, M Liebler, R Riedlinger, GM Preminger, and P Zhong. Re-

duction of tissue injury in shock-wave lithotripsy by using an acoustic diode. *Ultrasound in Medicine & Biology*, 30(5):675–682, 2004.

[18] M Sigalas, MS Kushwaha, EN Economou, M Kafesaki, IE Psarobas, and W Steurer. Classical vibrational modes in phononic lattices: Theory and experiment. *Zeitschrift für Kristallographie-Crystalline Materials*, 220(9-10):765–809, 2005.

[19] AF Vakakis. Inducing passive nonlinear energy sinks in vibrating systems. *Journal of Vibration and Acoustics*, 123(3):324–332, 2001.

[20] AF Vakakis. Shock isolation through the use of nonlinear energy sinks. *Journal of Vibration and Control*, 9(1-2):79–93, 2003.

[21] AF Vakakis, LI Manevitch, O Gendelman, and L Bergman. Dynamics of linear discrete systems connected to local, essentially non-linear attachments. *Journal of Sound and Vibration*, 264(3):559–577, 2003.

[22] MA Al-Shudeifat, N Wierschem, DD Quinn, AF Vakakis, LA Bergman, and BF Spencer. Numerical and experimental investigation of a highly effective single-sided vibro-impact non-linear energy sink for shock mitigation. *International Journal of Nonlinear Mechanics*, 52:96–109, 2013.

[23] YS Lee, AF Vakakis, LA Bergman, DM McFarland, and G Kerschen. Enhancing the robustness of aeroelastic instability suppression using multi-degree-of-freedom nonlinear energy sinks. *AIAA Journal*, 46(6):1371–1394, 2008.

[24] OV Gendelman, E Gourdon, and CH Lamarque. Quasiperiodic energy pumping in coupled oscillators under periodic forcing. *Journal of Sound and Vibration*, 294(4):651–662, 2006.

[25] Y Starosvetsky and OV Gendelman. Vibration absorption in systems with a nonlinear energy sink: Nonlinear damping. *Journal of Sound and Vibration*, 324(3):916–939, 2009.

[26] A Luongo and D Zulli. Aeroelastic instability analysis of nes-controlled systems via a mixed multiple scale/harmonic balance method. *Journal of Vibration and Control*, 20(5):1985–1998, 2014.

[27] D Zulli and A Luongo. Control of primary and subharmonic resonances of a duffing oscillator via non-linear energy sink. *International Journal of Non-Linear Mechanics*, 80:170–182, 2016.

[28] H Lin and PJ Antsaklis. Hybrid dynamical systems: An introduction to control and verification. *Found Trends Syst Control*, 1(1):1–172, 2014.

[29] M Di Bernardo, P Kowalczyk, and A Nordmark. Bifurcations of dynamical systems with sliding: Derivation of normal-form mappings. *Physica D: Nonlinear Phenomena*, 170(3):175–205, 2002.

[30] A eJ Luo. *Discontinuous dynamical systems on time-varying domains*. Springer, 2009.

[31] RA DeCarlo, MS Branicky, S Pettersson, and B Lennartson. Perspectives and

results on the stability and stabilizability of hybrid systems. *Proceedings of the IEEE*, 88(7):1069–1082, 2000.

[32] RI Leine and DH Van Campen. Bifurcation phenomena in non-smooth dynamical systems. *European Journal of Mechanics-A/Solids*, 25(4):595–616, 2006.

[33] PJ Holmes. The dynamics of repeated impacts with a sinusoidally vibrating table. *Journal of Sound and Vibration*, 84(2):173–189, 1982.

[34] GW Luo, XH Lv, and YQ Shi. Vibro-impact dynamics of a two-degree-of freedom periodically-forced system with a clearance: Diversity and parameter matching of periodic-impact motions. *International Journal of Non-Linear Mechanics*, 65:173–195, 2014.

[35] G Litak, MI Friswell, and S Adhikari. Magnetopiezoelastic energy harvesting driven by random excitations. *Applied Physics Letters*, 96(21):214103, 2010.

[36] SB Horowitz, M Sheplak, LN Cattafesta III, and T Nishida. A mems acoustic energy harvester. *Journal of Micromechanics and Microengineering*, 16(9):S174, 2006.

[37] LY Wu, LW Chen, and CM Liu. Acoustic energy harvesting using resonant cavity of a sonic crystal. *Applied Physics Letters*, 95(1):013506, 2009.

[38] CJ Rupp, ML Dunn, and K Maute. Switchable phononic wave filtering, guiding, harvesting, and actuating in polarization-patterned piezoelectric solids. *Applied Physics Letters*, 96(11):111902, 2010.

[39] M Carrara, MR Cacan, MJ Leamy, M Ruzzene, and A Erturk. Dramatic enhancement of structure-borne wave energy harvesting using an elliptical acoustic mirror. *Applied Physics Letters*, 100(20):204105, 2012.

[40] M Carrara, MR Cacan, J Toussaint, MJ Leamy, M Ruzzene, and A Erturk. Metamaterial-inspired structures and concepts for elastoacoustic wave energy harvesting. *Smart Materials and Structures*, 22(6):065004, 2013.

[41] M Carrara, JA Kulpe, S Leadenham, MJ Leamy, and A Erturk. Fourier transform-based design of a patterned piezoelectric energy harvester integrated with an elastoacoustic mirror. *Applied Physics Letters*, 106(1):013907, 2015.

[42] S Qi, M Oudich, Y Li, and B Assouar. Acoustic energy harvesting based on a planar acoustic metamaterial. *Applied Physics Letters*, 108(26):263501, 2016.

[43] AN Norris and C Vemula. Scattering of flexural waves on thin plates. *Journal of Sound and Vibration*, 181(1):115–125, 1995.

[44] VV Matus and VF Emets. T-matrix method formulation applied to the study of flexural waves scattering from a through obstacle in a plate. *Journal of Sound and Vibration*, 329(14):2843–2850, 2010.

[45] PC Waterman. Matrix formulation of electromagnetic scattering. *Proceedings of the IEEE*, 53(8):805–812, 1965.

[46] PC Waterman. New formulation of acoustic scattering. *The Journal of the Acoustical Society of America*, 45(6):1417–1429, 1969.

[47] KL Chan, B Smith, and E Wester. Flexural wave scattering in a quarter-infinite thin plate with circular scatterers. *International Journal of Solids and Structures*, 46(20):3669–3676, 2009.

[48] WM Lee and JT Chen. Scattering of flexural wave in a thin plate with multiple circular inclusions by using the null-field integral equation approach. *Journal of Sound and Vibration*, 329(8):1042–1061, 2010.

[49] SZ Peng. Flexural wave scattering and dynamic stress concentration in a heterogeneous plate with multiple cylindrical patches by acoustical wave propagator technique. *Journal of Sound and Vibration*, 286(4):729–743, 2005.

[50] LW Cai and SA Hambric. Multiple scattering of flexural waves on thin plates. *Journal of Vibration and Acoustics*, 138(1):011009, 2016.

[51] SS Rao. *Vibration of continuous systems*. John Wiley & Sons, 2007.

[52] A Darabi, S Shahab, MJ Leamy, and A Erturk. Bimorph disk piezoelectric energy harvester under base excitation: Electroelastic modeling and experimental validation. pages 943110–943110, 2015.

[53] U Aridogan, I Basdogan, and A Erturk. Analytical modeling and experimental validation of a structurally integrated piezoelectric energy harvester on a thin plate. *Smart Materials and Structures*, 23(4):045039, 2014.

[54] A Darabi and MJ Leamy. Analysis and experimental verification of electroacoustic wave energy harvesting in a coupled piezoelectric plate-harvester system. *Journal of Smart Structures and Materials*, 26(3):035047, 2016.

[55] L Cremer, M Heckl, and B Petersson. Structure-borne sound. *Physics Today*, 28:81, 1975.

[56] P Mehta. Vibrations of thin plate with piezoelectric actuator: theory and experiments. *Phd Thesis*, 2009.

[57] K Itao and SH Crandall. Natural modes and natural frequencies of uniform, circular, free-edge plates. *Journal of Applied Mechanics*, 46(2):448–453, 1979.

[58] LW Cai and JH Williams. Large-scale multiple scattering problems. *Ultrasonics*, 37(7):453–462, 1999.

[59] MI Hussein, MJ Leamy, and M Ruzzene. Dynamics of phononic materials and structures: Historical origins, recent progress, and future outlook. *Applied Mechanics Reviews*, 66(4):040802, 2014.